2017

Microcavity Enhanced Beaming and Magneto-Optical Switching of Light

Ali Haddadpour
Louisiana State University and Agricultural and Mechanical College, ahadda5@lsu.edu

Recommended Citation

Haddadpour, Ali, "Microcavity Enhanced Beaming and Magneto-Optical Switching of Light" (2017). *LSU Doctoral Dissertations*. 4434.
https://digitalcommons.lsu.edu/gradschool_dissertations/4434

Microcavity Enhanced Beaming and Magneto-Optical Switching of Light

A Dissertation

Submitted to the Graduate Faculty of the
Louisiana State University and
Agricultural and Mechanical College
in partial fulfillment of the
requirements for the degree of
Doctor of Philosophy

in

The School of Electrical Engineering and Computer Science

by
Ali Haddadpour
B.Sc., University of Tabriz, 2009
M.Sc., University of Tabriz, 2011
May 2017

Dedicated to my parents

تقدیم به

پدر و مادر عزیزم

که درس زندگی و محبت را به من آموخته‌اند.

Acknowledgments

First I would like to acknowledge my advisor Dr. Georgios Veronis for his patience, support and excellent guidance over the years. Without his insightful and innovative ideas, this thesis could not have been accomplished.

It is not easy to appreciate the invaluable support and dedication I received from my parents, Farzaneh and Majid, to whom this dissertation is dedicated. They taught me the value of education and hard work. I can never repay them enough for what they have done for me and I'm truly blessed to have them as my parents. Also I am grateful to my lovely sisters Maryam and Mozhdeh who always do their best for my success.

I would like to thank Professors Jin-Woo Choi, Theda Daniels-Race, Kidong Park, and Jay Park for being members of my general and final examination committees and providing me with their thoughtful comments and suggestions.

Special thanks to my colleagues at Louisiana State University for their friendship and helps, Pouya Dastmalchi, Amirreza Mahigir, and Vahid Foroughi Nezhad. I am also grateful to my friends Kasra Fattah-Hesary, Rod Tohid, Ata Mesgarnejad, and Sahar Marefat Navaz.

I would like to thank my collaborators Dr. Remo Proietti Zaccaria, Dr. Marti Duocastella, Dr. Francesco Tantussi, and Dr. Zongfu Yu.

I would like also to thank the administrative team at the Division of Electrical and Computer Engineering, Louisiana State University. I wish to express my appreciation to Beth R. Cochran for her constant support.

Table of Contents

Chapter

Appendix

Abstract

In this dissertation, we show numerically that a compact structure, consisting of multiple optical microcavities at both the entrance and exit sides of a subwavelength plasmonic slit, can lead to greatly enhanced directional transmission through the slit. The microcavities increase the resonant enhancement of the emission in the normal direction and/or the coupling between free space waves and the slit mode. An optimized structure with two microcavities on both the entrance and exit sides of the slit leads to ∼16 times larger transmission cross section per unit angle in the normal direction compared to the optimized reference slit without microcavities.

We then introduce highly-compact resonant-cavity-enhanced magneto-optical switches for metal-dielectric-metal (MDM) plasmonic waveguides. The static magnetic field induced asymmetry, which enhances or reduces the coupling between the waveguide and a side-coupled resonator, and the relatively large induced wave vector modulation are used to design a Fabry-Perot cavity magneto-optical switch, consisting of a MDM waveguide side-coupled to two MDM stub resonators. The on and off states correspond to either the presence or the absence of the externally applied static magnetic field.

We then investigate the influence of Rabi splitting tuning on the dynamics of strongly coupled J-aggregate/surface plasmon polariton systems. In particular, the Rabi splitting is tuned by modifying the J-aggregate molecule concentration while a polaritonic system is provided by a nanostructure formed by holes array in a golden layer. From the periodic and concentration changes we identify, through numerical and experimental steady-state analyses, the best geometrical configuration for maximizing Rabi splitting, which is then used for transient absorption measurements.

We finally study the combination of scanning probe technology with photonic nanojets. Here, by using advanced 3D fabrication techniques we integrate a microbead on an AFM cantilever thus realizing a system to efficiently position nanojets. This fabrication approach is robust and can be exploited in a myriad of applications, ranging from microscopy to Raman spectroscopy. We demonstrate the potential of portable nanojets by imaging different sub-wavelength structures.

We also show that finite-difference time-domain (FDTD) simulations are in good agreement with experiments.

Chapter 1
Introduction

1.1 Introduction

Nanophotonics is the science and engineering of light-matter interactions at the nanoscale. Dielectric nanophotonic structures and devices, such as photonic crystal devices, enable wavelength-scale manipulation of light. In addition, light-guiding structures which allow subwavelength confinement of the optical mode are important for achieving compact integrated photonic devices [1]. However, the minimum confinement of a guided optical mode in dielectric waveguides is set by the diffraction limit and is of the order of λ_0/n, where λ_0 is the wavelength in free space and n is the refractive index. As opposed to dielectric devices, plasmonic devices have shown the potential to guide subwavelength optical modes, the so-called surface plasmon polaritons, at metal-dielectric interfaces [2].

1.1.1 Light Beaming

The existence of 100 million similar holes on the surface of a gold film was observed in the early 90's by Thomas Ebbesen at the NEC Research Institute at Princeton, New Jersey under an electronic microscope. Standard aperture theory predicts that the transmission efficiency of a single subwavelength cylindrical aperture scales as $(r/\lambda)^4$, where r is the aperture radius, and λ is the wavelength. Since the hole radius in the experiment was 150 nm, based on standard aperture theory less than 0.05 percent of the light incident on the holes could go through them for λ>1000 nm. However, Ebbesen found out that the transmission efficiency exceeded unity (when normalized to the area of the holes) for specific wavelengths. Thus, the metal film behaved as a funnel which steered the incoming light to the holes. At that time he could not find any theoretical explanation for these phenomena and did not publish his strange results [3].

Later in 1998 Peter Wolff joined NEC and became interested in Ebbesen's old experiments. He considered more deeply the behavior of the free electrons in metals and showed that, because electrons can move freely in the surface of metals like a two-dimensional ocean, the incident light can interact with them. Furthermore, if the frequency of the light is the same as the resonant frequency of the electrons, it will cause the phenomena observed by Ebbesen in his experiments. Wolff showed that electrons on a metal surface excited by the incoming light can vibrate and make waves called surface plasmons [3].

Wolff and Ebbesen demonstrated that, when light and surface plasmons have the same energy and momentum, they can convert to each other. The reason for more than 100% transmission of light through the subwavelength apertures in the gold film is that for specific wavelengths the incident light after hitting the surface converts to surface plasmons and directs to the holes, where it can excite new surface plasmons on the other side of the foil and convert to light again [4].

This observation, in addition to making the scientists reconsider their theories, has opened the new field of nanoplasmonics dealing with the interaction of light with nanoscale metallic structures, which could lead to truly novel photonic devices. Surface plasmons have been predicted since around 1900. However, it was only in recent years that fabrication of nanometallic structures made it possible to investigate the interaction of such structures with light.

Different nanostructures have been used around the apertures on the input side such as corrugations, arrays of grooves or gratings to excite the surface plasmons, as well as confine them and lead them through the apertures [Fig. 1.1(a)]. In addition, corrugated metal films on the exit side of the apertures, where regenerated surface plasmons travel, can be used for beaming of light [5]. The excitation of surface plasmons enhances the coupling of incident light into the aperture [6, 7, 8, 9, 10, 11, 12, 13, 14, 15, 16]. Through accurate design of the geometrical parameters of the grooves, the beam direction and width, as well as the wavelength of the beaming light can be tuned. However, the period of such gratings on the entrance and exit sides of the aperture has to be equal to the surface plasmon wavelength, and several grating periods are required. Thus, when operating at optical frequencies, such structures need to be several microns long to lead to enhanced directional transmission through the aperture.

The large number of potential applications for this enhancement of transmission led to a lot of interest for new fabrication methods and technologies with improved accuracy which could enable the realization of the designed nanostructures. A schematic of cylindrical grooves formed around a subwavelength aperture, and a SEM image of the fabricated structure are shown in Figs. 1.1(b) and 1.1(c), respectively. Several design parameters should be considered and accurately controlled during the fabrication process: the film thickness, the depth and width of the grooves as well as the distance between consecutive grooves, the radius of the central hole, and the distance between the central hole and its nearest groove. The concentration and extraordinary transmission of light through small apertures can be used in various applications including photodetectors, optical lenses, and solar cells. A metal-dielectric-metal (MDM) plasmonic focusing cavity was designed to be integrated on an InGaAs/InP avalanche photodiode [17]. The cavity could concentrate light of specific wavelength to enhance its transmission. Through the MDM cavity, light from a large incident area is efficiently coupled to a small output area. The cavity could effectively couple light from an incident area as large as 33.6 μm into two subwavelength holes, with the output light intensity per unit area nine times bigger than that of the input light [17].

One would like to be able to get higher transmission out of these structures and also to control the directivity of transmitted light. Lezec *et al.* overcame this problem by using periodic texture on the input and exit sides of a single aperture [8]. They used a periodic structure in order to couple the free propagating light to surface plasmons on the surface. Thus, a single aperture surrounded by a periodic corrugation in a metal surface was used to enhance the transmission [18]. Free-standing films were used in order to have the capability of pattering the input and exit sides of the films simultaneously as shown in Fig. 1.2(a). The corresponding transmitted light was measured at various angles [Fig. 1.2(b)]. When there were periodic grooves around the hole only in the input side, the output light pattern was fully diffracted. However, when grating of the same period was patterned around the exit side of the hole, beaming was observed and the angular dependence was clear. The light is more directive at specific angles. A plot of the transmission intensity as a function of angle is illustrated in Fig. 1.2(d). An optical image of the exit surface of a bull's eye structure at its peak transmission wavelength is shown in Fig. 1.2(c).

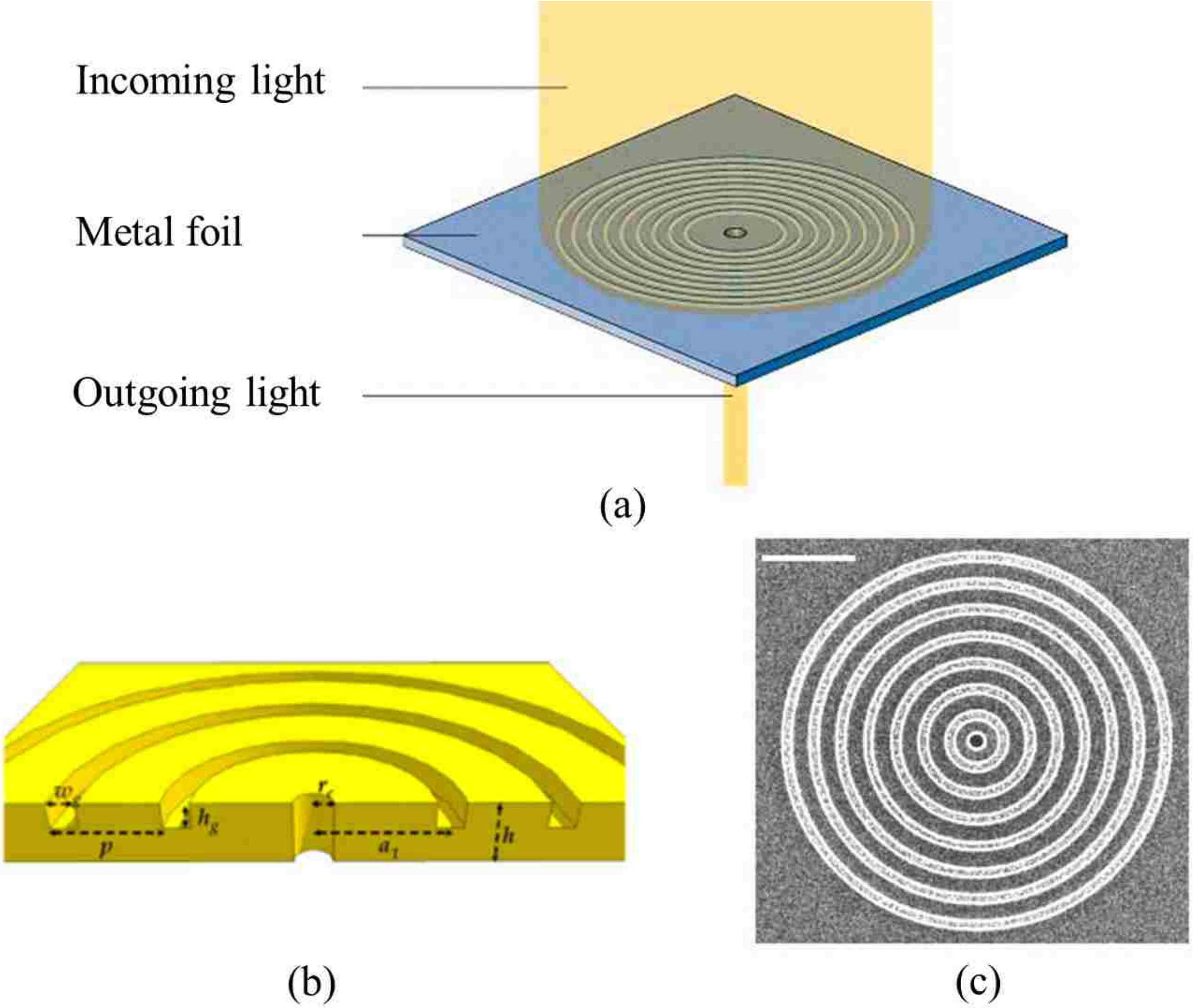

Figure 1.1: (a) Enhancement of the optical transmission through a subwavelength aperture by cylindrical grooves formed around the aperture. (b) Schematic of groove arrays around a subwavelength aperture. (c) SEM image of the fabricated structure designed to enhance optical transmission at a wavelength of 660 nm. The scale bar corresponds to 2 μm [4].

It was previously demonstrated that the use of a single microcavity at the entrance and exit sides of a subwavelength plasmonic slit, can enhance the transmission cross section of the slit

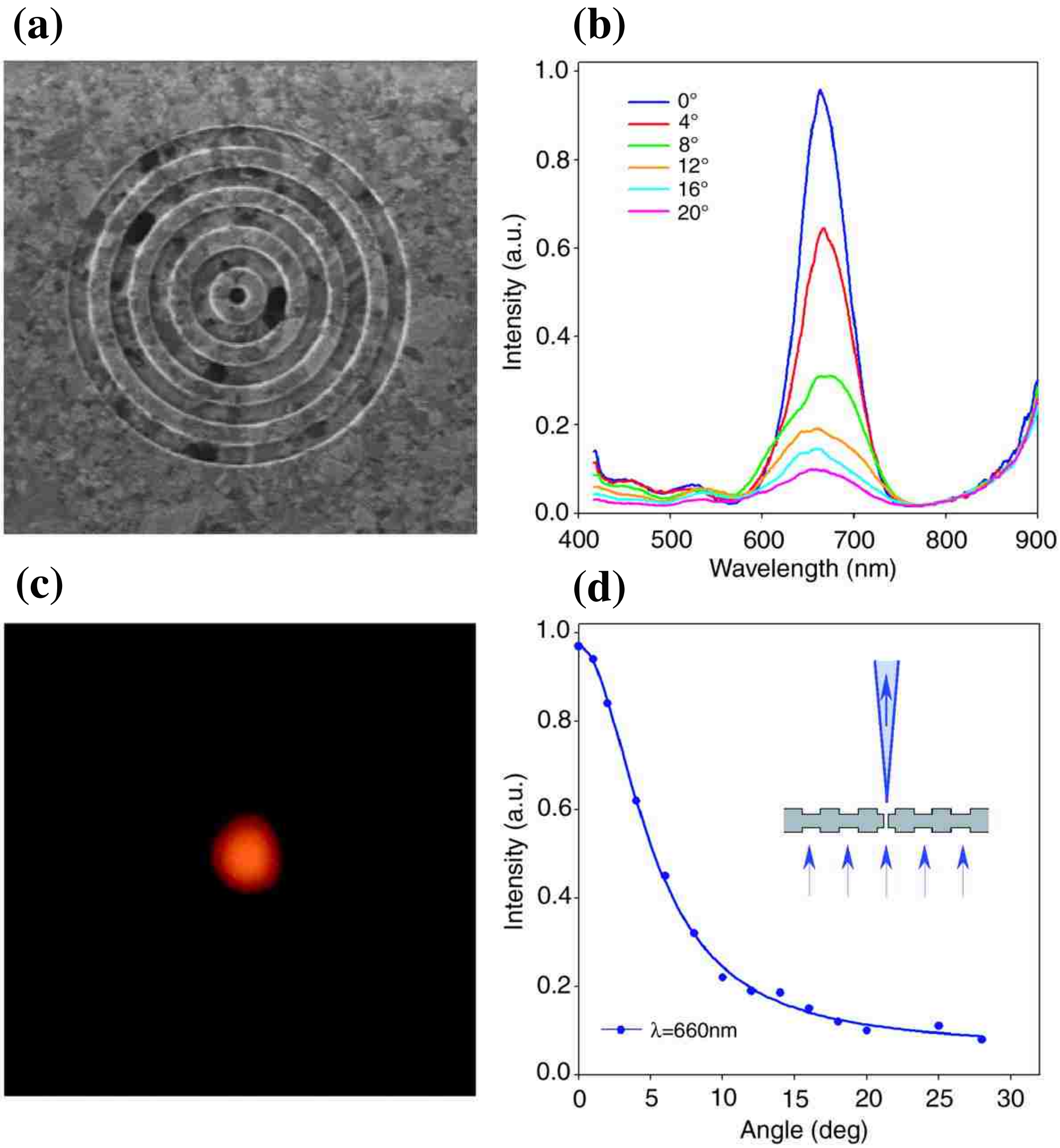

Figure 1.2: (a) FIB micrograph image of a bull's eye structure surrounding a cylindrical hole in a suspended Ag film (groove periodicity, 500 nm; groove depth, 60 nm; hole diameter, 250 nm; film thickness, 300 nm). (b) Transmission spectra recorded at various collection angles for a bull's eye structure on both sides of a suspended Ag film (groove periodicity, 600 nm; groove depth, 60 nm; hole diameter, 300nm; film thickness, 300 nm). The tail above 800 nm is an artifact of the spectral measurement. The structure is illuminated at normal incidence with unpolarized collimated light. The spectra were measured using a Nikon TE200 microscope coupled to an Acton monochromator and a Princeton Instruments CCD (charge-coupled device) camera. (c) Optical image of the sample of (a) illuminated from the back at its wavelength of peak transmission ($\lambda_{\max} = 660$ nm) using a 50-nm band-pass filter. (d) Angular transmission-intensity distribution derived from the spectra of (b) at $\lambda_{\max}$. (Inset) Schematic diagram of the structure and the beam divergence and directionality of the transmitted light at $\lambda_{\max}$ in the far field [8].

[19, 20]. Min and Gordon used highly reflective gold as a simple mirror to enhance the optical transmission through a subwavelength slit [20]. They showed numerically, using the finite-difference time-domain (FDTD) method, and experimentally that the optical transmission through the slit was resonantly enhanced by a factor of 2, by forming a surface plasmon microcavity around the slit. By varying the geometrical parameters of the microcavity such as its width, the wavelength of maximum transmission was tuned [20]. In addition, it was shown that a microcavity can greatly enhance the coupling efficiency between a MDM waveguide of wavelength-sized width and a MDM waveguide of subwavelength width [21].

It was also shown that the use of multiple microcavities at the entrance and exit sides of a subwavelength slit filled with an absorbing material can greatly enhance the absorption cross section of the slit [22]. Min *et al.* showed that the microcavity greatly enhances the incident light coupling into the slit by means of improving the impedance matching between the input plane wave and the slit mode [22]. They also used microcavities at the exit side of the slit, and found that these microcavities result in larger reflectivity and therefore larger resonant field enhancement. It was found that by optimizing two microcavities at each of the input and exit sides of the slit results in $\sim$9.3 times absorption enhancement at the optical communication wavelength compared to an optimized slit without microcavities [22].

1.1.2 Active Magneto-plasmonics

Achieving active control of the flow of light in plasmonic devices is of fundamental interest in plasmonics for designing modulators, couplers, add-drop filters, switches, and active multiplexers. Numerous passive plasmonic devices such as waveguides with different shapes and lengths have been designed. However, transporting information is not enough, we also need to be able to process it. For this reason, one of the targets for plasmonic circuits is to develop active components such as modulators and switches [23, 24, 25]. A possible route to actively control plasmons is to use an externally applied magnetic field [26, 27]. As an example, external magnetic fields could be used to control plasmonic devices through analogies of the Kerr and Faraday effects [28, 29]. Compared to electro-optics or thermo-optics, magneto-optics could lead to faster modulation speeds [27]. While in electro-optics the permittivity of dielectric materials is modified, in magneto-optics an externally applied magnetic field is able to modulate surface plasmons by changing the permittivity of conductors.

In the interaction of incident electromagnetic waves with the free electrons of a conductor, the free electrons respond collectively by oscillating resonantly with the incident waves. The resonant oscillation is characterized by a characteristic frequency, the bulk plasmon frequency ω_P, which sets the scale of the free electrons' response to time-varying perturbations [30]. The Lorentz force on the free electrons of a conductor as a result of the applied external magnetic field will influence the properties of surface plasmons. In the case of an applied external magnetic field, another characteristic frequency called cyclotron frequency and defined as $\omega_B = \frac{eB}{m}$ is important. Here, e is the electron charge, and m is the electron mass. The cyclotron frequency is proportional to the strength of the applied magnetic field $\mathbf{B}$ [31]. In the presence of a static magnetic field $\mathbf{B}$ in the z direction, the dielectric permittivity of the metal is described by a tensor [32, 33]:

$$\bar{\bar{\varepsilon}} = 1 - \frac{\omega_P^2}{(\omega + i/\tau)^2 - \omega_B^2} \times \begin{pmatrix} 1 + i\frac{1}{\tau\omega} & i\frac{\omega_B}{\omega} & 0 \\ -i\frac{\omega_B}{\omega} & 1 + i\frac{1}{\tau\omega} & 0 \\ 0 & 0 & \frac{(\omega+i/\tau)^2-\omega_B^2}{\omega(\omega+i/\tau)} \end{pmatrix}, \tag{1.1}$$

where the decay time τ characterizes the material loss in the metal.

There are numerous devices based on surface magneto-plasmons. As an example, a tunable planar plasmonic slit lens was proposed in 2012 [34]. The tunable planar plasmonic slit lens consists of metallic slab with several appropriately designed nano-slits as shown in Fig. 1.3(a). The focusing of light with this lens can be tuned by adjusting the geometric parameters and the materials of the slits. By replacing the metal with a semiconductor, a tunable THz lens was designed. With the intensity of the external magnetic field increased to 1 T, the focal length was tuned by 3λ, as shown in Fig. 1.3.

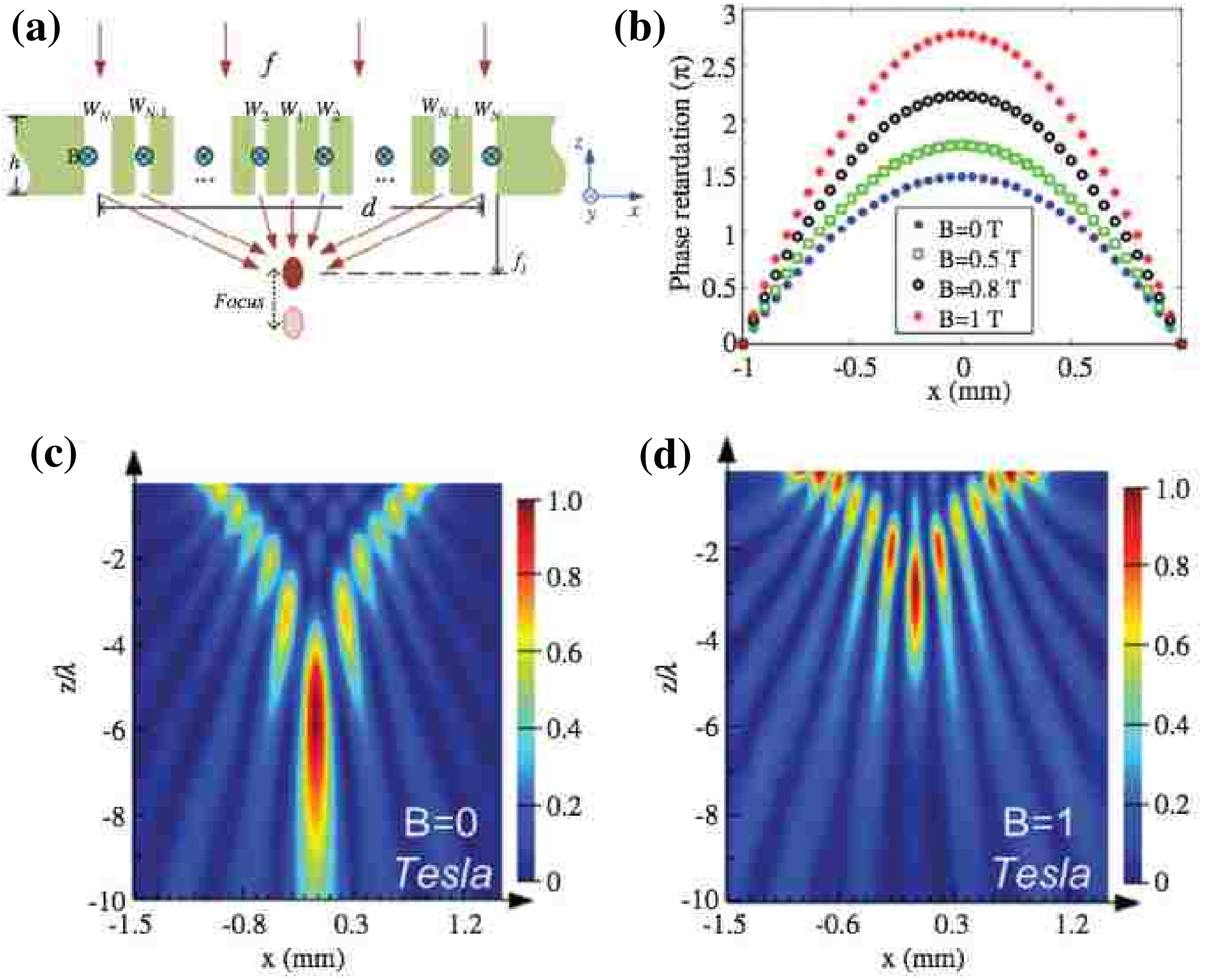

Figure 1.3: A tunable plasmonic lens (from [34]). (a) Schematic structure of the lens. The structure consists of an InSb slab tunable by an external magnetic field **B**, and perforated with 2N-1 subwavelength slits. (b) The relative phase retardation of the slits under magnetic fields of 0, 0.5, 0.8 and 1 T. (c), (d) Field distributions of the structure when the external magnetic field is 0 T and 1 T, respectively.

By using various magneto-optical materials, non-reciprocal propagation effects have been realized which can be used in integrated optoelectronic applications [35]. Mathew *et al.* studied numerically the propagation properties of the surface plasmon polariton modes in metal-strip plasmonic waveguides with magneto-optic substrate material [36]. Different subwavelength waveguide components based on gyrotropic materials have been studied, enabling subwavelength guiding and tunable non-reciprocal plasmon propagation [37, 33, 38]. The enhancement of magneto-optical

Kerr effects in multilayers of noble and ferromagnetic metals has been reported in the literature [39, 40, 41]. Sepulveda *et al.* investigated the magneto-optical effects in surface plasmon polariton modes guided by metallic layers as a function of the metallic thickness for different orientations of the magnetization [37]. It was shown that strong magneto-optical effects can be realized for long-range surface plasmon modes [37]. In addition, a new type of high-speed modulators based on magneto-optical effects has been investigated [42, 43], in which the dimensions of the device have been reduced by employing the capabilities of surface plasmon polariton propagation [43]. Khatir and Granpayeh proposed a wide-band high-speed magneto-optical switch. The operation of the proposed structure is based on the variations of the magnetic bias condition by altering the magnetization within an yttrium iron garnet (YIG) layer [44]. Bonanni *et al.* proposed the use of nickel nanodisks as a good candidate for biosensing devices [45]. They showed that nickel nanoferromagnets act as a magneto-plasmonic material, by demonstrating strong and tunable correlation between the localized plasmons and magneto-optics. Their findings point out the capability to actively control plasmons for magneto-optical light modulation [45].

In systems with broken time-reversal symmetry, the effect of disorders can be suppressed with the use of a one-way waveguide [33]. In this kind of waveguides, there is a one-way frequency range where only a forward propagating mode is allowed. So as a result there is no radiation or backward modes. Yu *et al.* proposed a one-way waveguide formed at the interface between a photonic crystal and a free-electron metal subject to an external magnetic field [33]. They showed that, as long as the surface plasmon frequency of the metal surface lies within the bandgap of the photonic crystal, the waveguide acts as a one-way waveguide [33].

Montoya *et al.* designed a surface plasmon isolator using the non-reciprocal coupling between a dielectric waveguide mode and a surface plasmon polariton mode at the interface between a ferromagnetic metal (Fe) and air [46], as shown in Fig. 1.4. The confinement in the metal results in an enhanced non-reciprocal response. An applied external magnetic field produces a non-reciprocal effective index in the magneto-optical surface plasmon waveguide. When the external magnetic field **B** is applied, weak coupling occurs between the dielectric waveguide and the surface plasmon waveguide in the forward direction, while for the backward-propagating mode coupling into the lossy surface plasmon mode results in large isolation, since the backward-propagating mode is absorbed in the ferromagnetic metal.

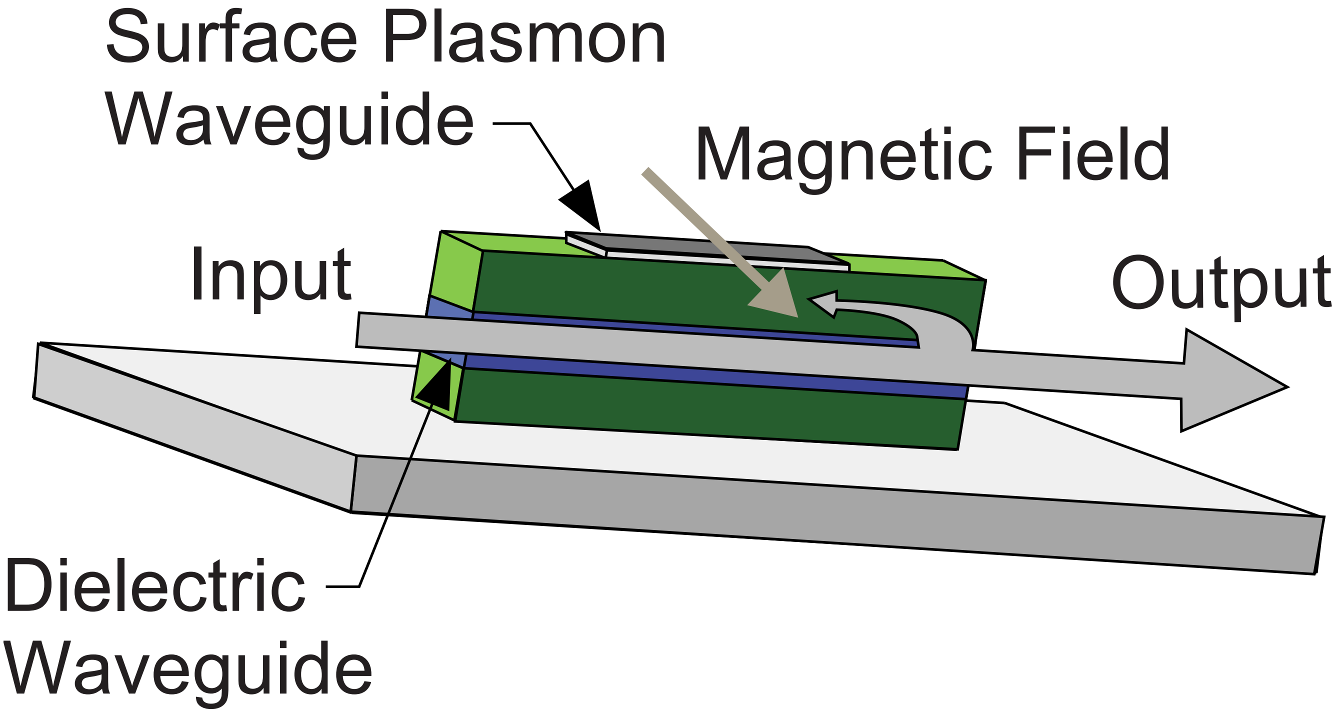

Figure 1.4: Non-reciprocal coupling concept for a surface plasmon optical isolator. In the forward direction, weak coupling occurs resulting in low insertion loss. In the reverse direction, the surface plasmon mode and the dielectric waveguide mode are index matched and strong coupling occurs resulting in large isolation [46].

Temnov *et al.* used a ferromagnetic layer (cobalt) in order to benefit from its stronger magneto-optical response compared to conventional metals [26]. They fabricated a plasmonic micro-interferometer consisting of a hybrid gold-cobalt-gold structure on a glass substrate, as shown in Fig. 1.5. Cobalt by itself has higher ohmic loss so that it is not a good material option for supporting surface plasmon polaritons over a long distance. However, if cobalt is integrated in a hybrid gold-cobalt-gold geometry, the resulting structure could combine the low-loss surface plasmon propagation on a gold surface with the large magneto-optical effect provided by a ferromagnetic layer. As shown in Fig. 1.5, an oscillating external magnetic field **B** was applied to periodically switch the magnetization of the cobalt layer and modulate the surface plasmon wave vector [26]. Temnov *et al.* were able to observe the wavevector modulation by means of a very small external magnetic field.

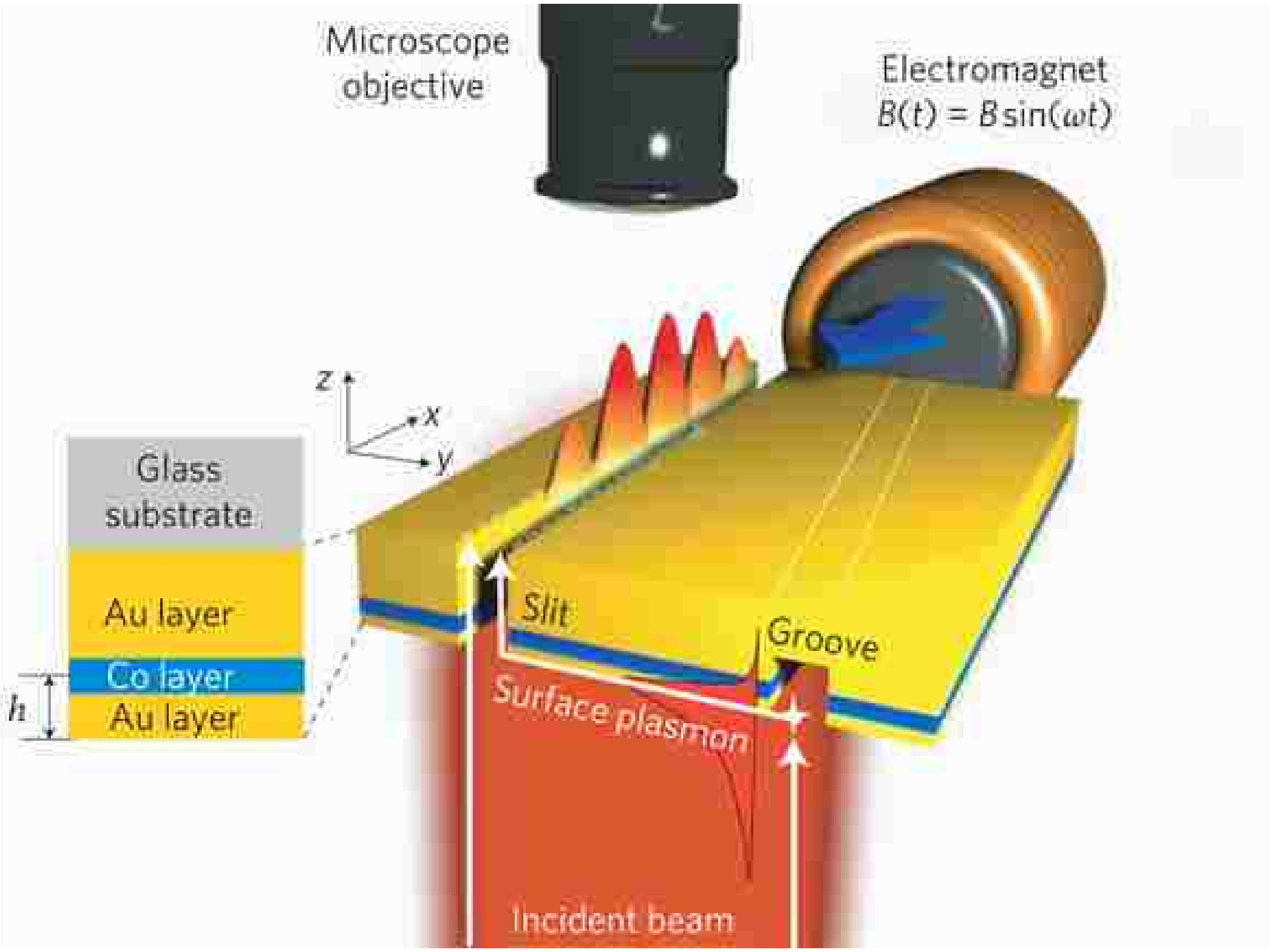

Figure 1.5: Active magneto-plasmonic interferometry. A plasmonic micro-interferometer consisting of a tilted slit-groove pair is milled in a gold-cobalt-gold multilayer film using a focused ion beam. Surface plasmons are launched by the groove, propagate towards the slit, and interfere with the directly transmitted light to produce a periodic interference pattern along the slit axes. The oscillating magnetic field of an electromagnet is used to periodically switch the magnetization in the thin cobalt layer and thus modify the wavevector of surface plasmons. An imaging nano-optical set-up is used to record the magneto-plasmonic modulation signal [26].

1.2 Outline of the Dissertation

The remainder of this dissertation is organized as follows. In Chapter 2, we investigate micro-cavity enhanced directional transmission through a subwavelength plasmonic slit. In Chapter 3, we introduce highly-compact resonant-cavity enhanced magneto-optical switches for MDM plasmonic waveguides. As part of this dissertation research, we also collaborated with a research group at the Istituto Italiano di Tecnologia (IIT) in Genoa, Italy. We performed all required numerical simulations and theoretical analyses to support the experimental results of our collaborators at IIT. This work is described in Chapters 4 and 5. More specifically, in Chapter 4, we investigate the influence of Rabi splitting tuning on the dynamics of strongly coupled J-aggregate/surface plasmon polariton systems. In Chapter 5, we study the combination of scanning probe technology with photonic nanojets. Finally, in Chapter 6 we summarize our conclusions and give some recommendations for future work.

Chapter 2
Microcavity enhanced directional transmission through a subwavelength plasmonic slit

2.1 Introduction

Resonant nanoscale metallic apertures can efficiently concentrate light into deep subwavelength regions, and therefore greatly enhance the optical transmission through the apertures [6] or the absorption in or below the apertures [7, 47, 19]. In addition, grating structures, consisting of periodic arrays of grooves patterned on the metal film surrounding the entrance of the aperture, can excite surface plasmons on the metal surface. The excitation of surface plasmons enhances the coupling of incident light into the aperture [6, 7, 8, 9, 10, 11, 12, 13, 14, 15, 16, 48, 49]. When a grating structure is also formed on the exit side of the aperture, the transmission of light through the aperture can be highly directional [8, 9, 48, 49, 50, 51, 52, 53]. Such beaming of light from metallic nanoapertures can lead to numerous applications which include enhancing the performance of near-field devices for microscopy and data storage, and reducing the beam divergence of light sources such as lasers [8, 54]. However, the period of such gratings on the entrance and exit sides of the aperture has to be equal to the surface plasmon wavelength, and several grating periods are required. Thus, when operating at optical frequencies, such structures need to be several microns long to lead to enhanced directional transmission through the aperture.

It was previously demonstrated that the use of a single microcavity at the entrance and exit sides of a subwavelength plasmonic slit, can enhance the transmission cross section of the slit [19, 20]. In addition, it was shown that a microcavity can greatly enhance the coupling efficiency between a MDM waveguide of wavelength-sized width and a MDM waveguide of subwavelength width [21]. It was also demonstrated that the use of multiple microcavities at the entrance and exit sides of a subwavelength slit filled with an absorbing material can greatly enhance the absorption cross section of the slit [22].

Here, we show numerically that a compact structure, consisting of multiple optical microcavities at both the entrance and exit sides of a subwavelength plasmonic slit, can lead to greatly enhanced directional transmission through the slit [55]. Our reference structure is an optimized subwavelength slit without microcavities. We show that the presence of the microcavities at the entrance and exit sides of the slit can lead to significantly larger reflectivity at both sides of the slit, and therefore to larger resonant transmission enhancement. In addition, the microcavities at the entrance and exit sides of the slit can greatly improve the impedance matching, and therefore the coupling between free-space waves and the slit mode. Such structures enhance both the incoupling of normally incident light from free space into the slit mode, as well as the outcoupling of light from the slit mode to free-space radiation in the normal direction. An optimized structure with two microcavities on both the entrance and exit sides of the slit leads to $\sim$16 times larger transmission cross section per unit angle in the normal direction compared to the optimized reference slit without microcavities. We also show numerically that, while all structures were optimized at a single wavelength, the operation frequency range for high emission in the normal direction is broad.

The remainder of this chapter is organized as follows. In Section 2.2, we define the transmission cross section and the transmission cross section per unit angle of the slit, and employ single-mode scattering matrix theory to account for their behavior. The results obtained for the reference slit without microcavities, as well as for the microcavity enhanced structures are presented in Section 2.3.

2.2 Transmission cross section and transmission cross section per unit angle

We consider a structure consisting of a single slit in a silver film with N microcavities at the entrance side, and M microcavities at the exit side of the slit (Fig. 2.1). We use silver for the metal film due to its relatively low material loss at near-infrared wavelengths. Other metals such as gold can also be used. The structures are compact with all microcavity dimensions limited to less than 1.6 μm.

We use a two-dimensional finite-difference frequency-domain (FDFD) method [56] to calculate the transmission through the structures as well as their radiation pattern. This method allows us to directly use experimental data for the frequency-dependent dielectric constant of metals such as silver [57], including both the real and imaginary parts, with no approximation. We use perfectly matched layer (PML) absorbing boundary conditions at all boundaries of the simulation domain [58]. We also use the total-field-scattered-field formulation to simulate the response of the structure to incident plane waves from free space with the electric field in plane [59].

We consider *symmetric* structures having the same number of microcavities on the entrance and exit sides of the slit ($N = M$), and the same microcavity dimensions ($w_{\mathrm{T}i} = w_{\mathrm{B}i}, d_{\mathrm{T}i} = d_{\mathrm{B}i}, i = 1, ..., N$). This is due to the fact that the optimized structures which lead to maximum emission in the normal direction for a normally incident plane wave were found to be symmetric. In other words, a multiple microcavities structure, which is optimum for incoupling normally incident light from free space into the slit mode, is also optimum for outcoupling light from the slit mode to free-space radiation in the normal direction.

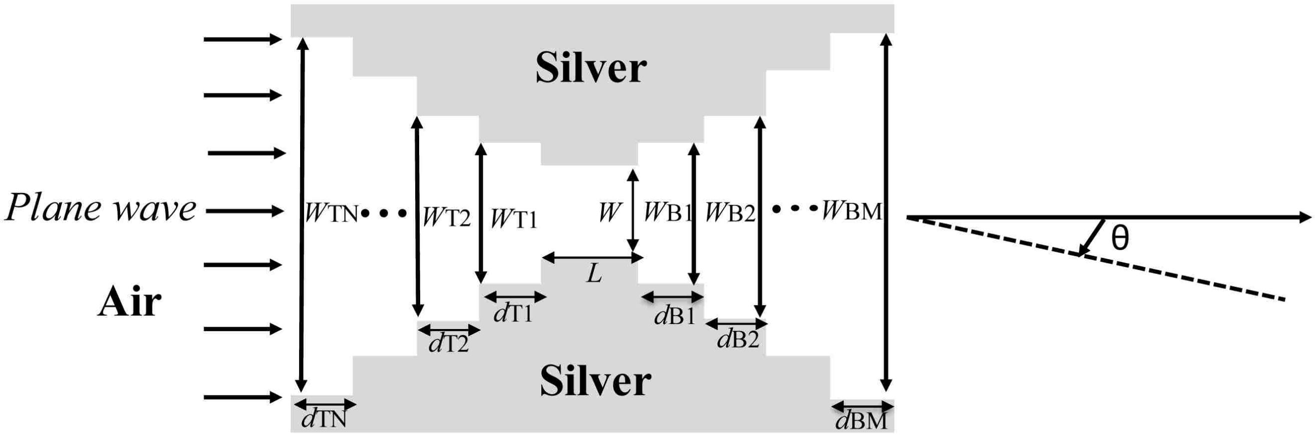

Figure 2.1: Schematic of a structure consisting of a slit in a silver film with N microcavities at the entrance side, and M microcavities at the exit side of the slit.

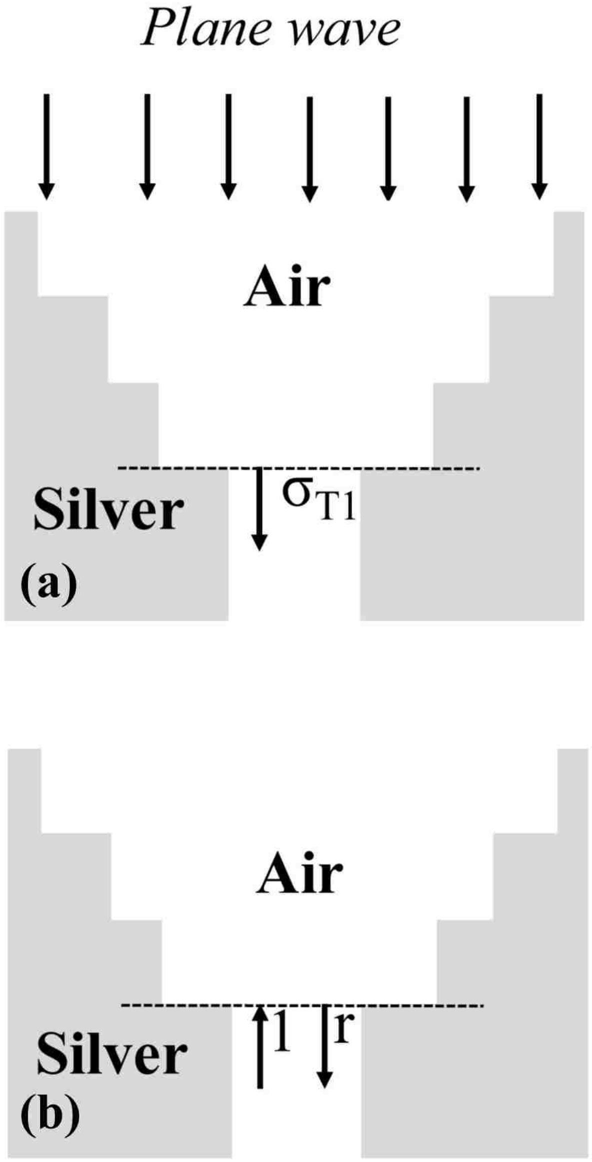

Figure 2.2: (a) Schematic defining the transmission cross section σ_{T1} of a silver-air-silver waveguide through the structure above the entrance side of the slit of Fig. 2.1 for a normally incident plane wave from air. (b) Schematic defining the reflection r of the fundamental TM mode of a silver-air-silver waveguide at the interface of such a waveguide with the structures at the entrance and exit sides of the slit of Fig. 2.1.

For comparison of different configurations, we define the *transmission cross section* σ_{T} of the slit as the total power radiated from the slit (per unit length in two dimensions) normalized by the incident plane wave power flux. In two dimensions, the transmission cross section has units of length (m). We also define the *transmission cross section per unit angle* σ of the slit as the power radiated from the slit per unit angle normalized by the incident plane wave power flux. In two dimensions, the transmission cross section per unit angle has units of length per angle (m/rad).

We develop a single-mode scattering matrix theory to account for the behavior of these systems [60]. We define the transmission cross section σ_{T1} of a silver-air-silver MDM waveguide of width w (in the unit of length in two dimensions) as the transmitted power into the waveguide from the structure above the entrance side of the slit of Fig. 2.1, normalized by the incident plane wave power flux [Fig. 2.2(a)]. We also define r as the complex magnetic field reflection coefficient for the fundamental propagating TM mode in a silver-air-silver MDM waveguide of width w at the interface of such a waveguide with the structures at the entrance and exit sides of the slit of Fig. 2.1 [Fig. 2.2(b)]. Finally, we define the directivity D as the ratio of the radiation intensity in a given direction from the slit to the radiation intensity averaged over all directions [61]. We use FDFD to numerically extract σ_{T1} and r [22, 60, 62]. We also use FDFD to numerically calculate the directivity $D(\theta)$ at an angle θ with respect to the normal as

$$D\left(\theta\right) = \frac{S_{\mathrm{PW}}\left(\theta\right)\pi r_{\mathrm{FF}}}{P_{\mathrm{out}}}, \tag{2.1}$$

where $S_{\mathrm{PW}}\left(\theta\right) = \frac{1}{2}\eta_0 |H_{\mathrm{FF}}\left(\theta\right)|^2$ is the far-field power density at a distance r_{FF} above the slit, and at an angle θ with respect to the normal, and P_{out} is the total power emitted through the slit (per unit length in two dimensions). Here η_0 is the free-space impedance, and H_{FF} is the magnetic field in the far-field. We choose r_{FF} to be sufficiently far, so that the numerically calculated directivity becomes independent of r_{FF} [19]. The transmission cross section per unit angle of the slit at an angle θ with respect to the normal can then be calculated using scattering matrix theory as [22, 60, 62]:

$$\sigma\left(\theta\right) = \sigma_{\mathrm{T}}\frac{D\left(\theta\right)}{\pi} = \sigma_{\mathrm{T1}}\eta_{\mathrm{res}}T\frac{D\left(\theta\right)}{\pi}, \tag{2.2}$$

where $T = 1 - |r|^2$ is the power transmission coefficient of the slit, $\eta_{\mathrm{res}} = \left|\frac{\exp(-\gamma L)}{1-r^2\exp(-2\gamma L)}\right|^2$ is the resonance enhancement factor associated with the slit resonance, γ is the complex wave vector of the fundamental propagating TM mode in a silver-air-silver MDM waveguide of width w, and L

is the length of the slit. Based on Eq. 2.1, we observe that, for fixed slit dimensions, w and L are fixed, so that the transmission cross section per unit angle of the slit σ is solely determined by σ_{T1}, r, and D. These three parameters in turn can be tuned by adjusting the geometrical dimensions of the microcavities at the entrance and exit sides of the slit.

2.3 Results

We first consider our reference structure consisting of a single subwavelength slit in a metal film (Fig. 2.3). In Fig. 2.4 we show the transmission cross section per unit angle in the normal direction $\sigma\,(\theta = 0^o)$ for such a structure as a function of the slit length L calculated using FDFD. The transmission cross section per unit angle is normalized with respect to w/π. A normalized transmission cross section per unit angle of one $[\sigma/(w/\pi) = 1]$ therefore corresponds to a structure with transmission cross section equal to the geometric cross section of the slit ($\sigma_{\mathrm{T}} = w$), which radiates isotropically in all directions [$D(\theta)$=1 for all θ]. We found that, as the slit length L increases, the transmission cross section per unit angle in the normal direction exhibits peaks, corresponding to the Fabry-Perot resonances in the slit. In Fig. 2.4 we also show the transmission cross section per unit angle in the normal direction calculated using scattering matrix theory (Eq. 2.2). We observe that there is excellent agreement between the scattering matrix theory and the exact results obtained using FDFD. Similarly, excellent agreement between the results of these two methods is observed for all the structures considered in this chapter (Table 2.1). The maximum normalized transmission cross section per unit angle for the slit is ∼7.25 (Fig. 2.4). For such a structure the transmission cross section σ_{T1} of the corresponding silver-air-silver MDM waveguide with width $w = 50$ nm is ∼184 nm (Table 2.1), which is significantly larger than w. This is due to the fact that subwavelength MDM plasmonic waveguides collect light from an area significantly larger than their geometric cross-sectional area [63]. In addition, the resonance enhancement factor associated with the slit resonance is $\eta_{\mathrm{res}} \sim 4.97$, and the maximum transmission cross section of the slit is $\sigma_{\mathrm{T}} \sim 382$ nm (Table 2.1).

The properties of resonant apertures, such as the subwavelength slit in a metal film that we consider here, can be described using temporal coupled-mode theory [19]. Coupled-mode theory describes the interaction between a resonator and the surrounding environment using channels that couple to the resonance [64, 65, 66]. For the slit resonator one type of channel consists of free space plane waves propagating in different directions above and below the film [19]. If the metal is plasmonic, there are additional channels which consist of plasmonic modes at the top and bottom metal film surfaces [19]. The theory also includes loss channels associated with material absorption [19]. Based on temporal coupled-mode theory, the maximum transmission cross section for a subwavelength slit in a perfect electrical conductor (PEC) film is λ_0/π [19], which for $\lambda_0 = 1.55$ μm gives $\lambda_0/\pi \sim 493$ nm. As expected, the maximum transmission cross section of the slit in a plasmonic metal ($\sigma_{\mathrm{T}} \sim 382$ nm) is smaller than the maximum transmission cross section of a similar slit in a PEC film due to the material losses in the plasmonic metal [19].

In Fig. 2.5, we show the profile of the magnetic field amplitude for the structure of Fig. 2.3, normalized with respect to the field amplitude of the incident plane wave. The profile is shown for a slit length of L=474 nm, which results in maximum transmission cross section per unit angle in the normal direction. We observe that, as expected for a subwavelength slit in a metallic film, the radiation pattern is almost isotropic [19]. The calculated directivity in the normal direction is $D(\theta = 0^o)$~0.969 (Table 2.1). The directivity is smaller than one due to the presence of surface plasmon modes at the top surface of the metal film [19]. A portion of the light power exiting the slit couples to these plasmonic modes. The calculated directivity of the structure D as a function of the angle θ with respect to the normal is shown in Fig. 2.8.

We next consider a structure with a single microcavity at each of the entrance and exit sides of the slit (Fig. 2.1 with $N = M = 1$). With such a structure we aim to increase both the transmission of light through the slit as well as the directivity in the normal direction [19]. We use a genetic global optimization algorithm in combination with FDFD [22, 63, 67] to optimize the width and length of the two microcavities in the structure for maximum transmission cross

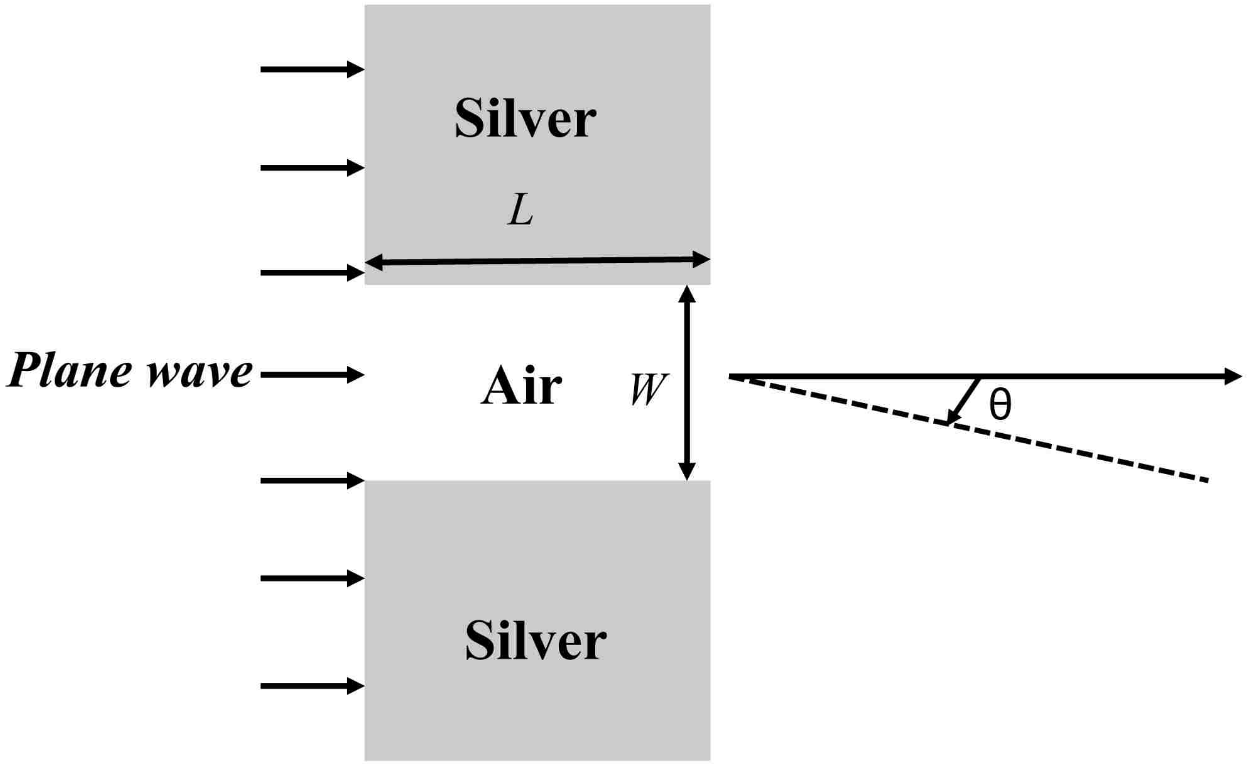

Figure 2.3: Schematic of a structure consisting of a single slit in a silver film.

section per unit angle in the normal direction $\sigma(\theta = 0^o)$. All structures are optimized at a single wavelength of λ_0=1.55 μm. However the structures can be designed to operate at other wavelengths in the near-infrared and visible. As mentioned above, all microcavity dimensions are limited to less than 1.6 μm, and we consider symmetric structures. The maximum normalized transmission cross section per unit angle in the normal direction for such a structure is found to be ~33.5 (Table 2.1). For such a structure the transmission cross section $\sigma_{\rm T1}$ of the corresponding silver-air-silver MDM waveguide is $\sigma_{\rm T1}$~169 nm (Table 2.1), which is slightly smaller than the cross section for a slit without microcavities ($\sigma_{\rm T1}$~184 nm). Thus, for the optimized $(N = 1, M = 1)$ structure the presence of the microcavity at the entrance side of the slit does not severely affect the coupling of the incident light into the slit mode. However, the presence of the microcavities at the entrance and exit sides of the slit results in significantly larger reflectivity $|r|^2$ at the sides of the slit compared to a slit without microcavities (Table 2.1). Thus, the resonance enhancement factor for the optimized $(N = 1, M = 1)$ structure is ~24.8 which is ~5 times larger than the one of the optimized reference

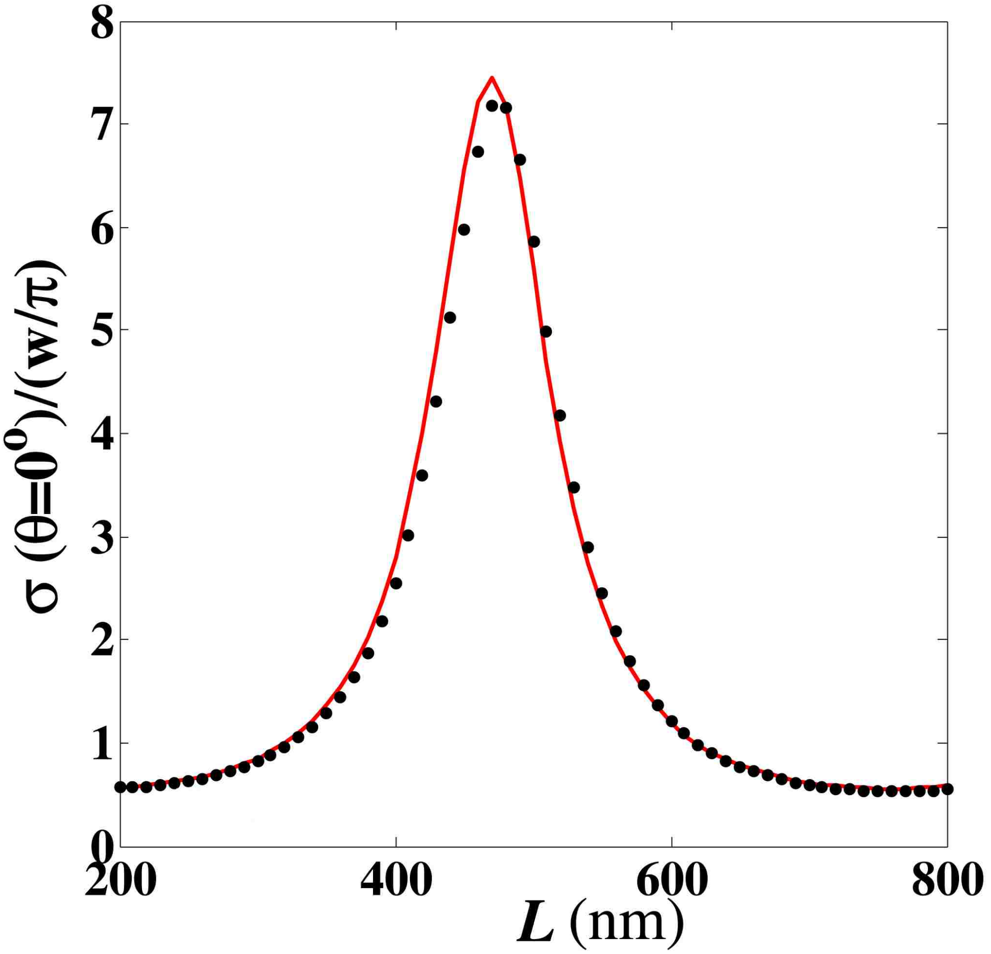

Figure 2.4: Normalized transmission cross section per unit angle σ in the normal direction ($\theta = 0^o$) for the structure of Fig. 2.3 as a function of slit length L calculated using FDFD (black dots) and scattering matrix theory (red solid line). Results are shown for w=50 nm and λ_0=1.55 μm.

slit without microcavities. In addition, the increased reflectivity at the sides of the slit leads to decrease of the power radiated from the slit. Thus, the power transmission coefficient of the slit for the optimized ($N = 1, M = 1$) structure is ∼2.6 times smaller than the one of the optimized reference slit without microcavities. Overall, the use of an optimized single microcavity at the entrance and exit sides of the slit results in a slit transmission cross section σ_{T}∼671 nm (Table 2.1), which is ∼1.8 times larger than the transmission cross section of the optimized slit without microcavities.

In Fig. 2.6, we show the profile of the magnetic field amplitude for the optimized ($N = 1, M = 1$) structure, normalized with respect to the field amplitude of the incident plane wave. We observe that for such a structure the directivity in the normal direction is increased compared to the slit without microcavities (Fig. 2.5), and the radiation pattern is anisotropic. The calculated directivity in the normal direction is $D(\theta = 0^o) {\sim} 2.51$ (Table 2.1), which is $\sim$2.6 times larger than the one of the optimized slit without microcavities. Overall, such a structure, when optimized, results in $1.8 \times 2.6 \sim 4.7$ times larger transmission cross section per unit angle in the normal direction compared to the optimized reference slit without microcavities (Fig. 2.3). The calculated directivity of the optimized $(N = 1, M = 1)$ structure D as a function of the angle θ with respect to the normal is shown in Fig. 2.8.

We note that the $(N = 1, M = 1)$ structure can be considered as a system of three coupled resonators (the slit and the two microcavities at the entrance and exit sides of the slit). These are also coupled to free space propagating plane waves above and below the structure as well as to plasmonic modes at the top and bottom metal film surfaces. The two microcavities are MDM waveguide resonators of width $w_{\mathrm{T1}} = w_{\mathrm{B1}}$ and length $d_{\mathrm{T1}} = d_{\mathrm{B1}}$. Due to the symmetry of the structure, normally incident plane waves can only excite even MDM modes in the microcavities. In addition, since the width of the optimized microcavities is smaller than the wavelength, only the fundamental MDM mode is propagating in the microcavities [60]. Since the width of the slit is much smaller than the width of the microcavities, the required length of the microcavities can be roughly estimated if the effect of the slit is ignored. Then each microcavity can be considered as a plasmonic transmission line resonator which is short-circuited on one side and open-circuited on the other [60]. Thus, the sum of the phases of the reflection coefficients at the two boundaries of the resonator is π. If we consider the Fabry-Perot resonance condition for the microcavities, we therefore find that the first resonant length of the microcavities is $\lambda_0/4$, which for $\lambda_0 = 1.55$ μm gives $\lambda_0/4 \sim 388$ nm. This rough estimate is close to the calculated optimized microcavity length $d_{\mathrm{T1}} = d_{\mathrm{B1}} = 430$ nm (Fig. 2.6).

To further enhance the transmission cross section per unit angle of the slit in the normal direction, we consider a structure with multiple microcavities at both the entrance and exit sides of the slit (Fig. 2.1). More specifically, we use the genetic optimization algorithm in combination

Table 2.1: Transmission cross sections σ_{T1} and σ_{T}, reflection coefficient r, resonance enhancement factor η_{res}, power transmission coefficient T, directivity in the normal direction $D(\theta = 0^o)$, and normalized transmission cross section per unit angle in the normal direction $\sigma(\theta = 0^o)/(w/\pi)$ calculated using scattering matrix theory and FDFD. Results are shown for the optimized structures of Fig. 2.1 with $(N, M) = (0, 0), (1, 1), (2, 2)$.

	(0,0)	(1,1)	(2,2)
σ_{T1}	184 nm	169 nm	645 nm
r	0.763 exp(2.56i)	0.916 exp(2.62i)	0.786 exp(2.62i)
η_{res}	4.97	24.8	5.81
T	0.418	0.160	0.382
σ_{T}	382 nm	671 nm	1432 nm
$D(\theta = 0^o)$	0.969	2.51	4.00
$\underset{\text{S-Matrix}}{\sigma(\theta = 0^o)/(w/\pi)}$	7.40	33.7	115
$\underset{\text{FDFD}}{\sigma(\theta = 0^o)/(w/\pi)}$	7.25	33.5	113

with FDFD to optimize the widths and lengths of the microcavities in a $(N = 2, M = 2)$ structure for maximum transmission cross section per unit angle in the normal direction $\sigma(\theta = 0^o)$. As before, the dimensions of the structures at both the entrance and exit sides of the slit are limited to less than 1.6 μm, and we consider symmetric structures. The maximum normalized transmission cross section per unit angle in the normal direction is found to be $\sim$113 (Table 2.1). For such a structure the transmission cross section σ_{T1} of the corresponding silver-air-silver MDM waveguide is $\sigma_{\mathrm{T1}}\sim$645 nm (Table 2.1), which is $\sim$3.5 larger than the cross section for a slit without microcavities ($\sigma_{\mathrm{T1}}\sim$184 nm). Thus, for the optimized $(N = 2, M = 2)$ structure the microcavities at the entrance side of the slit greatly enhance the coupling between free space waves and the slit mode. This is consistent with previous findings that optimized multisection structures can greatly improve the impedance matching and therefore the coupling between optical modes [22, 63]. In addition, for the optimized $(N = 2, M = 2)$ structure the reflectivity $|r|^2$ at the sides of the slit is only slightly larger than the one of a slit without microcavities (Table 2.1). Thus, the resonance enhancement factor η_{res} for the optimized $(N = 2, M = 2)$ structure is only slightly increased with respect to the optimized reference slit without microcavities (Table 2.1). Overall, the use of two optimized microcavities at the entrance and exit sides of the slit results in a slit transmission cross section $\sigma_{\mathrm{T1}}\sim$1432 nm (Table 2.1), which is $\sim$3.7 times larger than the transmission cross section of the optimized slit without microcavities. In addition, unlike the optimized single-microcavity structure in which the increased transmission is associated with increased resonance enhancement in the slit, for the optimized double-microcavity structure the increased transmission is mostly associated with improved impedance matching between free space waves and the slit mode.

In Fig. 2.7, we show the profile of the magnetic field amplitude for the optimized ($N = 2, M = 2$) structure, normalized with respect to the field amplitude of the incident plane wave. We observe that for such a structure the directivity in the normal direction is further increased compared to the optimized slit without microcavities (Fig. 2.5), and single-microcavity structure (Fig. 2.6). The calculated directivity in the normal direction is $D(\theta = 0^o)\sim 4$ (Table 2.1), which is ∼4.1 times larger than the one of the optimized reference slit without microcavities. Overall, the double-microcavity structure, when optimized, results in $3.7 \times 4.1 \sim 16$ times larger transmission cross section per unit angle in the normal direction compared to the optimized reference slit without microcavities (Fig. 2.3). The calculated directivity of the optimized ($N = 2, M = 2$) structure D as a function of the angle θ with respect to the normal is shown in Fig. 2.8. We observe that the radiation pattern of the optimized double-cavity structure is more anisotropic than the one of the optimized single-cavity structure.

All structures were optimized for maximum transmission cross section per unit angle in the normal direction at a single wavelength of λ_0=1.55 μm. In Fig. 2.9, we show the normalized transmission cross section per unit angle in the normal direction as a function of frequency for the optimized slit without microcavities (Fig. 2.5), single-microcavity (Fig. 2.6), and double-microcavity (Fig. 2.7) structures. We observe that in all cases the operation frequency range for high emission in the normal direction is broad. This is due to the fact that in all cases the enhanced emission in the normal direction is not associated with any strong resonances. In other words, the quality factors Q of the microcavity structures are relatively low. The full width at half maximum for the optimized double-microcavity structure is larger than the one of the optimized single-microcavity structure. This is due to the fact that, as mentioned above, for the optimized

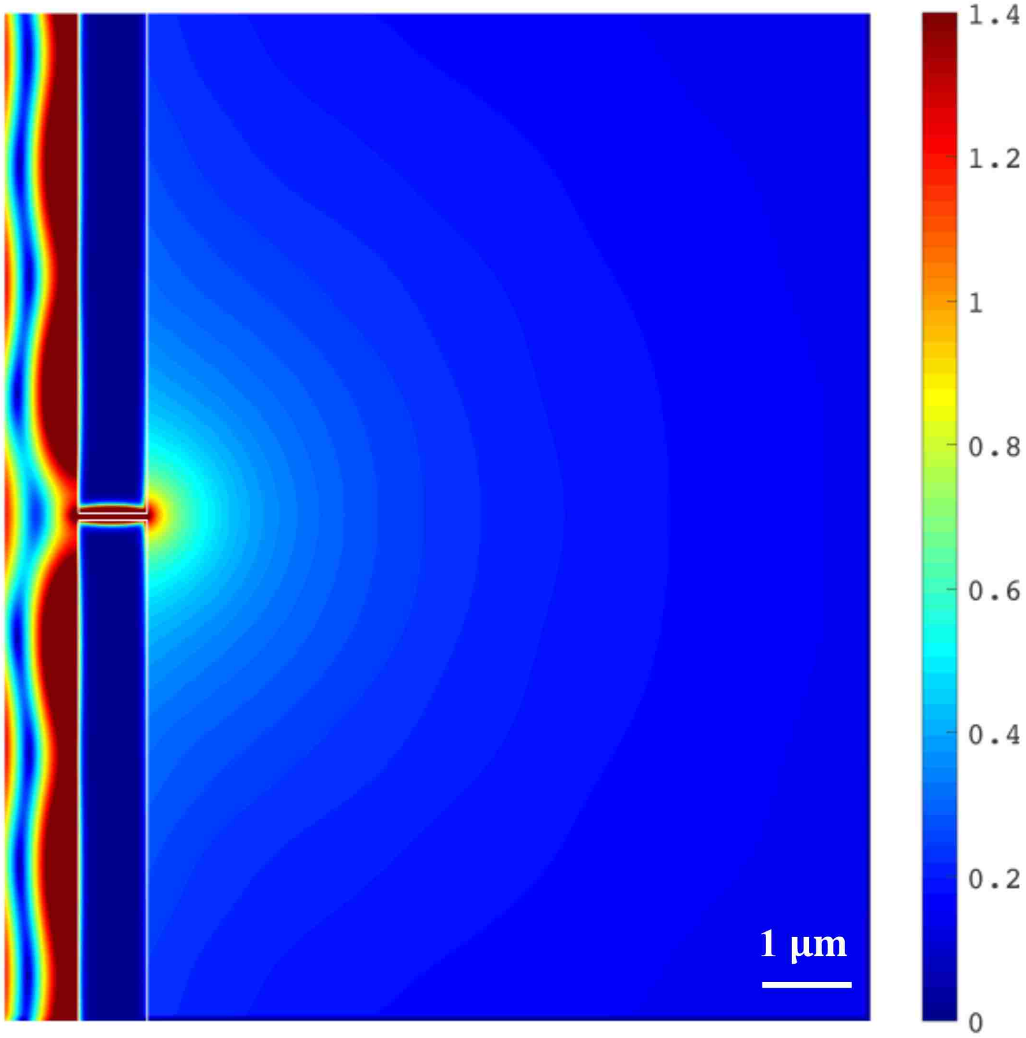

Figure 2.5: Profile of the magnetic field amplitude for the structure of Fig. 2.3, normalized with respect to the field amplitude of the incident plane wave. Results are shown for L=474 nm. All other parameters are as in Fig. 2.4.

single-microcavity structure the increased transmission is associated with a stronger slit resonance, while for the optimized double-microcavity structure the increased transmission is mostly associated with improved impedance matching. In Fig. 2.9 we also show the transmission cross section per unit angle in the normal direction for the optimized double-microcavity structure, if the metal in the structure is assumed to be lossless [$\epsilon_{\rm metal}$ =Re($\epsilon_{\rm metal}$), neglecting the imaginary part of the dielectric permittivity Im($\epsilon_{\rm metal}$)]. As expected, in the presence of loss, the transmission through the

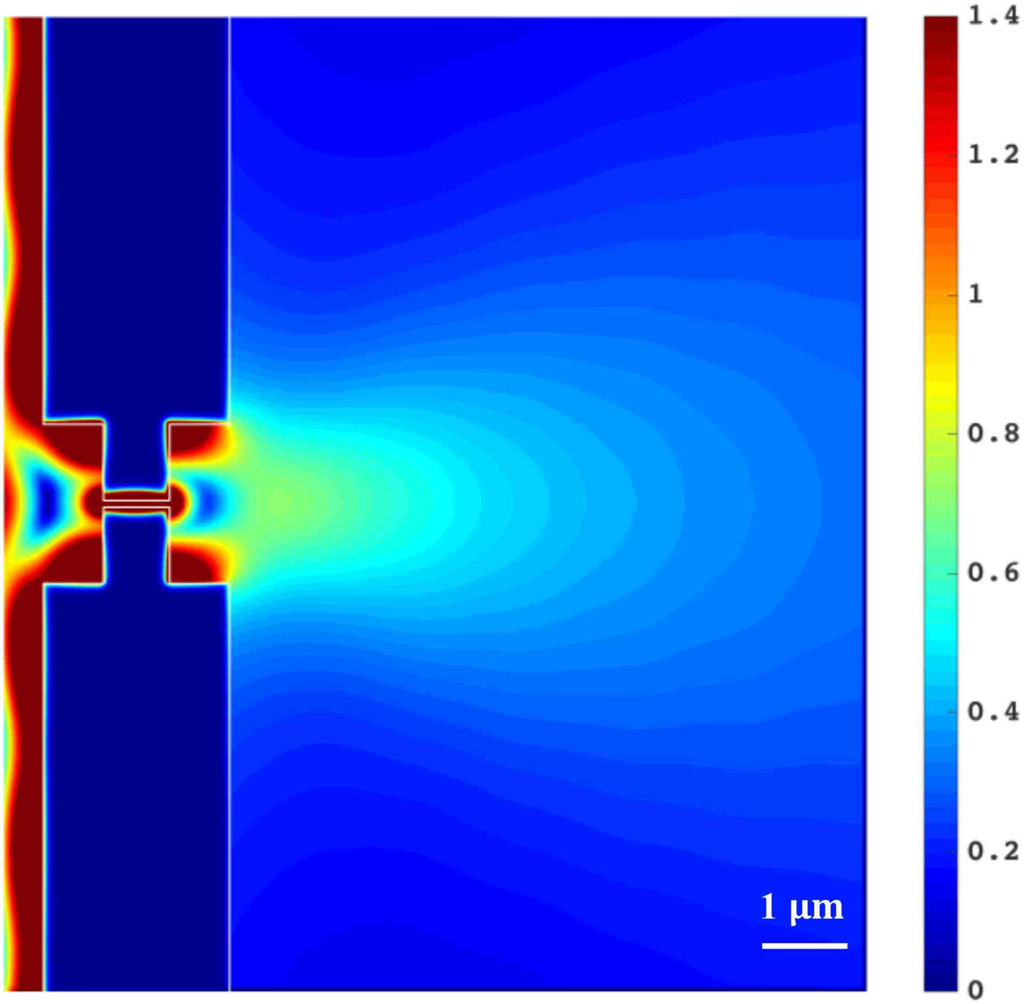

Figure 2.6: Profile of the magnetic field amplitude for the structure of Fig. 2.1, normalized with respect to the field amplitude of the incident plane wave. Results are shown for N=1, M=1, and optimized parameters of ($w_{\rm T1}$, $d_{\rm T1}$, $w_{\rm B1}$, $d_{\rm B1}$) = (1140, 430, 1140, 430) nm. All other parameters are as in Fig. 2.5.

structure decreases. However, this decrease is relatively small due to the compact wavelength-scale size of the structures.

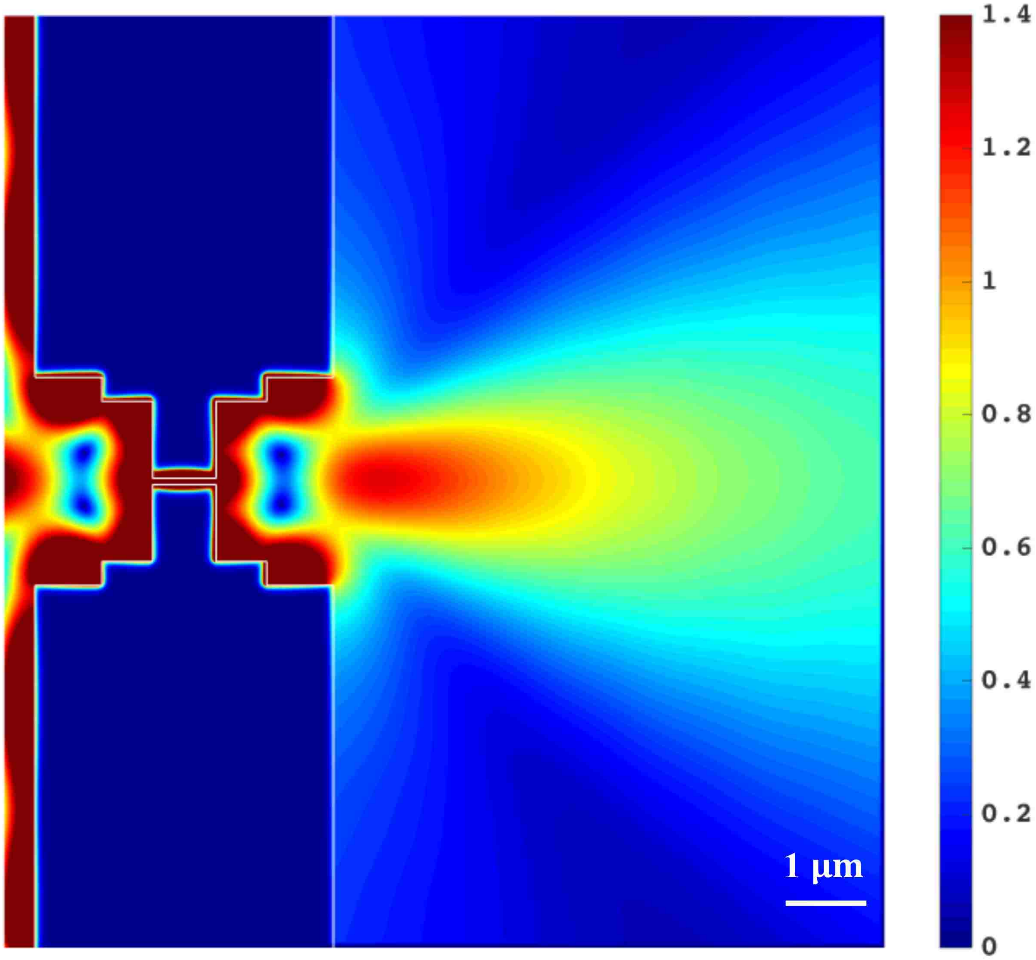

Figure 2.7: Profile of the magnetic field amplitude for the structure of Fig. 2.1, normalized with respect to the field amplitude of the incident plane wave. Results are shown for N=2, M=2, and optimized parameters of (w_{T1}, d_{T1}, w_{T2}, d_{T2}, w_{B1}, d_{B1}, w_{B2}, d_{B2}) = (1560, 500, 1200, 380, 1200, 380, 1560, 500) nm. All other parameters are as in Fig. 2.5.

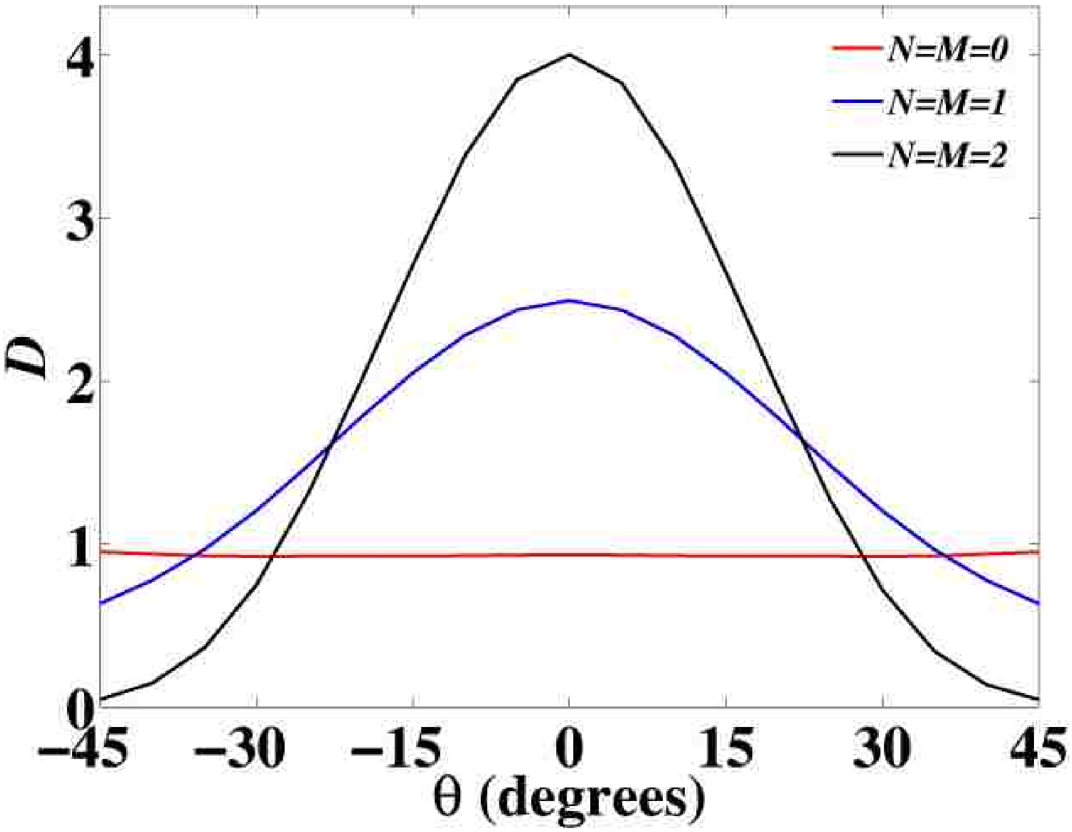

Figure 2.8: Directivity D as a function of the angle θ with respect to the normal for the optimized structures of Fig. 2.1 with N=M=0 (red line), N=M=1 (blue line), and N=M=2 (black line). All other parameters for the N=M=0, N=M=1, and N=M=2 cases are as in Figs. 2.5, 2.6, and 2.7, respectively.

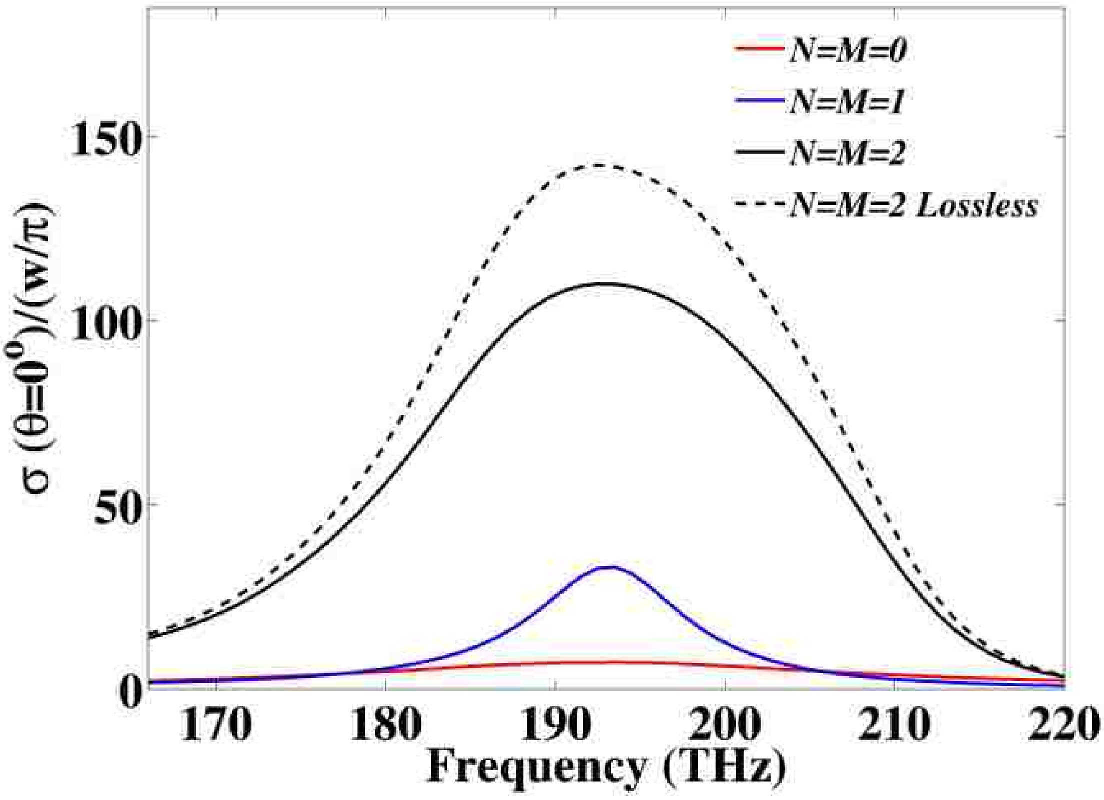

Figure 2.9: Normalized transmission cross section per unit angle σ in the normal direction ($\theta = 0^o$) as a function of frequency for the optimized structures of Fig. 2.1 with N=M=0 (red line), N=M=1 (blue line), and N=M=2 (black line). All other parameters for the N=M=0, N=M=1, and N=M=2 cases are as in Figs. 2.5, 2.6, and 2.7, respectively. Also shown is the transmission cross section per unit angle in the normal direction for the optimized $N = M = 2$ structure, if the metal in the structure is assumed to be lossless (black dashed line).

Chapter 3
Highly-compact magneto-optical switches for metal-dielectric-metal plasmonic waveguides

3.1 Introduction

Achieving active control of the flow of light in plasmonic devices is of fundamental interest in plasmonics. A possible route to actively control plasmons is to use an externally applied magnetic field [26, 27]. As an example, external magnetic fields could be used to control plasmonic devices through analogies of the Kerr and Faraday effects [28, 29]. Compared to electro-optics or thermo-optics, magneto-optics could lead to faster modulation speeds [27]. In addition, the magneto-optical effect breaks the time-reversal symmetry, and the use of magneto-optical materials may therefore lead to nonreciprocal plasmonic devices [68, 69, 33]. Surface plasmon polaritons propagating at metal-dielectric interfaces in which one or both media are magneto-optical have been investigated both theoretically and experimentally [70, 71, 72, 73, 74, 75, 76, 77].

In this Chapter, we introduce highly-compact resonant-cavity-enhanced magneto-optical switches for MDM plasmonic waveguides [78]. Based on the dispersion relation of the optical modes supported by a MDM waveguide in which the free-electron plasmonic metal is subject to an externally applied static magnetic field along the direction perpendicular to the plane of propagation, the field amplitude profile of the fundamental mode of the waveguide is asymmetric. The static magnetic field induced asymmetry, which can enhance or reduce the coupling between the waveguide and a side-coupled resonator, and the relatively large induced wave vector modulation can be used to design a Fabry-Perot cavity magneto-optical switch with a large modulation depth. The switch

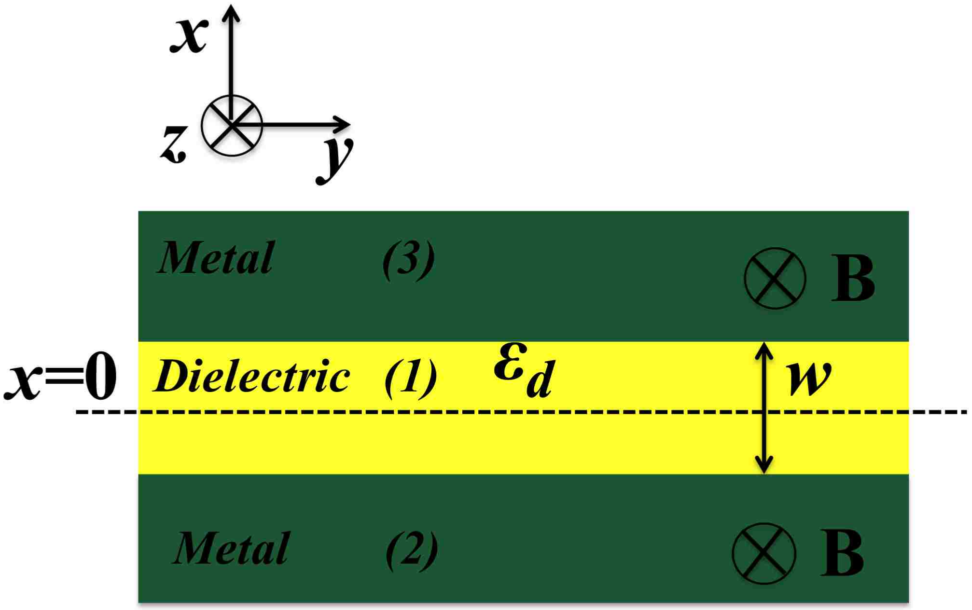

Figure 3.1: Schematic of a MDM waveguide. The metal is subject to an externally applied static magnetic field, and has a bulk plasmon wavelength $\lambda_P = \frac{2\pi c}{\omega_P}$, where c is the speed of light in vacuum.

consists of a MDM waveguide side-coupled to two MDM stub resonators, and the on and off states correspond to either the presence or the absence of the externally applied static magnetic field.

3.2 Results

A schematic of a MDM waveguide in which the metal is subject to an externally applied static magnetic field is shown in Fig. 3.1. Light in MDM waveguides can be coupled using a variety of structures such as gratings and slit-based couplers [79]. We consider TM modes, with non-zero field components E_x, E_y, and H_z. In the presence of a static magnetic field **B** in the z direction, the dielectric permittivity of the metal is described by a tensor [32, 33]:

$$\bar{\bar{\varepsilon}} = 1 - \frac{\omega_P^2}{(\omega + i/\tau)^2 - \omega_B^2} \times \begin{pmatrix} 1 + i\frac{1}{\tau\omega} & i\frac{\omega_B}{\omega} & 0 \\ -i\frac{\omega_B}{\omega} & 1 + i\frac{1}{\tau\omega} & 0 \\ 0 & 0 & \frac{(\omega+i/\tau)^2 - \omega_B^2}{\omega(\omega+i/\tau)} \end{pmatrix}, \tag{3.1}$$

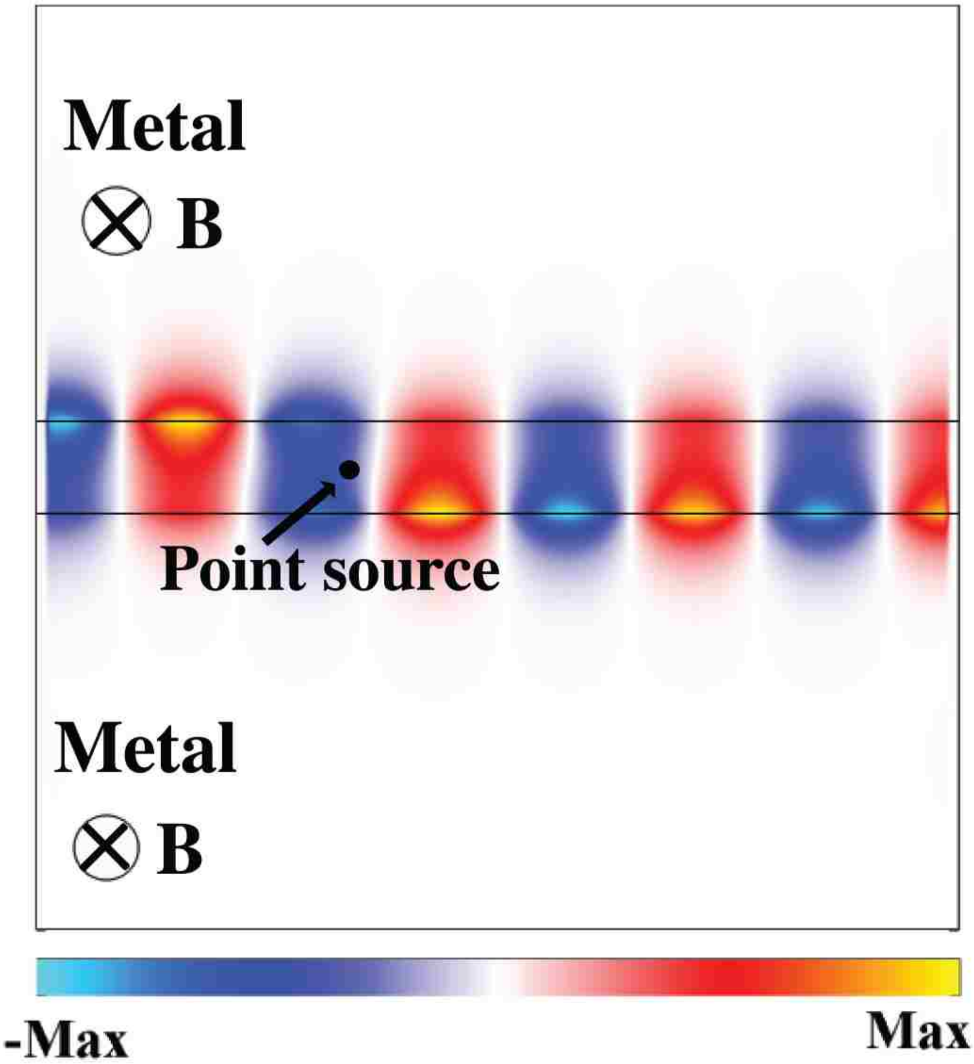

Figure 3.2: Magnetic field distribution of propagating waves excited by a dipole source placed in the MDM waveguide structure of Fig. 3.1, calculated using FDFD. Results are shown for $w = 0.37\lambda_P$, ϵ_d= 13.32, $\omega = 0.16\omega_P$, $\omega_B = 0.1\omega_P$, and $1/\tau = 0.002\omega_P$.

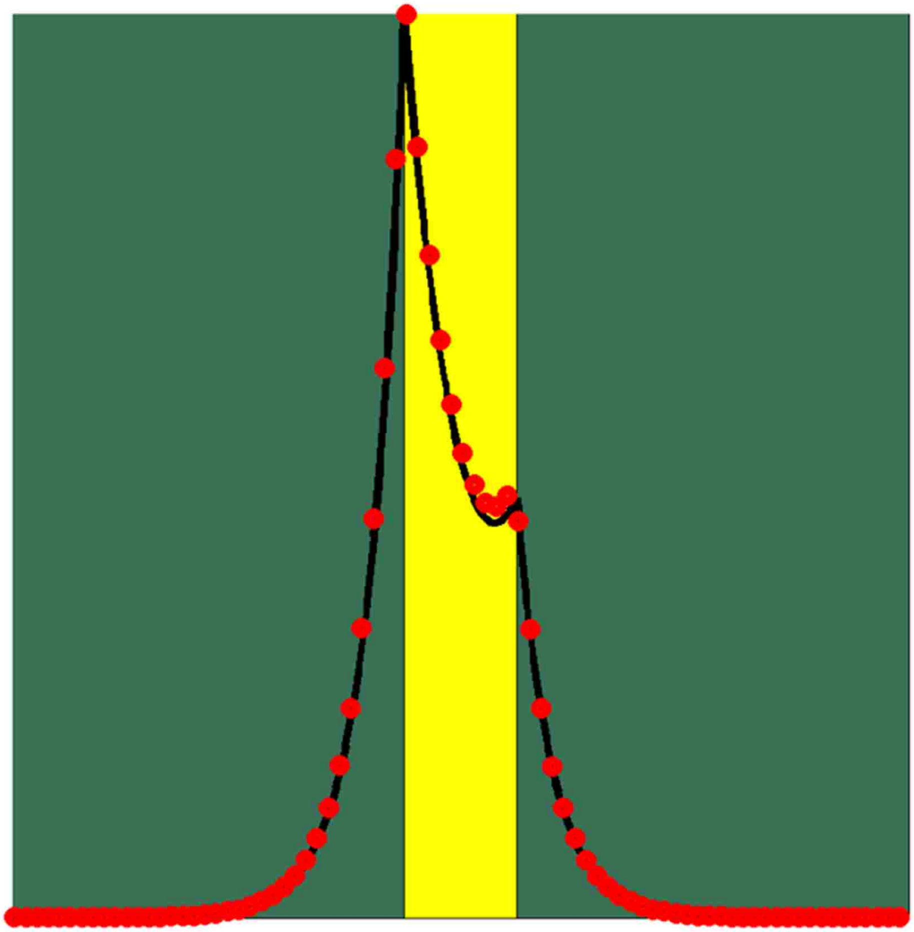

Figure 3.3: Magnetic field amplitude profile of the fundamental TM mode propagating in the positive y direction, calculated using FDFD (solid black lines), and analytically (red dots).

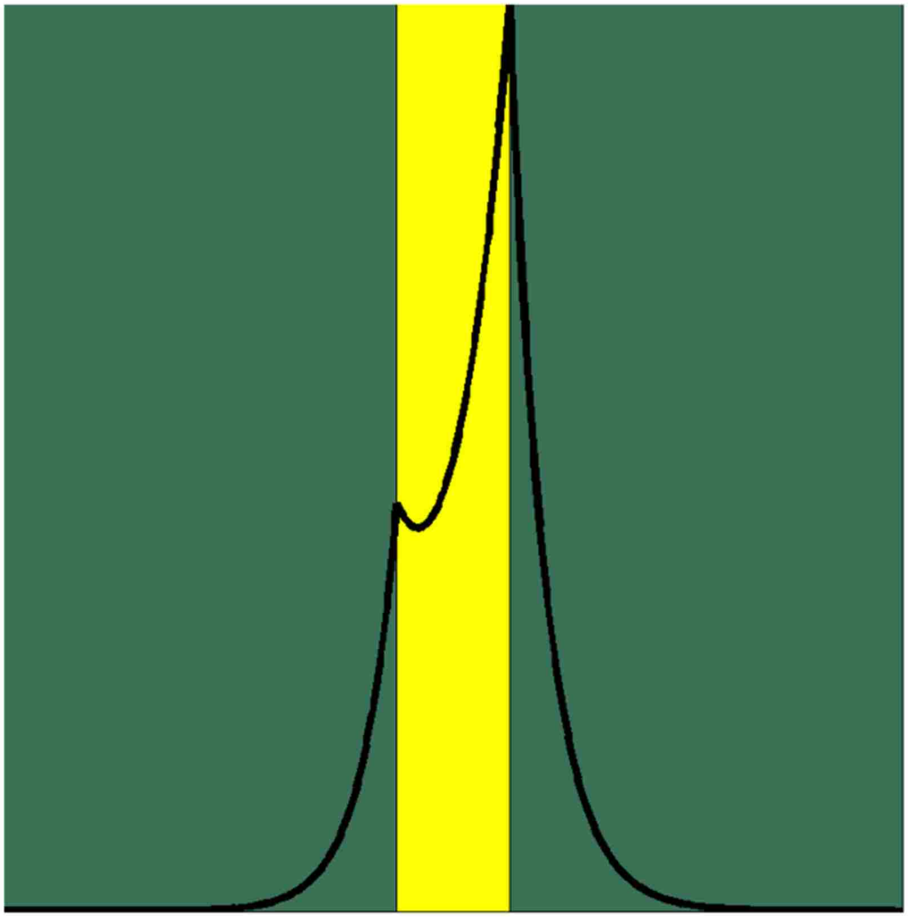

Figure 3.4: Magnetic field amplitude profile of the fundamental TM mode propagating in the negative y direction, calculated using FDFD (solid black lines).

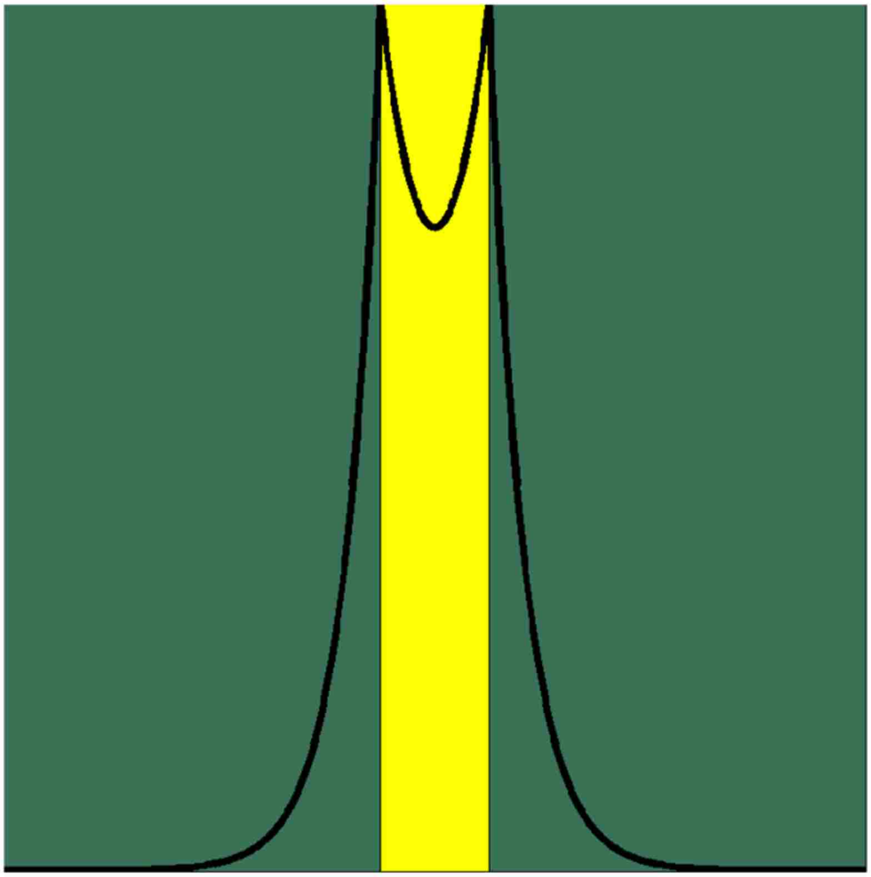

Figure 3.5: Magnetic field amplitude profile of the fundamental propagating TM mode for $\omega_B = 0$.

where ω_P is the bulk plasmon frequency, and $\omega_B = \frac{eB}{m}$ is the cyclotron frequency. The decay time τ characterizes the material loss in the metal, e is the electron charge, and m is the electron mass. Here we use $1/\tau = 0.002\omega_P$. By applying the boundary conditions at the metal-dielectric interfaces, one can derive the following dispersion relation for the optical modes supported by the structure of Fig. 3.1 [80]:

$$\exp(2k_d w) = \frac{\left(\frac{k\varepsilon_{xy}}{\varepsilon_{xx}\varepsilon_m}\right)^2 + (k_d/\varepsilon_d - k_m/\varepsilon_m)^2}{\left(\frac{k\varepsilon_{xy}}{\varepsilon_{xx}\varepsilon_m}\right)^2 + (k_d/\varepsilon_d + k_m/\varepsilon_m)^2}, \tag{3.2}$$

where $\varepsilon_m = \varepsilon_{xx} + \varepsilon_{xy}^2/\varepsilon_{xx}$, k is the y component of the wave vector, $k_i = \sqrt{k^2 - k_0^2\varepsilon_i}, i = d, m$, and w is the width of dielectric region (Fig. 3.1). [Equation (3.2) is proved in Appendix A]. We observe that the above dispersion relation depends only on the square of the propagation constant k. As a result, the propagation constants for the modes propagating in the positive and negative y direction are the same.

We found, however, that the corresponding field profiles are different. In Fig. 3.2 we show the magnetic field distribution of propagating waves excited by a dipole source placed in the MDM waveguide structure of Fig. 3.1 calculated with the FDFD method [56]. We observe that, even though the right-moving and left-moving modes have the same propagation constant, the field amplitude of the right-moving (left-moving) mode is larger at the lower (upper) metal-dielectric interface.

In the absence of an externally applied static magnetic field, the magnetic field amplitude profile of the fundamental TM mode supported by the MDM waveguide has a maximum at the two metal-dielectric interfaces, and is exponentially decaying in the metal. The profile is symmetric with respect to the $x = 0$ mirror plane in the middle of the dielectric layer (Fig. 3.5).

However, in the presence of an externally applied static magnetic field $\mathbf{B}$, the magnetic field amplitude profile of the fundamental mode of the MDM waveguide becomes asymmetric. As in the case of no externally applied static magnetic field, the profile has a maximum at the two metal-dielectric interfaces, and the field amplitude is exponentially decaying in the metal. However, the maximum field amplitudes at the two interfaces are different, resulting in the asymmetry of the profile [75] (Figs. 3.3, 3.4). In addition, because of the symmetry of the waveguide structure, the magnetic field amplitude profile of the mode propagating in the negative y direction is the mirror image with respect to the $x = 0$ plane of the profile of the mode propagating in the positive y direction (Figs. 3.3, 3.4). Note that for applied magnetic field with opposite orientations below and above the dielectric there is no asymmetry in the magnetic field amplitude profile.

In Fig. 3.3, in addition to the numerically calculated magnetic field amplitude profile obtained with FDFD, we also show the analytically calculated profile, obtained by solving the dispersion relation of the modes supported by the waveguide (Eq. 3.2). We observe that there is excellent agreement between the analytical results and the numerical results obtained using the FDFD method. This demonstrates that the FDFD method that we use to model the MDM waveguide, in which the metal is subject to an externally applied static magnetic field, is indeed valid and appropriate for investigating the properties of such structures.

We now consider the effect of the externally applied static magnetic field on the propagation constant of the mode. In Fig. 3.6 we show the real part of the propagation constant in the absence ($\omega_B = 0$) and presence ($\omega_B = 0.1\omega_P$) of the static magnetic field as a function of frequency. We observe that the real part of the propagation constant of the waveguide mode in the presence of the magnetic field $\mathrm{Re}[k(\omega_B = 0.1\omega_P)]$ is larger than the real part of the propagation constant of the mode in the absence of the magnetic field $\mathrm{Re}[k(\omega_B = 0)]$. This is consistent with the dispersion relation of the modes (Eq. 3.2). To see this, for simplicity we first consider the lossless case ($1/\tau = 0$). Since for metals $\varepsilon_{xx} < 0$, we have $\varepsilon_m < 0$. In addition, the amplitude of ε_m increases when the external static magnetic field $\mathbf{B}$ is applied. As a result, the right hand side of Eq. 3.2 increases, and consequently k_d, and therefore k also increase, when the external static magnetic field $\mathbf{B}$ is applied. Similarly, if the effect of the loss is included ($1/\tau = 0.002\omega_P$), the real part of k increases, when the magnetic field $\mathbf{B}$ is applied (Fig. 3.6).

We also define the magnetic field induced wave vector modulation as $|\Delta k(\omega_B)/k| \equiv |\frac{k(\omega_B)-k(\omega_B=0)}{k(\omega_B=0)}|$. We observe that, as the frequency increases, both the magnetic field induced change in the propagation constant (Fig. 3.6), as well as the magnetic field induced wave vector modulation (Fig. 3.7) increase. This is associated with the fact that the fraction of the modal power in the metal increases, as the frequency increases [81]. Thus, the effect of the magnetic field induced change in the dielectric permittivity of the metal on the propagation constant of the mode becomes larger, as the frequency increases.

In Fig. 3.7 we also show the effect of the dielectric permittivity ε_d of the material between the two metal regions of the MDM waveguide on the wave vector modulation $|\Delta k(\omega_B)/k|$. It is known that in a plasmonic MDM waveguide, as the permittivity of the dielectric increases, the fraction of the modal power in the metal increases [81]. Thus, we expect that the wave vector modulation $|\Delta k(\omega_B)/k|$ will increase, as the dielectric permittivity of the material between the two metal regions ε_d increases. This is indeed verified by the results shown in Fig. 3.7. The relatively large magnetic field induced wave vector modulation obtained for large ε_d can be beneficial in designing Fabry-Perot cavity magneto-optical switches [82], as we will see below.

As before, in Figs. 3.6 and 3.7, in addition to the numerically calculated results obtained with FDFD for the propagation constant of the mode and the magnetic field induced wave vector modulation, we also show the analytically calculated results, obtained by solving the dispersion relation of the modes supported by the waveguide (Eq. 3.2). Once again, we observe that there is excellent agreement between the analytical results and the numerical results obtained using the FDFD method in the whole range of parameters considered. This further demonstrates that the FDFD method that we use is appropriate for investigating the properties of such structures.

As a first step towards designing a Fabry-Perot cavity magneto-optical switch based on the structure of Fig. 3.1, we investigate a MDM waveguide side-coupled to a MDM stub resonator, when the metal is subject to an externally applied static magnetic field (Fig. 3.8). In Fig. 3.9 we show the transmission as a function of the stub length L_1 for the structure of Fig. 3.8. We excite the fundamental mode of the input waveguide using a point current source, and measure the power of the transmitted optical mode in the output waveguide (Fig. 3.8). We perform a similar

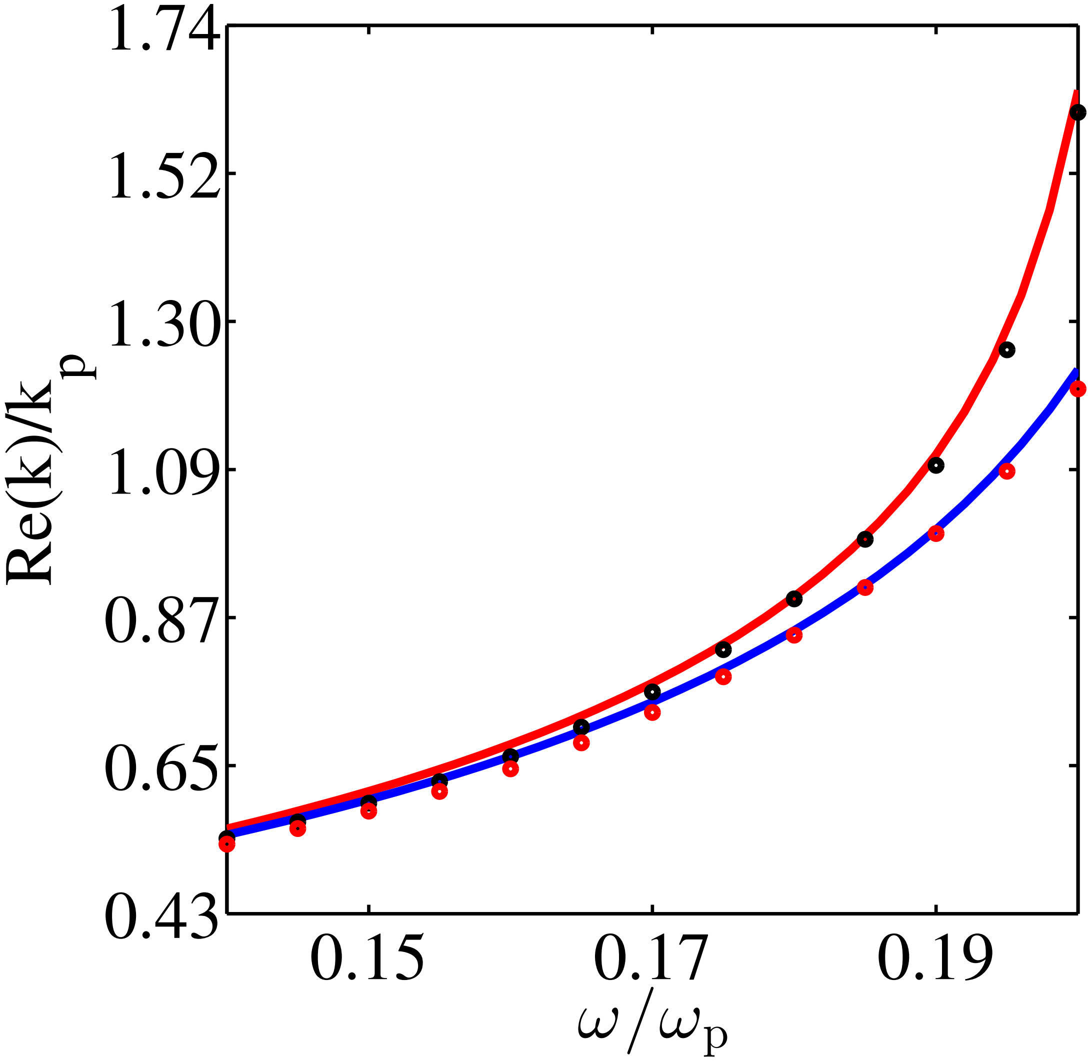

Figure 3.6: Real part of the y component of the wave vector, normalized by $k_P = \omega_P/c$, as a function of frequency, calculated using FDFD for $\omega_B = 0.1\omega_P$ (black dots), and $\omega_B = 0$ (red dots). Also shown are analytically calculated results for $\omega_B = 0.1\omega_P$ (red solid line), and $\omega_B = 0$ (blue solid line).

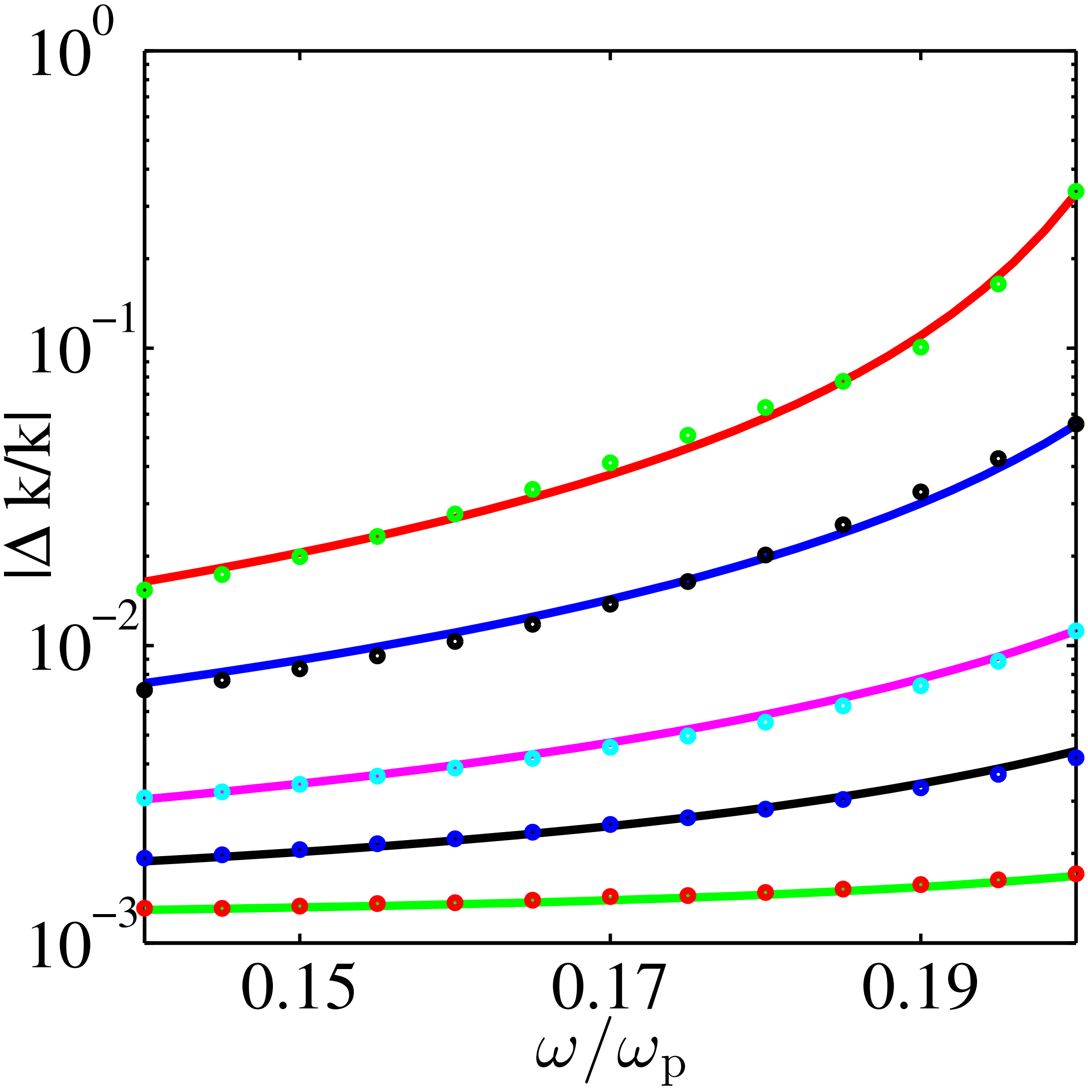

Figure 3.7: Normalized amplitude of the change in the y component of the wave vector, when the static magnetic field is applied to the metal, as a function of frequency, calculated using FDFD for ϵ_d=1 (red dots), ϵ_d=3 (blue dots), ϵ_d=5 (light blue dots), ϵ_d=9 (black dots), and ϵ_d= 13.32 (green dots). Also shown are analytically calculated results for ϵ_d=1 (solid green line), ϵ_d=3 (solid black line), ϵ_d=5 (solid pink line), ϵ_d=9 (solid blue line), and ϵ_d= 13.32 (solid red line).

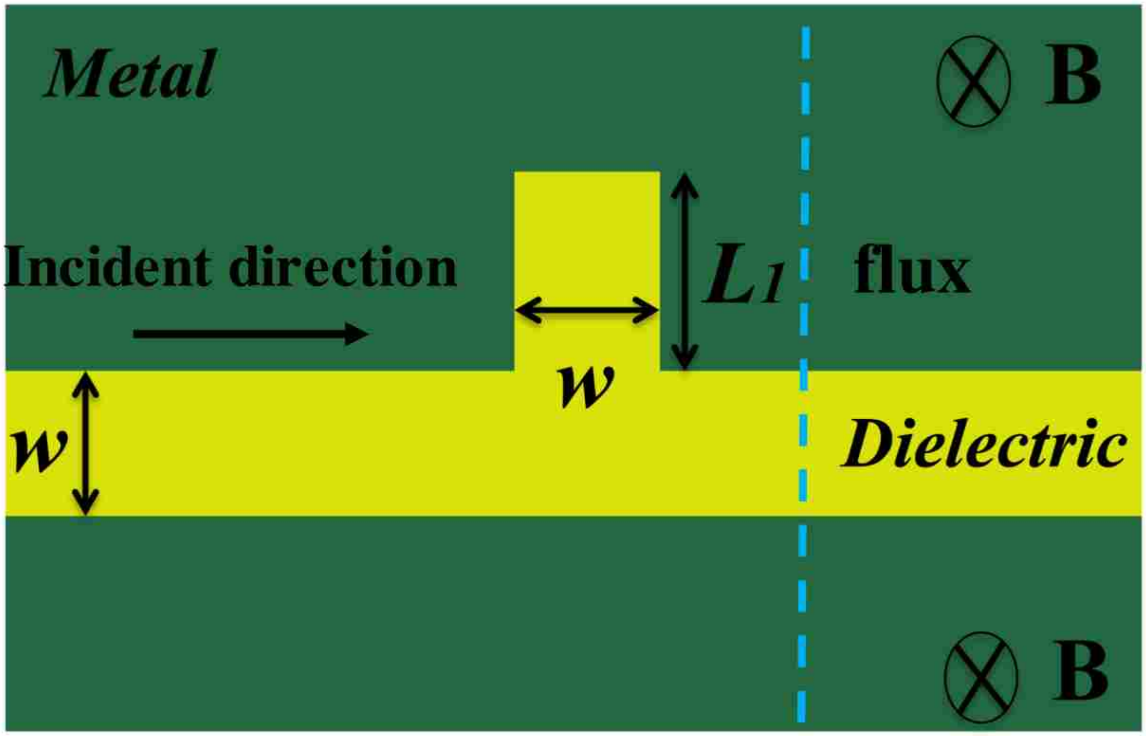

Figure 3.8: Schematic of a MDM waveguide side-coupled to a MDM stub resonator. The metal is subject to an externally applied static magnetic field. The dashed line indicates the flux measurement plane.

simulation in a straight waveguide and the ratio of the power measured in the structure with respect to the power measured in the straight waveguide is the transmission of the structure. In the absence of an externally applied static magnetic field ($\omega_B = 0$), the transmission exhibits a dip when L_1 is equal to one of the resonant lengths of the cavity [82]. The transmission at this length is relatively low, since the incoming wave interferes destructively with the decaying amplitude into the forward direction of the resonant cavity field [62]. In the presence of an externally applied static magnetic field **B**, the transmission for the structure of Fig. 3.8 depends on the direction of the static magnetic field. When the static magnetic field is in the positive z direction ($\omega_B = 0.1\omega_P$), the magnetic field amplitude of the fundamental mode of the MDM waveguide is larger at the lower metal-dielectric interface (Fig. 3.3). Thus, the coupling between the waveguide and the stub resonator, which is side-coupled at the upper metal-dielectric interface, is weaker compared to the case of no externally applied static magnetic field. As a result, the on-resonance dip in transmission is smaller (Fig. 3.9). We also observe a shift in the resonant lengths, associated with the change in the propagation constant of the mode in the presence of the static magnetic field (Fig. 3.2). In contrast, when the static magnetic field is in the negative z direction ($\omega_B = -0.1\omega_P$), the magnetic field amplitude of the fundamental mode of the MDM waveguide is larger at the upper metal-dielectric interface (Fig. 3.4). Thus, the coupling between the waveguide and the stub resonator is stronger. As a result, the transmission is lower compared to the case of no externally applied static magnetic field both off-resonance and on-resonance (Fig. 3.9).

We now investigate a Fabry-Perot cavity structure consisting of a MDM waveguide side-coupled to two MDM stub resonators, when the metal region between the two stubs is subject to an externally applied static magnetic field **B** (Fig. 3.10). Since only the fundamental mode is propagating in each waveguide section, we can use a single-mode scattering matrix theory to account for the behavior of this system. The transmission for the structure of Fig. 3.10 can be calculated using

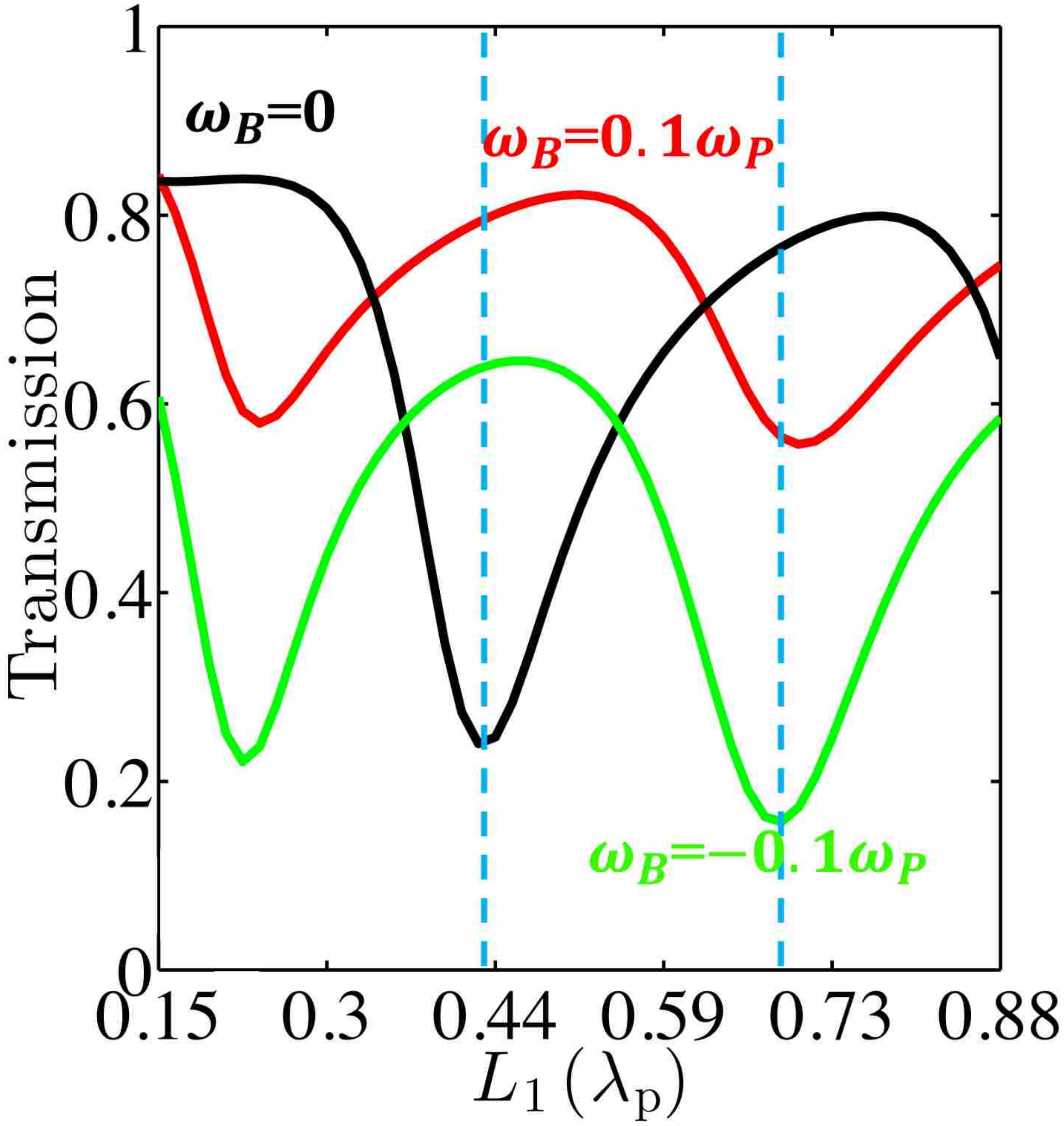

Figure 3.9: Transmission as a function of the stub length L_1 for the structure of Fig. 3.8. Results are shown for $\omega_B = 0$ (black line), $\omega_B = 0.1\omega_P$ (red line), and $\omega_B = -0.1\omega_P$ (green line). All other parameters are as in Fig. 3.2. The vertical dashed lines correspond to $L_1 = 0.43\lambda_P$, and $L_1 = 0.67\lambda_P$.

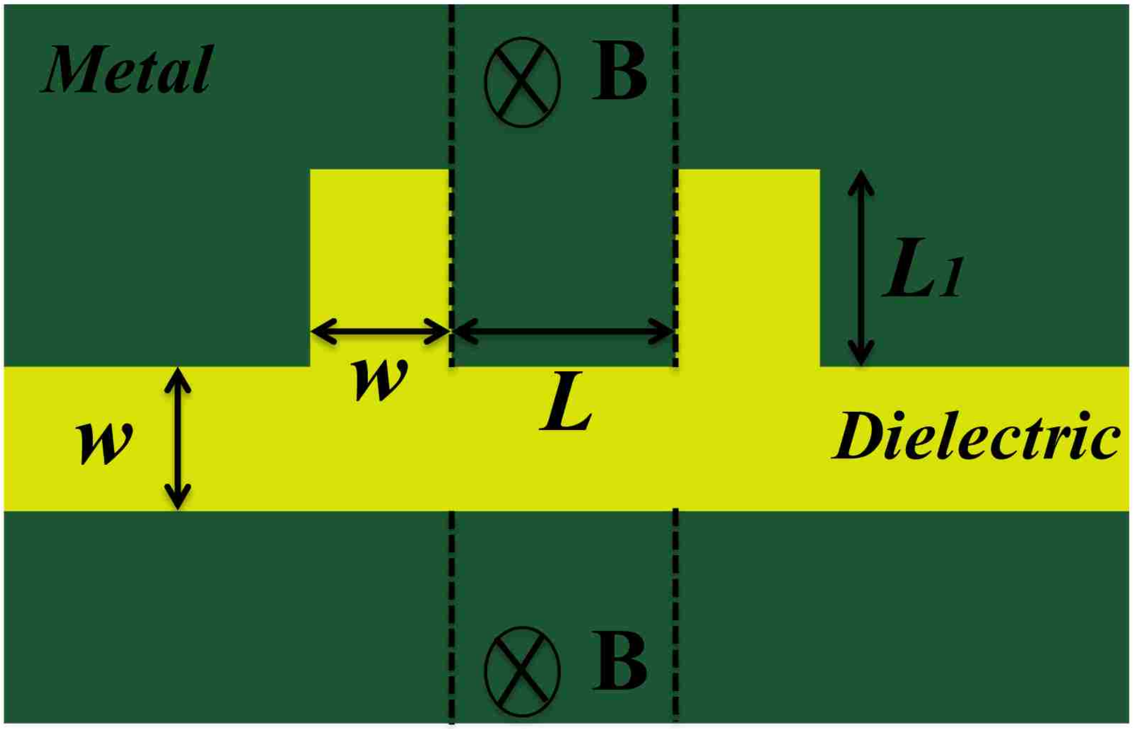

Figure 3.10: Schematic of a Fabry-Perot cavity structure consisting of a MDM waveguide side-coupled to two MDM stub resonators. The metal region between the two stubs is subject to an externally applied static magnetic field.

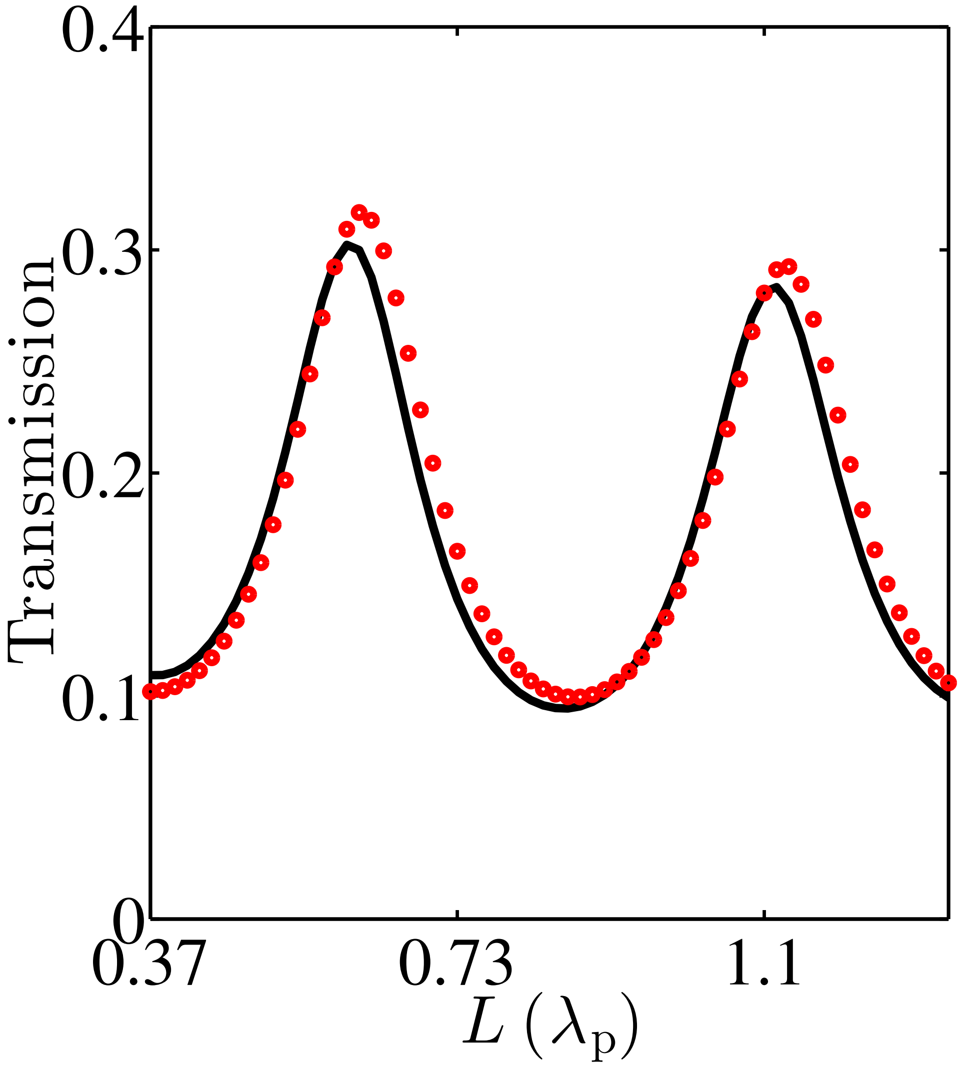

Figure 3.11: Transmission as a function of the distance L between the two stubs for the structure of Fig. 3.10 calculated using FDFD (black solid line) and scattering matrix theory (red dots). Results are shown for $L_1 = 0.43\lambda_P$.

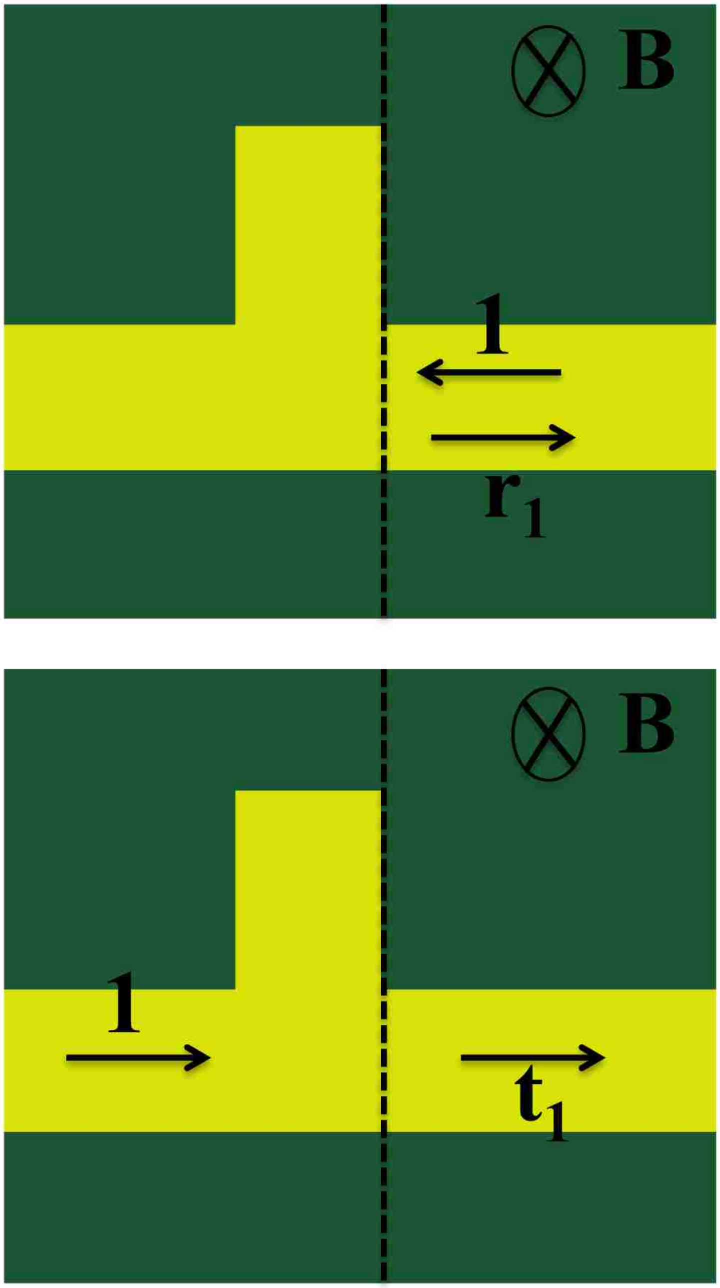

Figure 3.12: Schematics defining the transmission and reflection coefficients when the metal region to the right of the stub is subject to a static magnetic field.

scattering matrix theory as [60]:

$$T = \left|\frac{t_1 t_2 e^{-kL}}{1 - r_1 r_2 e^{-2kL}}\right|^2, \tag{3.3}$$

where t_1 and r_1 (t_2 and r_2) are the numerically extracted using FDFD [60] complex magnetic field transmission and reflection coefficients, respectively, when the metal region to the right (left) of the stub is subject to a static magnetic field (Fig. 3.12). [Equation (3.3) is proved in Appendix B]. We observe that there is excellent agreement between the scattering matrix theory results and the exact results obtained using FDFD. The transmission as a function of the distance L between the two stubs exhibits peaks, corresponding to the Fabry-Perot resonances of the cavity (Fig. 3.11).

For a MDM waveguide side-coupled to a single stub with a length of $L_1 = 0.43\lambda_P$, there is a significant difference between the transmission in the absence of an externally applied static magnetic field ($\omega_B = 0$) and the transmission when the static magnetic field is in the positive z direction ($\omega_B = 0.1\omega_P$) (Fig. 3.9). This significant difference in transmission can be used to design a Fabry-Perot cavity magneto-optical switch consisting of a MDM waveguide side-coupled to two MDM stub resonators, in which the metal is subject to an externally applied static magnetic field (Fig. 3.13). By using two stubs and properly tuning the length of the cavity L formed between them, the difference in transmission between the on and off states [Fig. 3.14(a)], and therefore the modulation depth of the switch, defined as $[T(\omega_B = 0.1\omega_P) - T(\omega_B = 0)]/T(\omega_B = 0.1\omega_P)$ [Fig. 3.14(b)], can be resonantly enhanced compared to the single-stub structure. Thus, such a Fabry-Perot cavity structure can act as a magneto-optical switch, in which the on/off states correspond to the presence/absence of externally applied static magnetic field.

Similarly, for a waveguide side-coupled to a single stub with a length of $L_1 = 0.67\lambda_P$, there is a significant difference between the transmission in the absence of an externally applied static magnetic field ($\omega_B = 0$) and the transmission when the static magnetic field is in the negative z direction ($\omega_B = -0.1\omega_P$) (Fig. 3.9). Again, this difference in transmission can be used to design a Fabry-Perot cavity magneto-optical switch consisting of a MDM waveguide side-coupled to two

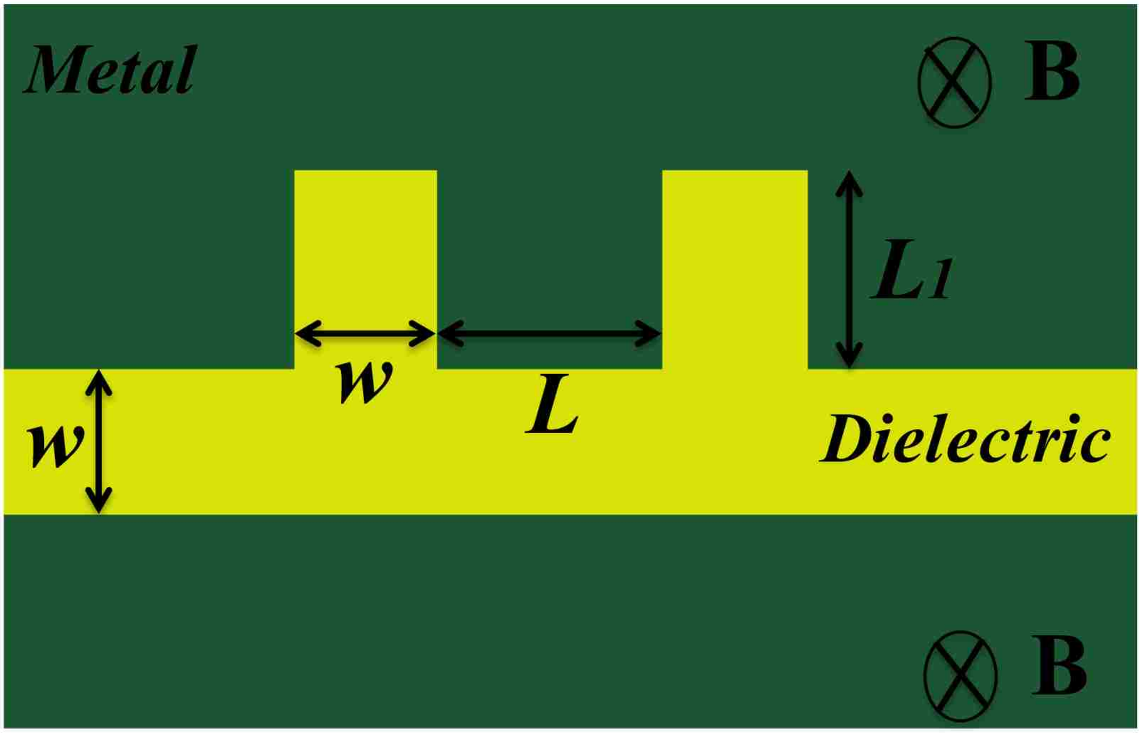

Figure 3.13: Schematic of a Fabry-Perot cavity structure consisting of a MDM waveguide side-coupled to two MDM stub resonators. The metal is subject to an externally applied static magnetic field.

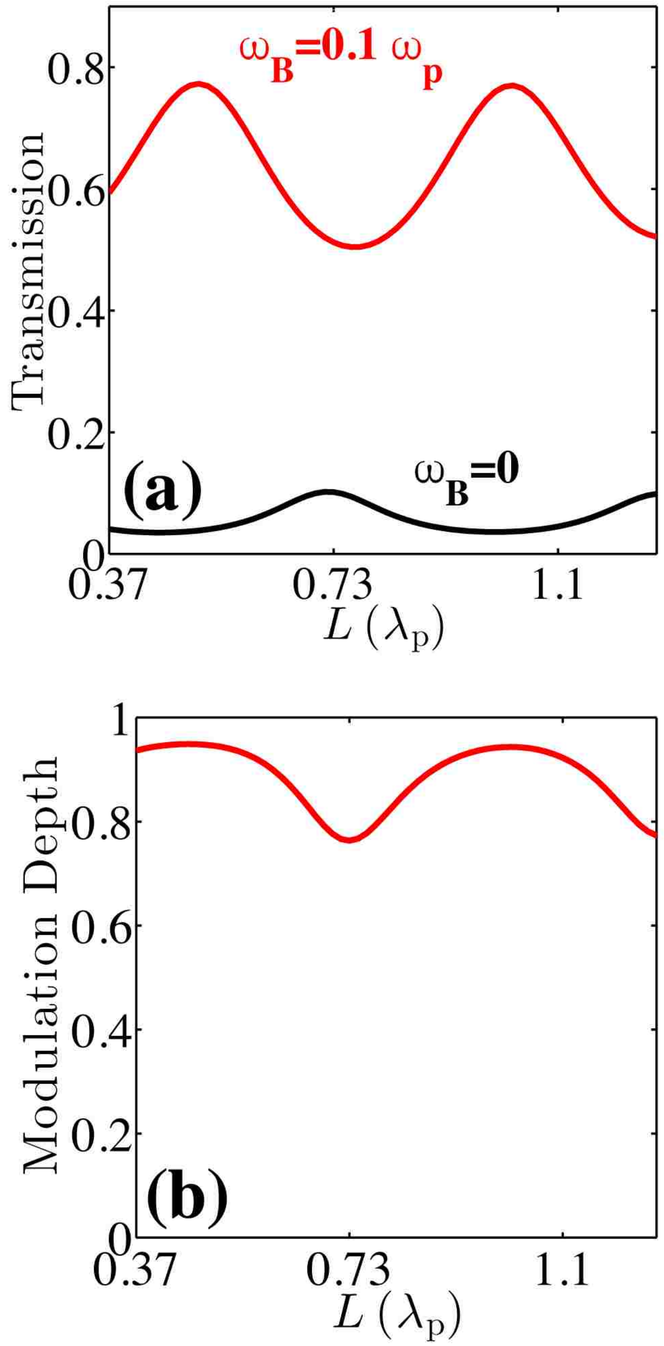

Figure 3.14: (a) Transmission as a function of the distance L between the two stubs for the structure of Fig. 3.13 calculated using FDFD for $\omega_B = 0$ (black line) and $\omega_B = 0.1\omega_P$ (red line). Results are shown for $L_1 = 0.43\lambda_P$. All other parameters are as in Fig. 3.2. (b) Modulation depth $[T(\omega_B = 0.1\omega_P) - T(\omega_B = 0)]/T(\omega_B = 0.1\omega_P)$ as a function of L for the structure of Fig. 3.13. All parameters are as in Fig. 3.14(a).

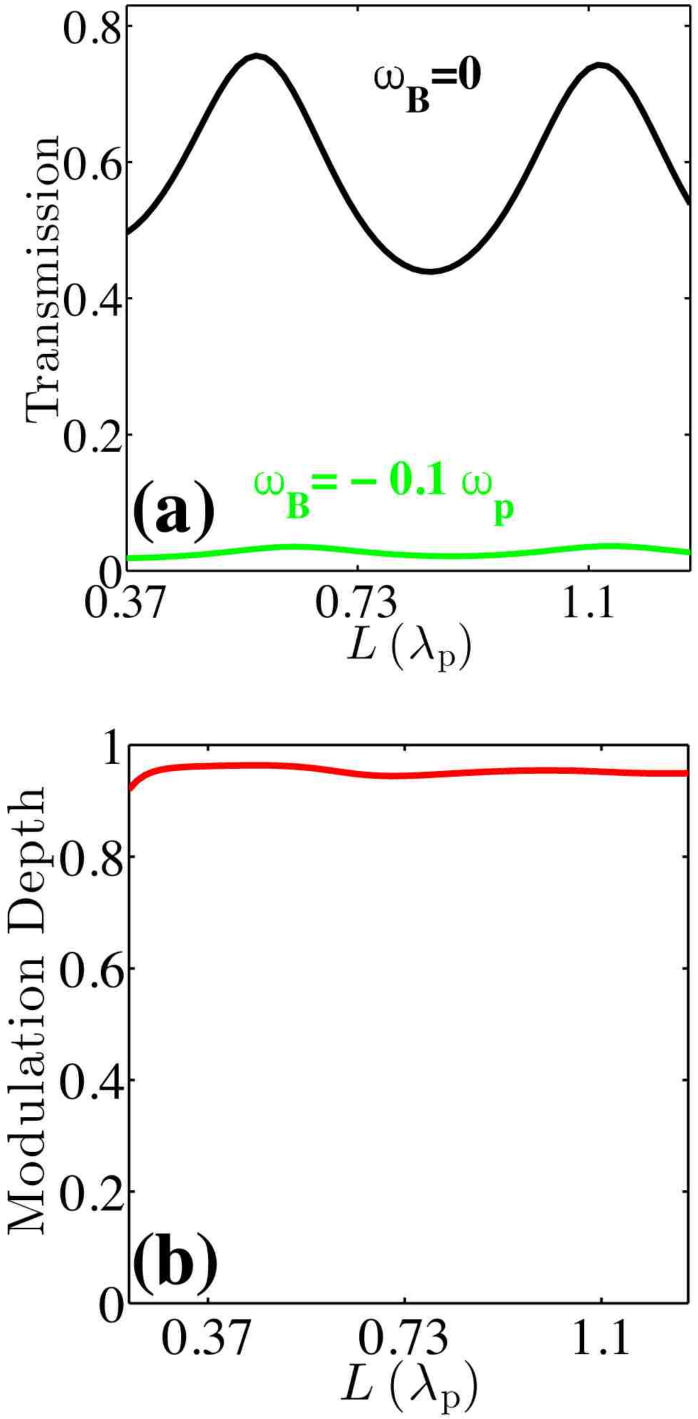

Figure 3.15: (a) Transmission as a function of L for the structure of Fig. 3.13 calculated using FDFD for $\omega_B = 0$ (black line) and $\omega_B = -0.1\omega_P$ (green line). Results are shown for $L_1 = 0.67\lambda_P$. All other parameters are as in Fig. 3.2. (b) Modulation depth $[T(\omega_B = 0) - T(\omega_B = -0.1\omega_P)]/T(\omega_B = 0)$ as a function of L for the structure of Fig. 3.13. All parameters are as in Fig. 3.15(a).

MDM stub resonators (Fig. 3.13), in which the on/off states correspond to the absence/presence of externally applied static magnetic field [Figs. 3.15(a), 3.15(b)]. Since the transmission for the single stub structure for $\omega_B = -0.1\omega_P$, $L_1 = 0.67\lambda_P$ is smaller than the one for $\omega_B = 0$, $L_1 = 0.43\lambda_P$ (Fig. 3.9), the transmission in the off state is smaller for the double stub structure corresponding to Figs. 3.15(a), 3.15(b) compared to the one corresponding to Figs. 3.14(a), 3.14(b). As a result, the modulation depth as a function of the length of the cavity L is more uniform for the structure corresponding to Figs. 3.15(a), 3.15(b).

As final remarks, a free-electron plasmonic material with the required properties is indium antimonide (InSb). For such a material the bulk plasmon frequency is $\omega_P \simeq 12.57 \times 10^{12}$ rad/sec ($\lambda_P \simeq 150$ μm) [83], and thus $\omega_B = 0.1\omega_P$ corresponds to an externally applied static magnetic field of $B = 0.1$T. The corresponding dimensions of the structure are $(w, L, L_1) \simeq$ (55.5,166.5,100.5) μm. In addition, the loss parameter used in this Chapter ($1/\tau = 0.002\omega_P$) is appropriate for indium antimonide [84, 83]. We also found that even for a significantly larger loss parameter of $1/\tau = 0.01\omega_P$ the modulation depth is $\sim$0.54 which is acceptable for switching applications [12]. In addition, for the structure corresponding to Figs. 3.15(a), 3.15(b) the transmission for $\omega_B = -0.1\omega_P$ is close to zero for light incident from the left, while it is non zero for light incident from the right. Thus, this structure could also be used for magneto-optical isolation [85].

Chapter 4
The role of Rabi splitting tuning in the dynamics of strongly coupled J-aggregates and surface plasmon polaritons in nanohole arrays

4.1 Introduction

Matter–light interaction is surely one of the most fundamental processes occurring in nature, and the interaction between molecular excitons and surface plasmon polariton (SPP) modes is one of its most effective forms. When the interaction is weak, the wave function of molecules and the SPP modes can be treated as unperturbed, only leading to modification of the spontaneous emission rate. On the other hand, when the interaction is strong enough, upon light irradiation a reversible energy is exchanged between the excitons and SPP modes at a rate faster than their respective damping processes. The result is the formation of a hybrid [86, 87] exciton–SPP state: the system is in a strong coupling regime [88, 89, 90, 91, 92, 93, 94]. The new state is formed by two energy bands (upper and lower band) separated by an energy value known as the Rabi splitting energy $\hbar\Omega_R$ ($\hbar\Omega_R$, the energy exchange rate between the hybrid bands). The hybrid state is characterized by the mixed properties of molecules and SPPs, which is similar to the behaviour of polaritons in an optical microcavity [95, 96, 97, 98, 99, 100, 101]. Such an intrinsic peculiarity makes hybrid states interesting for both fundamental research and applications. It has been demonstrated that the strong coupling with organic molecules can display a very large vacuum Rabi splitting (up to 700 meV with SPPs; more than 1 eV in a cavity), comparable to a significant fraction of the molecular transition energy [98, 102, 103]. The strong modification of the energy levels of the hybrid system has been used to tune chemical reaction rates [104] and the work function of organic materials [105]. In particular, due to the bosonic character of the hybrid states, non-equilibrium Bose–Einstein condensation has been observed at room temperature [106].

From a dynamics perspective, the Rabi oscillations between J-aggregate molecules and SPPs have been recently measured in real time on a 10 fs timescale [107], the first step towards the realization of next stage nano-plasmonic devices, such as all-optical switches and low threshold nanolasers [96, 108, 109]. The choice of this kind of molecule is dictated by the need for realizing strong coupling. Indeed, according to the definition, strong coupling is achieved if the Rabi splitting is wider than the linewidths of both the SPP mode and the molecule absorption resonance. In this regard, J-aggregates show a narrow absorption band, much narrower than standard dye molecules (such as Rhodamine 6G, Sulforhodamine 101, Rhodamine 800, Nile red and beta-carotene) which instead are characterized by inhomogeneously broad spectra. In the absence of dissipation, the Rabi splitting energy $\hbar\Omega_R$ (i.e. the coupling strength) of an individual two-level oscillator at resonance with the SPP vacuum field $\mathbf{E}$, is given by [110]:

$$\hbar\Omega_R = 2\mathbf{E}\cdot\mathbf{d}\sqrt{n_{ph}+1} = 2\sqrt{\frac{\hbar\omega}{2\varepsilon_0 V}}d\sqrt{n_{ph}+1}, \tag{4.1}$$

where $\mathbf{d}$ is the molecular transition dipole moment of the two level oscillator, $\hbar\omega$ is the SPP resonance energy, ε_0 is the vacuum permittivity, V is the modal volume and $\mathrm{n_{ph}}$ refers to the number of photons in the system. Importantly, energy splitting can still exist even under zero photon conditions, that is $\mathrm{n_{ph}} = 0$. This is indeed known as vacuum Rabi splitting ($\hbar\Omega_{VRS}$), attributed to electromagnetic vacuum fluctuations. In particular, quantum theory predicts that $\hbar\Omega_{VRS}$ is proportional to the square root of the absorbance which, in turn, is proportional to the concentration $\sqrt{N/V}$ [89, 93], where N is the number of oscillators in the modal volume V. Hence, increasing the molecule concentration, namely confining the molecules into a smaller volume, is an effective way to increase the coupling strength.

In recent years there has been a great deal of effort towards understanding the dynamics of strongly coupled systems by transient spectroscopy experiments [107, 111, 112, 113, 114, 115]. It has been demonstrated that the lifetime of the upper hybrid band in exciton–SPP systems can be much longer than the life of bare excited molecules. It was suggested that this result can be caused by a trap state observed in the upper band [111, 113] or by the blockage of the vibrational relaxation modes due to the large Rabi splitting [116, 117, 118, 119]. In this work, we report a comprehensive spectroscopic study of a prototypical SPP–molecule hybrid structure consisting of a gold nanoholes array coated with different constructions of J-aggregate molecules [120]. The dynamics of the aforementioned system is revealed by an ultrafast pump–probe approach under resonant excitation. We demonstrate that the upper hybrid band shows a reduced lifetime upon increasing of the coupling strength.

4.2 Sample Fabrication

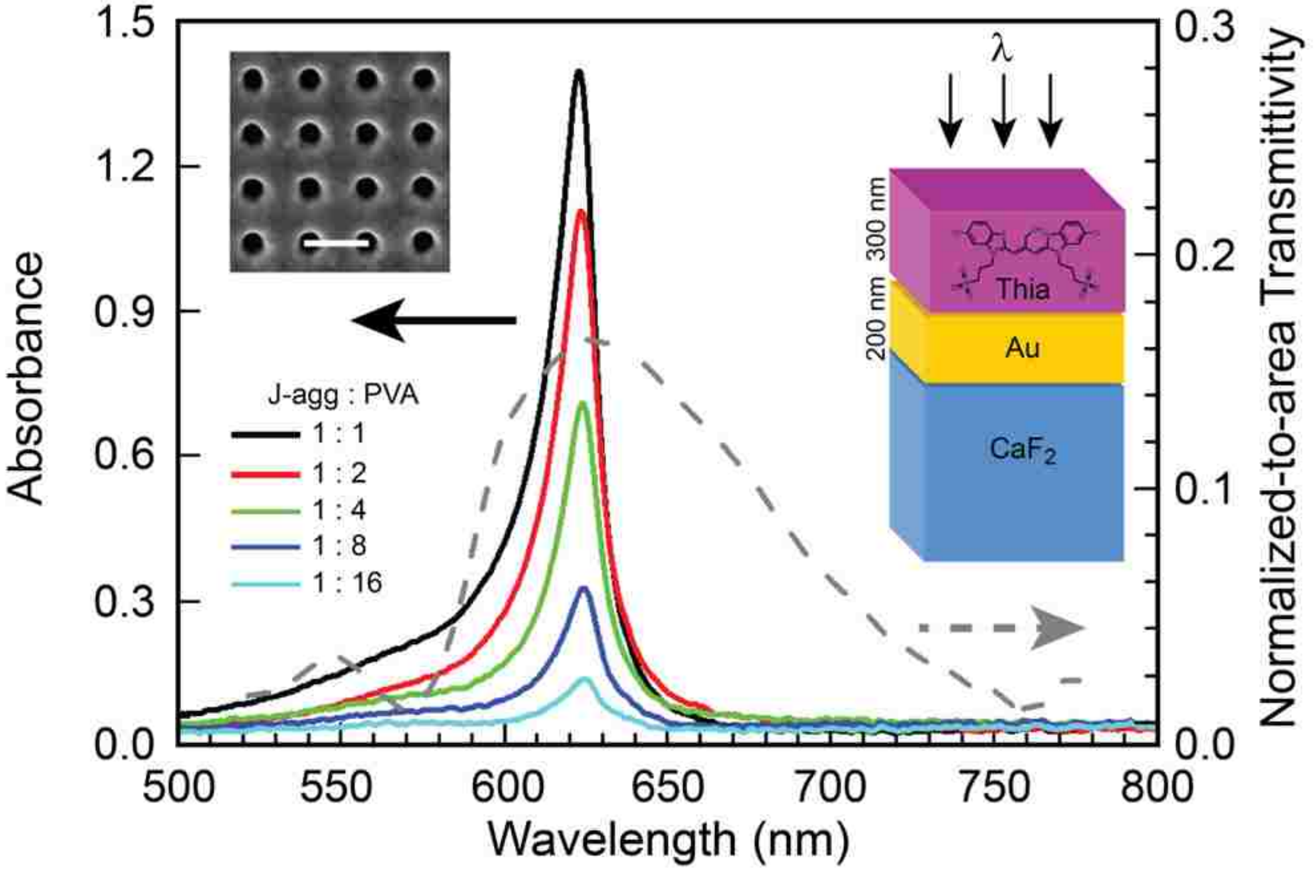

Figure 4.1: Experimental absorbance spectra, at different concentrations of J-aggregate molecules, dispersed inside a 300 nm thick PVA film (solid lines). Normalized-to-area transmission spectrum of a gold hole array (period = 310 nm, white bar in the SEM image) covered with a 300 nm thick PVA film showing the broad SPP feature (gray dashed line). The low and high wavelength peaks correspond to the SPP orders (1,1) and (1,0), respectively. Inset: SEM image of the nano-patterned gold layer. Light is impinging from the top with normal incidence.

The samples were fabricated through the deposition of 200 nm of gold on a CaF_2 substrate followed by the milling of the holes array by focused ion beams (FEI/Helios Nanolab 650). The total patterned area is $200 \times 200\ \mu m^2$. The ratio between the periodicity and the hole diameter was kept at 2.5 while the period was varied from 260 to 360 nm. Afterwards, the samples were coated with a 300 nm thick layer of J-aggregate molecules, previously dispersed in liquid PVA (polyvinyl alcohol) with five different concentrations (from 0.5 to 4 mg/mL). To determine the absorbance of the J-aggregate film, samples with no gold layer were fabricated; the corresponding absorbance spectra are shown in Fig. 4.1 together with the scheme of the overall structure. The dye used in the experiments was 3,3' -disulfopropy1 -5,5' -dichloro-9-ethylthia-carbocyanine triethylammonium salt (Thia; Hayashibara Biochemical Laboratories, Inc.), which has a sharp absorbance at 623 nm due to its large transition dipole moment upon J-aggregation. Such a feature is particularly suitable to achieve strong coupling with SPPs. In order to prevent oxidization, the samples were sealed by a glass slide under a nitrogen environment in a glove box with an oxygen concentration lower than 0.1 ppm.

4.3 Numerical Simulations

The numerical simulations were based on the Rigorous Coupled Wave Analysis (RCWA) method [121]. This numerical approach uses the concept of a unit cell to handle both 2D and 3D periodic structures and is specifically tailored for multilayer structures. The unit cell definition can have arbitrary geometry and the index distribution can consist of both standard dielectric materials and dispersive/lossy materials such as metals. The electromagnetic input can be an incident plane wave with arbitrary direction and polarization. Various simulation results can be outputted including far field components such as absorption, reflection and transmission. In particular, the latter quantity was utilized for a straight comparison with the experimental data.

The gold permittivity was described following the model in Alabastri *et al.* [122], while PVA and CaF_2 permittivities were taken equal to 2.25 and 2.045, respectively, for all the wavelength spectrum of interest. The J-aggregate permittivity is described by a Lorentz oscillator model with the main resonant energy at 1.99 eV, as reported by Wurtz *et al.* [123]. In order to match the short-wavelength tail of the experimental absorption spectra (see Fig. 4.1), we slightly modified this simple model by adding a second oscillator at 2.16 eV.

Finally, the impinging light was considered normal to the top surface with linear polarization directed along the shortest distance between two adjacent holes.

4.4 Static Measurements

Periodic metallic hole arrays have the capability to convert impinging radiation into SPPs modes resulting in a remarkable field confinement at the metal surface. Owing to the periodic pattern of the array, the desired SPP mode can be chosen by tuning the period thus to match the absorbance peak of the J-aggregates. Upon normal incidence radiation, the transmission spectrum of the gold holes array with a period of 310 nm (gray dashed line) shows two peaks corresponding to the SPP orders (1,1) and (1,0) [124, 125]. As illustrated in Fig. 4.1, the (1,0) SPP mode overlaps the absorbance peaks of the J-aggregate molecules, shown at different concentrations, with the result of maximizing the coupling strength. In Fig. 4.2(a) are plotted the simulated normal incidence transmission spectra for a series of gold hole arrays, characterized by different periodicities, covered by a 300 nm thick J-aggregate/PVA film (the latter manifesting an absorbance of 1.40 at 623 nm, as shown in Fig. 4.1). Similarly, in Fig. 4.2(b) are illustrated the corresponding experiment. As can be observed, the original plasmon peak illustrated in Fig. 4.1 (gray dashed line) splits into two bands. In particular, in Fig. 4.3(a) and Fig. 4.3(b) (numerical simulations and experimental characterization, respectively) the dispersion of the two bands is plotted as functions of both the holes array period from 260 nm to 360 nm and absorbance, and the result shows the characteristic feature of strong coupling: the anticrossing of energies. An optimal Rabi splitting of 245 meV was experimentally measured at the resonance period of 310 nm for a concentration corresponding to an absorbance equal to 1.40. The dispersion curves for lower concentrations of J-aggregates are also represented in the figures. The decrease of the energy splitting magnitude upon lowering the

J-aggregate concentration is clearly shown. In particular, J-aggregate/PVA film absorbances of 0.70 and 0.14 correspond to Rabi splitting of 161 meV and 99 meV, respectively.

In Figs. 4.4(a), 4.4(b), the former corresponding to simulations the latter to experiments, is highlighted the behaviour of Rabi splitting as a function of the absorbance for the resonant period of 310 nm and under normal incident radiation. A remarkable match is noticed between the two figures. The observed Rabi splitting displays a linear dependence on the square root of the J-aggregate absorbance [Fig. 4.5(a) simulations, Fig. 4.5(b) experiment] which, in turn, depends on the molecule concentration. Thus, the Rabi splitting observed in the normal transmission spectrum follows a $\sqrt{N/V}$ dependence, which is consistent with previous experimental results and the quantum theory description of strong coupling [93, 104]. Above all, static measurements have clearly indicated that the hybrid system is in a strong coupling regime. To gain further insight into the corresponding dynamics of such a hybrid system with different coupling strengths, extensive studies were focused on transient absorption spectroscopy.

4.5 Transient Absorption Experiments

Femto-second transient absorption (TA) spectroscopy was carried out with a 100 fs laser pump–probe setup [126, 127, 128] based on a mode-locked Ti:sapphire laser/amplifier system (Solstice, Spectra-Physics). The amplified output from the regenerative amplifier (RGA, Spitfire, Spectra Physics), showing a 250 Hz repetition rate with a pulse energy of 1.5 mJ, 100 fs pulse width and 800 nm wavelength, was split into two parts. The strongest signal was used to generate the desired excitation pulse at 560 nm through a TOPAS system; the weakest part was focused on a sapphire substrate to generate a broadband white light, from 450–800 nm, used as probe pulses. The two beams were orthogonally and collinearly recombined by a dichroic mirror, and focused on the sample at normal incidence through a microscope objective (NA 0.75, magnification 10). Of particular note is that, due to the chromatic aberrations, the focal planes of the pump and probe beams are indeed different. In this regard we had to apply a procedure to optimize the

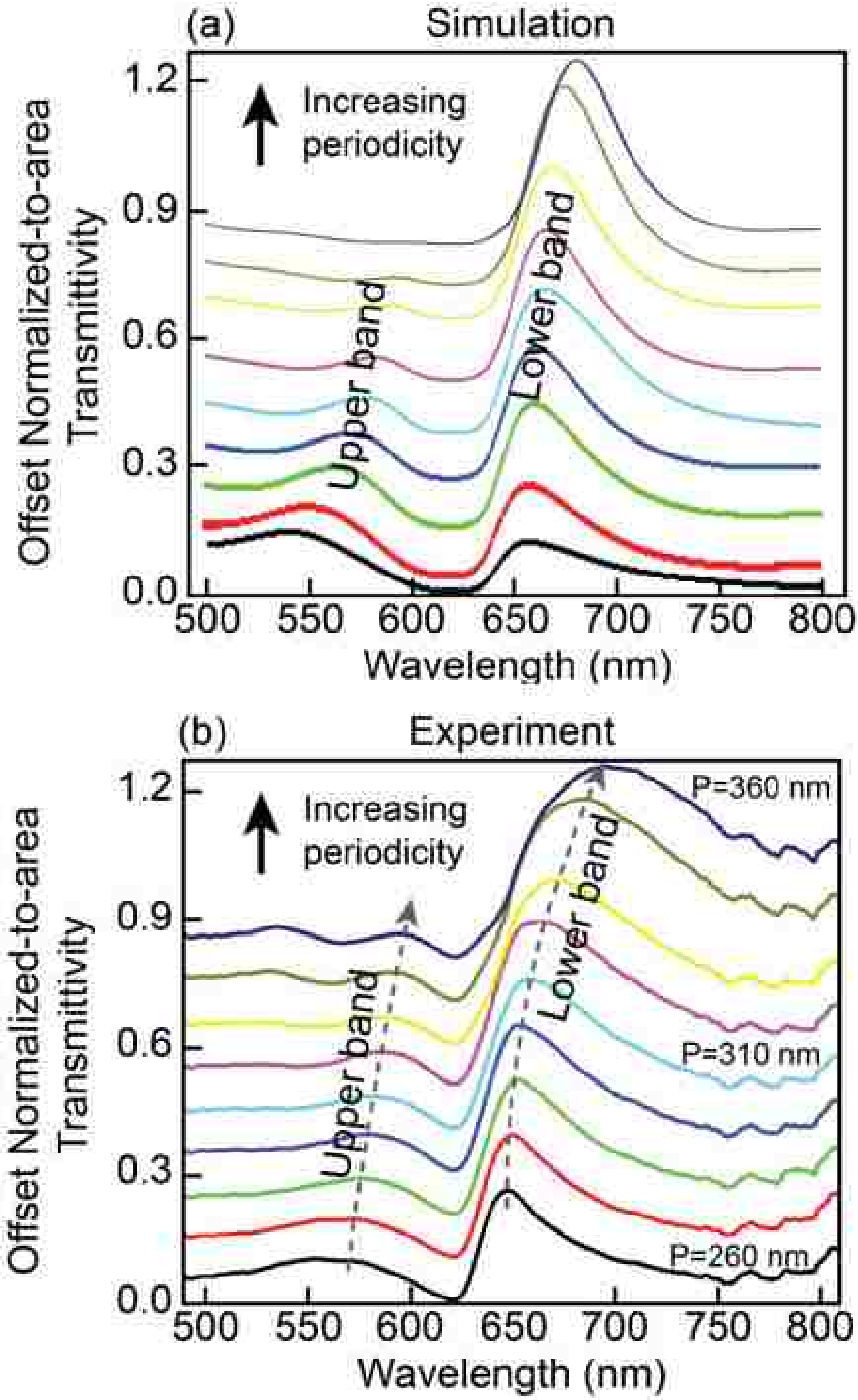

Figure 4.2: (a) Simulated transmission spectra of a set of gold hole arrays (period from 250 nm to 350 nm as indicated by the arrow) covered by a 300 nm-thick PVA film doped with J-aggregates (chosen concentration such as the absorbance is 1.40 at 623 nm – see Fig. 4.1 black curve). (b) Experimental normalized-to-area transmission spectra of a set of gold hole arrays (period from 260 nm to 360 nm as indicated by the arrow) covered by a 300 nm-thick PVA film doped with J-aggregates (chosen concentration such as the absorbance is 1.40 at 623 nm – see Fig. 4.1 black curve). The two dashed lines highlight the shift of the lower and upper bands.

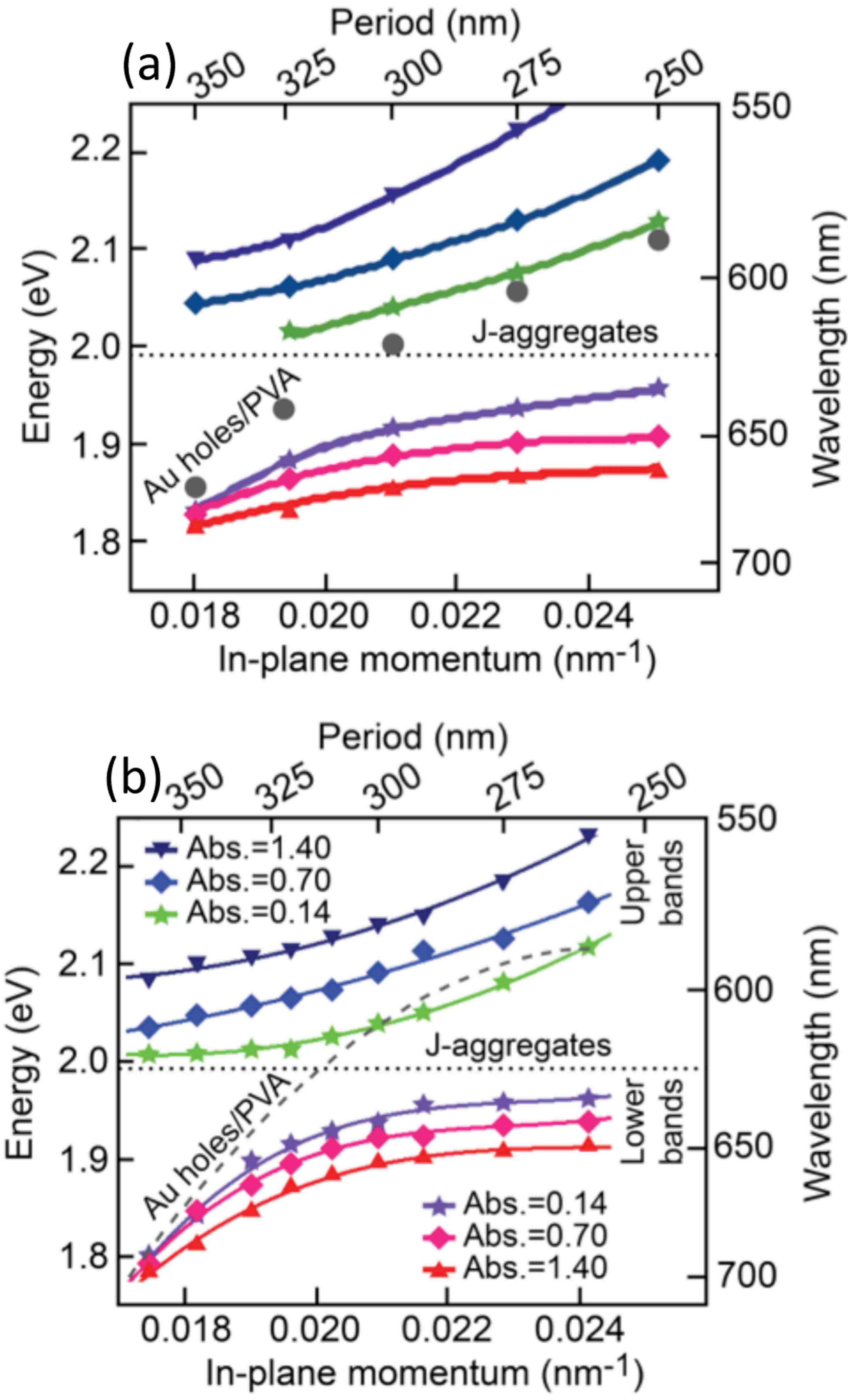

Figure 4.3: (a) Simulated energy dispersion curves associated with three J-aggregate doped samples at different concentrations: 1.40 (blue and red triangles), 0.70 (light blue and pink squares) and 0.14 (green and violet stars). The gray dots represent the simulated dispersion curve for the J-aggregate-free (undoped) configuration. (b) Experimental energy dispersion curves corresponding to the undoped sample (no J-aggregate molecules, only gold holes array and PVA; gray dashed line) and to three different samples, doped with J-aggregates, showing absorbance of 1.40 (blue and red triangles), 0.70 (light blue and pink squares), and 0.14 (green and violet stars) calculated at 623 nm. These three values of absorbance were obtained by tuning the period of the holes array from 260 nm to 360 nm. The horizontal black dotted line corresponds to the J-aggregate 623 nm absorbance energy.

focusing of the probe beam. Otherwise, the pump would be out of focus thus providing a spatially uniform excitation pulse larger than the probed area. Finally, the reflected light from the sample was collected by the same objective and, by blocking the excitation light through a filter, the transient absorption data were collected by using a fibre-coupled sensitive spectrometer (Avantes AvaSpec-2048 × 14). The detection window was from 575 nm to 800 nm due to the blockage of the probe light by the dichroic mirror. To be noted is that the group velocity dispersion of the transient spectra was compensated by a chirp program.

In TA experiments we measured the variation of the optical density ΔOD, here defined as -log($R_{\text{pump,probe}}/R_{\text{probe}}$), where $R_{\text{pump,probe}}$ is the reflection of the probe laser right after the pump signal has hit the sample, namely the sample reflection upon perturbation induced by the pump laser. Similarly, the R_{probe} describes the probe reflectivity under conditions far from the pump excitation. The three highest J-aggregate concentration samples, with absorbance values of 1.40, 1.10 and 0.70 calculated at 623 nm, were chosen for TA measurements. In Fig. 4.6(a) is shown the response of the reference sample, formed by J-aggregate/PVA spin-coated on a flat gold film, irradiated with a 560 nm laser pulse (upper band excitation). The result is a positive signal around 610 nm, which is attributed to excited state absorption, while the narrow negative signal at 623 nm, which is consistent with the steady-state absorption spectrum of Fig. 4.1, corresponds to the ground state bleaching of J-aggregates. As can be seen in Fig. 4.6(b), the normalized bleaching kinetics associated with the three aforementioned absorbance values show very similar behaviour, namely fast decay, with no apparent dependence on the J-aggregate concentration.

The next step was to perform TA experiments on hybrid systems formed by gold hole arrays (period = 310 nm) covered by a film of PVA and J-aggregates at different concentrations (thickness of the film around 300 nm). Similarly to the experiment shown in Fig. 4.6, the samples were pumped by a pulsed laser at 560 nm corresponding to the upper hybrid band excitation. However, with respect to the reference sample of Fig. 4.6, the transient absorption spectra of the hybrid system show totally different features. Indeed, in Figs. 4.7, 4.8, and 4.9, all three transient spectra

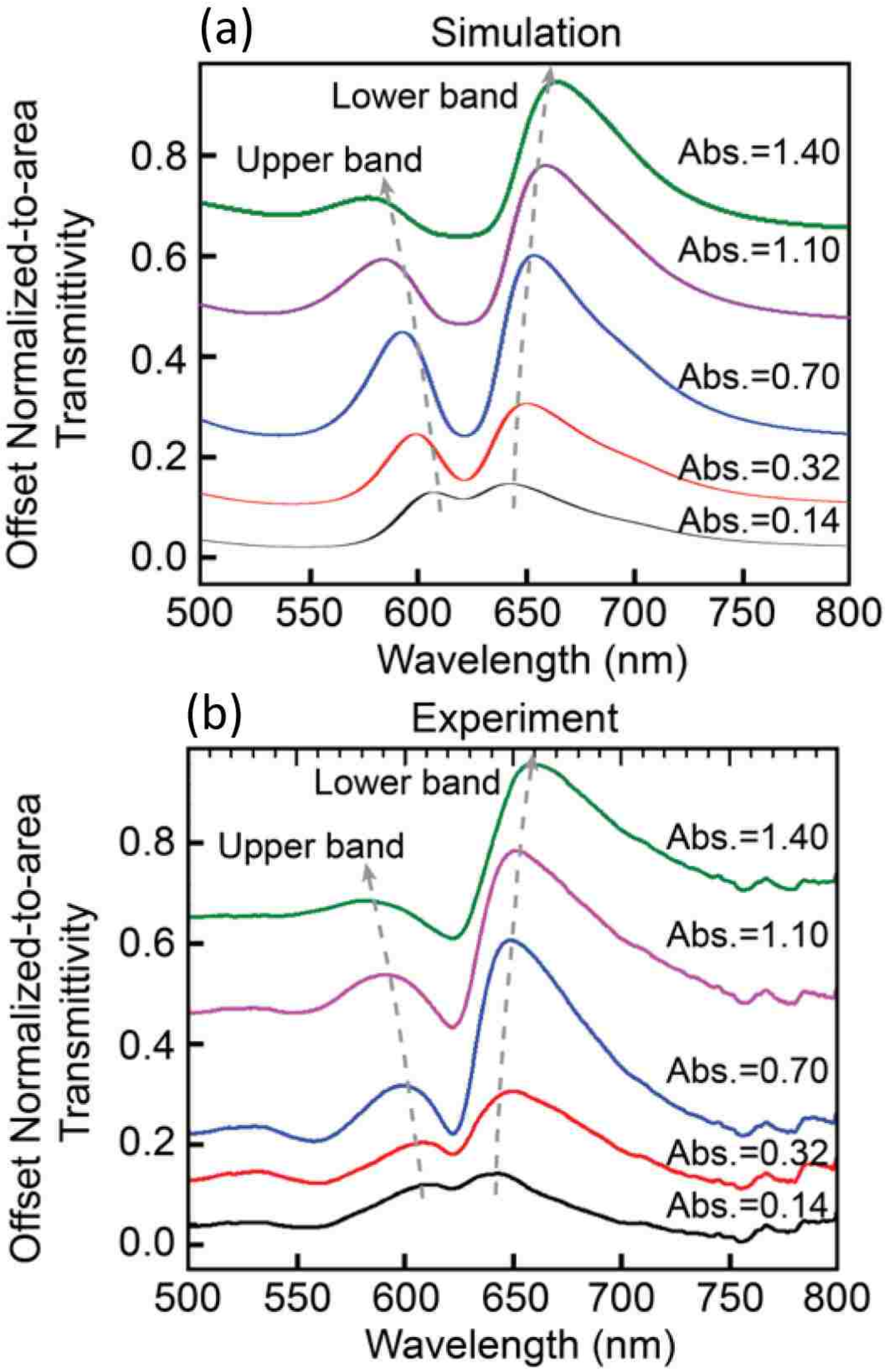

Figure 4.4: (a) Simulated transmission spectra of gold holes array (period = 310 nm) upon increasing of the J-aggregate concentration (absorbance from 0.14 to 1.40 calculated at 623 nm). (b) Experimental characterization as in (a).

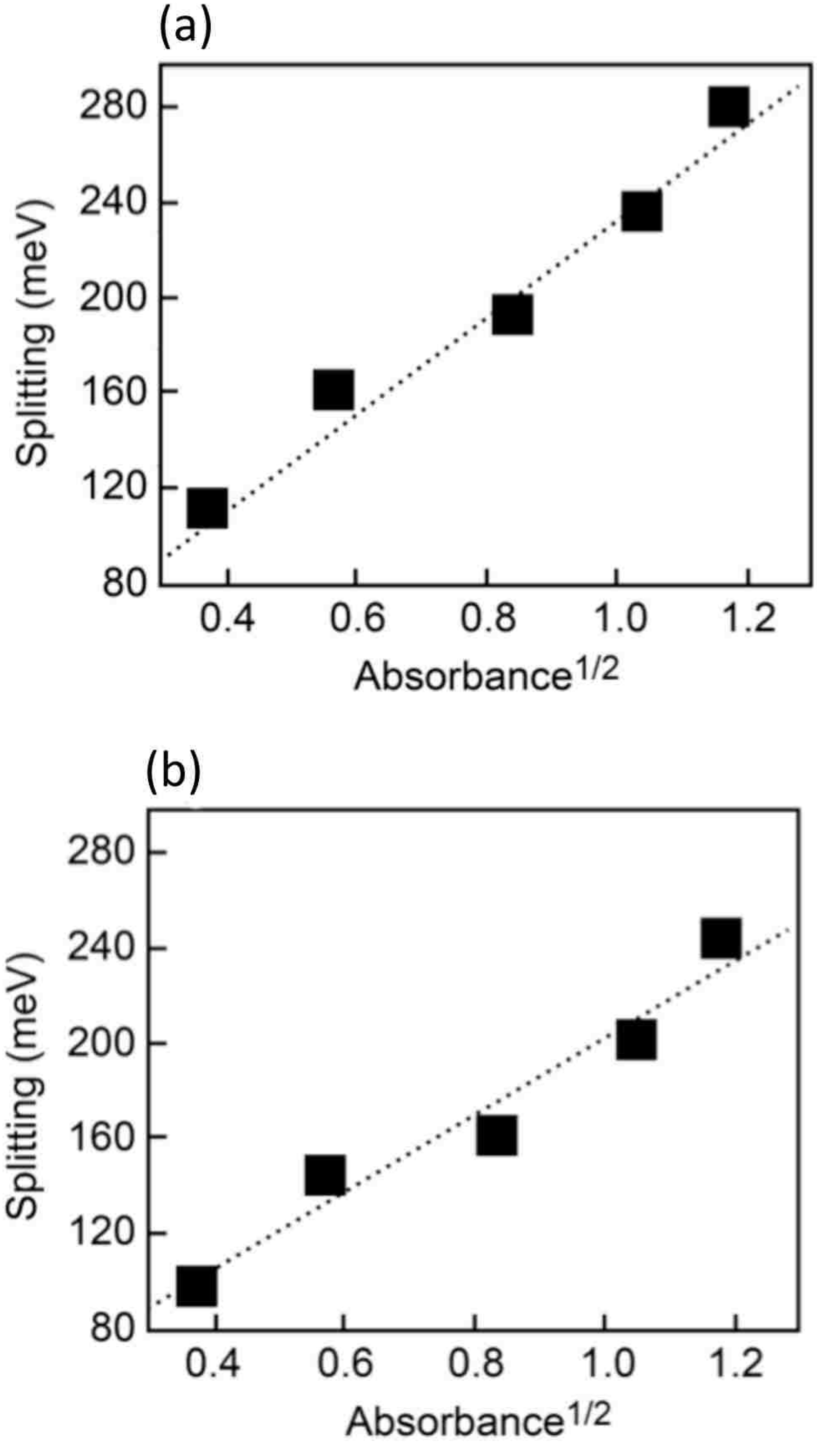

Figure 4.5: (a) Simulated Rabi splitting values as a function of the square root of the J-aggregate molecule absorbance. The chosen period is 310 nm. (b) Corresponding experimental Rabi splitting.

are characterized by two bleaching signals (to be noted that due to the limitation of the detection window only a small part of the upper bands can be clearly detected). Especially for the highest J-aggregate concentration sample (absorbance 1.40), the upper band undergoes a strong blue-shift pushing it almost out of the detection window due to the very large Rabi splitting. Regardless, clear evidence of the existence of lower and upper bands is provided by all the considered concentrations.

For J-aggregate concentrations with absorbance values of 1.10 and 1.40 (Figs. 4.7, 4.8), a positive signal associated with thermal effects [129] is observed between the two bleaching minima. Indeed, in the proposed configuration the resonant pump laser brings the system to an excited condition where the energy is shared and oscillates between the SPP modes associated with the gold nanoholes array and the excited state of J-aggregates. This leads to the hybrid states appearing in the TA spectra once the probe laser shines into the system. In the first moments, after the pump laser hits the sample (<1 ps), the system undergoes dephasing of the SPP resonances, namely the excited electrons tend to thermalize via electron–electron scattering. This phenomenon determines the creation of new energy levels which will contribute to the absorption of probe photons, namely the transmission of the probe pulse is reduced with respect to the initial completely coherent (before dephasing) coupled hybrid system. In turn, this means a positive peak in the TA measurements.

However, by considering the amplitude of the thermal peak with respect to the overall spectra, we can argue that at these concentrations the hybrid system is probably dominated by a SPP-related non-thermal process. With the J-aggregate concentration decrease, the lower and upper bands gradually overlap with each other due to the Rabi splitting decrease (Fig. 4.9); meanwhile the small positive signal submerges in the bleaching signals. Hence, for all the three samples under resonant 560 nm excitation, the dynamics of the hybrid systems is dominated by a SPP-related non-thermal process, in which the photophysics nature of strong coupling can be directly reflected.

In order to highlight the shift associated with different J-aggregate concentrations, the spectra recorded at 0.5 ps are shown in Fig. 4.10 for all three concentrations. The observed shift of the lower band (the upper band falls outside the detection window) confirms that the Rabi splitting

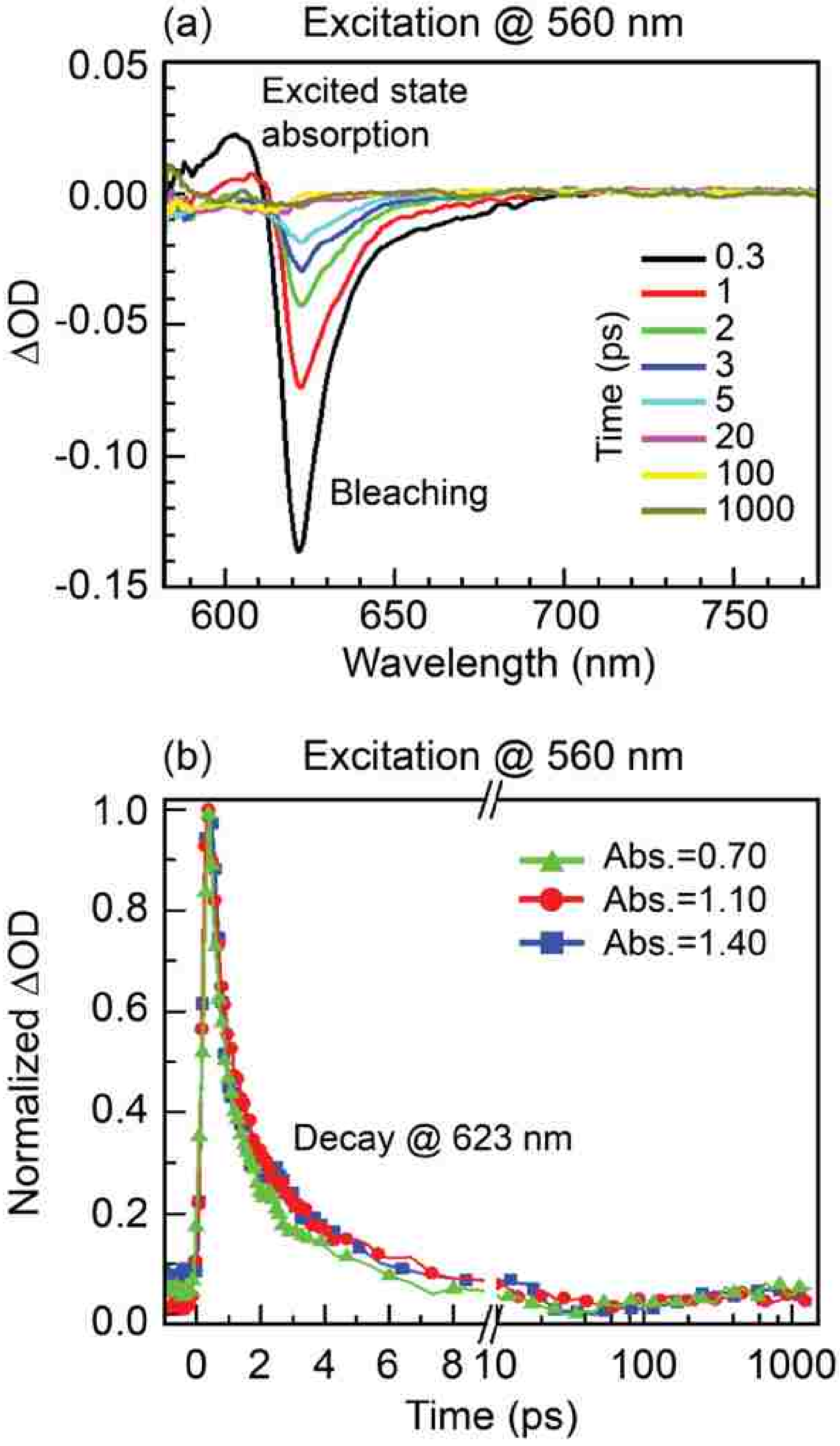

Figure 4.6: (a) Transient absorption spectra of J-aggregates (absorbance of 1.10 at 623 nm) on a flat gold film. The spectra were recorded at 0.3, 1, 2, 3, 5, 20, 100 and 1000 ps. (b) Normalized bleaching dynamics of J-aggregates on a flat gold film at 623 nm with different concentrations (measured from reference samples with no gold layer). For both figures, a 560 nm excitation was considered (upper band excitation). ΔOD: optical density variation.

increases with the J-aggregate concentration. This result is consistent with the static measurements shown in Fig. 4.5(a).

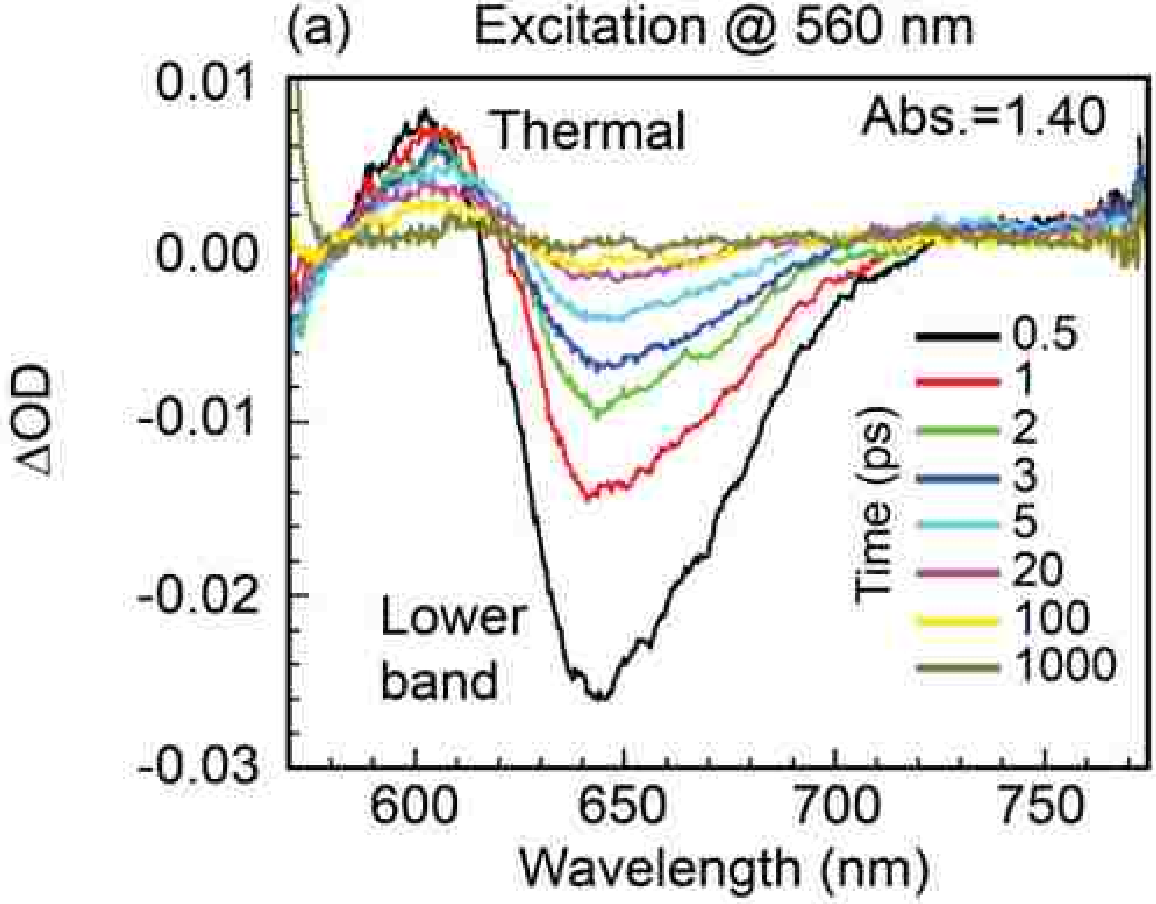

Figure 4.7: Transient absorption spectra of PVA/J-aggregates with different concentrations for absorbance of 1.40, deposited on a gold holes array under 560 nm excitation. The period of the array is taken to be equal to 310 nm. The PVA thickness is around 300 nm. The spectra were recorded at 0.5, 1, 2, 3, 5, 20, 100 and 1000 ps. ΔOD: optical density variation.

The kinetics of the lower [Fig. 4.11(a)] and upper [Fig. 4.11(b)] hybrid bands with different coupling strengths (i.e. J-aggregate concentration) are compared with the kinetics of J-aggregates on a flat gold film and a flat glass substrate. The choice of materials is dictated by the need for ruling out any kind of strong coupling which might also occur between J-aggregates and a flat gold film. In particular, due to the detection window limitations, the upper band of the highest J-aggregate concentration sample (absorbance 1.40) cannot be detected. For the other two

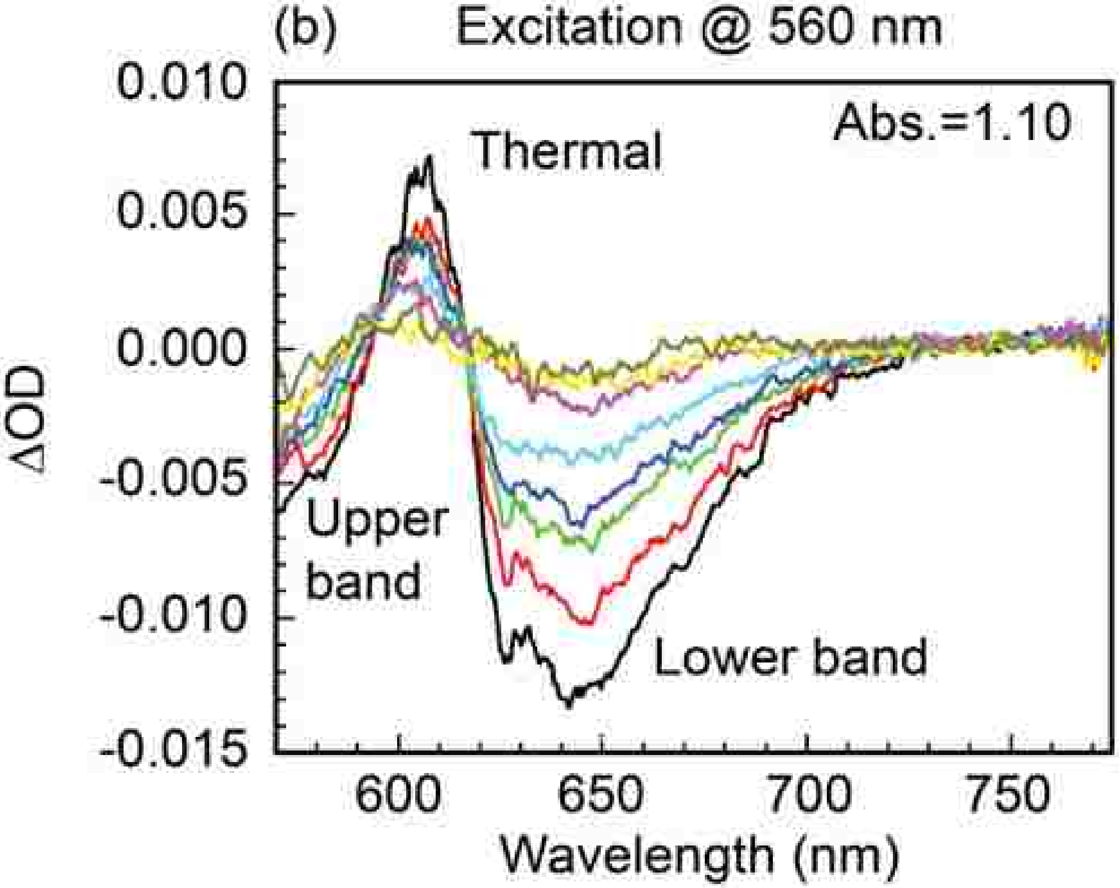

Figure 4.8: Transient absorption spectra of PVA/J-aggregates with different concentrations for absorbance of 1.1, deposited on a gold holes array under 560 nm excitation. The period of the array is taken to be equal to 310 nm. The PVA thickness is around 300 nm. The spectra were recorded at 0.5, 1, 2, 3, 5, 20, 100 and 1000 ps. ΔOD: optical density variation.

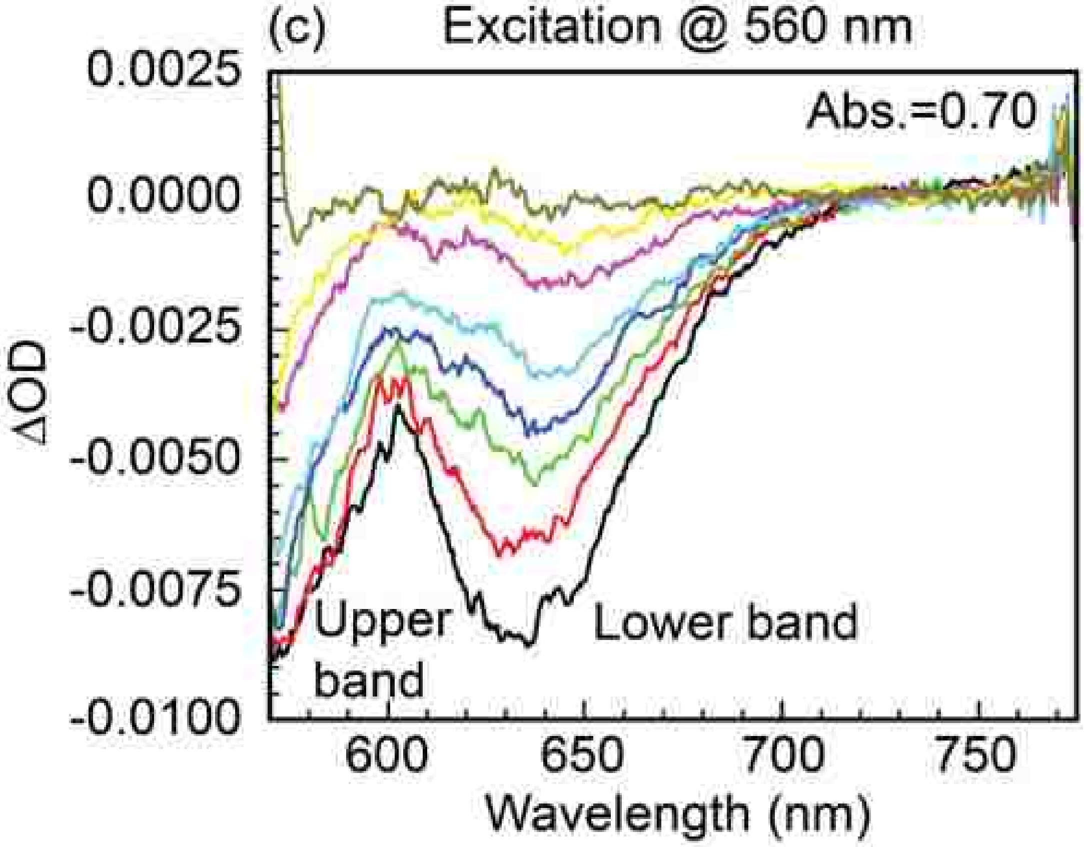

Figure 4.9: Transient absorption spectra of PVA/J-aggregates with different concentrations for absorbance of 0.7, deposited on a gold holes array under 560 nm excitation. The period of the array is taken to be equal to 310 nm. The PVA thickness is around 300 nm. The spectra were recorded at 0.5, 1, 2, 3, 5, 20, 100 and 1000 ps. ΔOD: optical density variation.

samples (absorbance 0.70 and 1.10) the kinetics of the upper bands are taken at the detection window edge, namely 580 nm. The results clearly show that the hybrid bands have longer lifetimes than the bleaching recovery of J-aggregates on flat gold films and glass substrates. Furthermore, Fig. 4.11 also shows that the kinetics of the hybrid exciton–SPP state is significantly affected by the J-aggregate concentration, namely the coupling strength. Indeed, the lifetime of both hybrid bands is reduced by increasing the coupling strength (higher J-aggregate concentration). This result is of particular interest especially when compared to the behaviour of J-aggregates on a flat gold film where no dependence on the concentration was detected, as shown in Fig. 4.6(b) (similar considerations also apply to J-aggregates on the glass substrate, see Fig. 4.11). This behaviour can be explained by taking into account the phonon bottleneck effect, the phenomenon responsible for suppressing vibrational relaxation levels, as already demonstrated in semiconductor quantum dots [130] and also demonstrated in strongly coupled hybrid systems as a result of the large Rabi splitting [118]. Indeed, under pump laser excitation the population density of plexitons (i.e. combination of plasmons and excitons) in hybrid bands increases with the concentration of J-aggregates (the amplitude of the bleaching signal is proportional to the J-aggregate concentration). With high population density, the interaction among plexitons is expected to be especially significant, which in turn means that energy is released to build up the population of phonons associated with different energies. These new energy levels will then represent a channel for a relaxation from the upper to the lower hybrid band and further to the ground state (namely removal of the bottleneck effect). Such behaviour is consistent with the bottleneck suppression found at high pump powers [131], in which a higher population density can be created. Thus we suggest that the bottleneck relaxation mechanism can also play an important role in the dynamics of SPP-related systems and is strongly suppressed in hybrid structures with large Rabi splitting values (i.e. high dye concentration). This explains why the lifetime under high dye concentration approaches (i.e. shorten) the behaviour of the dye on top of a flat metal layer or glass substrate.

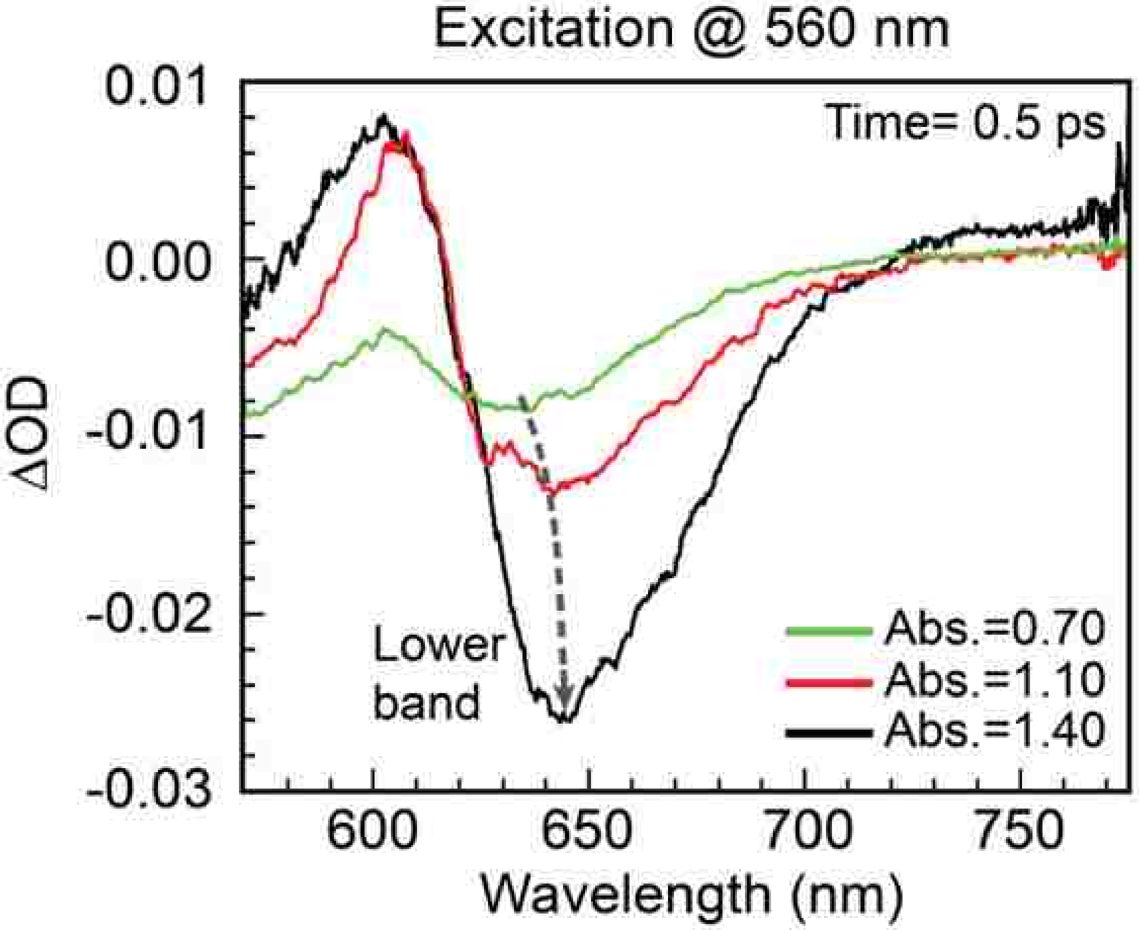

Figure 4.10: Transient absorption spectra recorded at 0.5 ps for PVA/J-aggregates deposited on a gold holes array with period equal to 310 nm. Three different concentrations are considered. The lower band red shift is highlighted by the gray dashed line. Excitation: 560 nm. ΔOD: optical density variation.

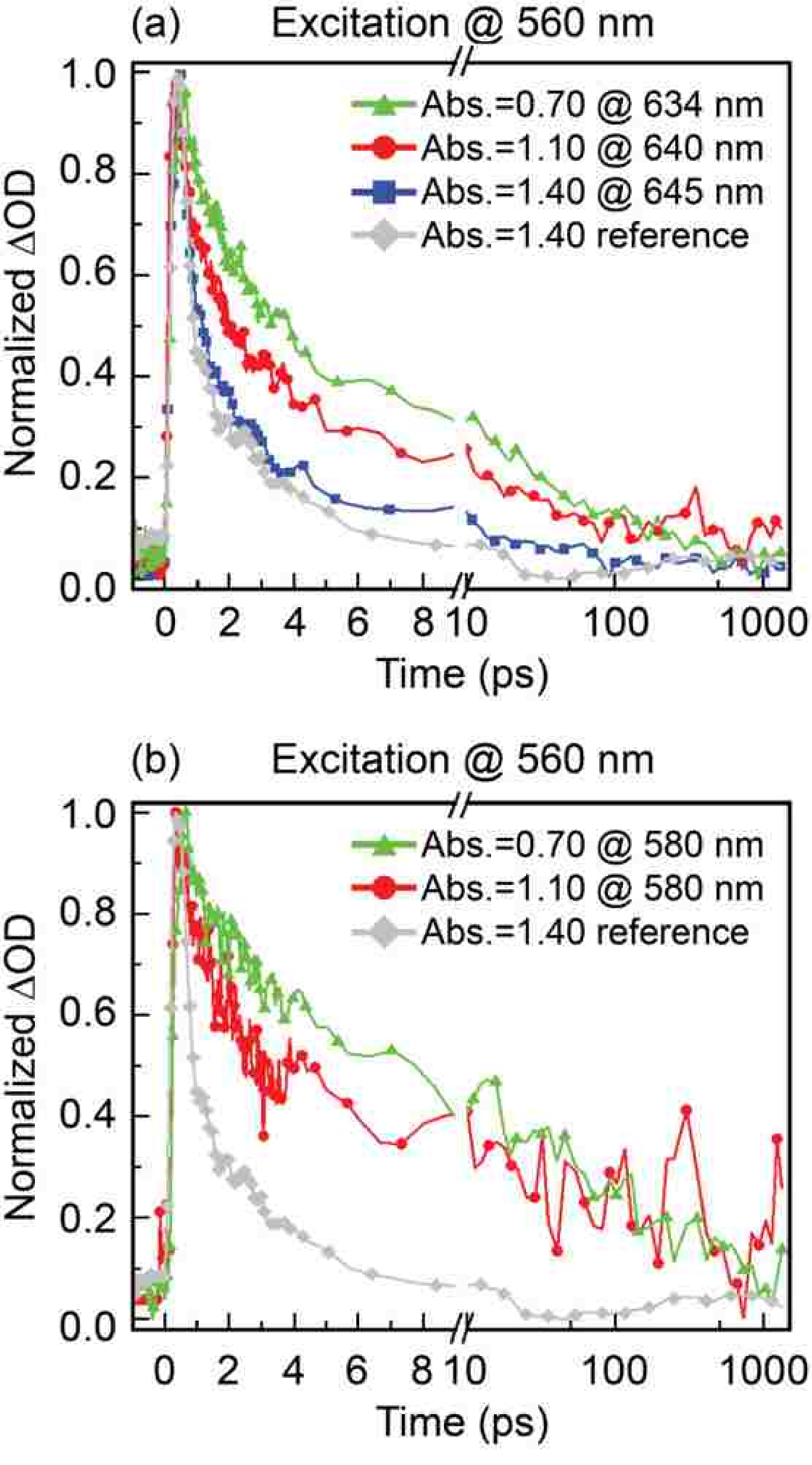

Figure 4.11: Comparison between normalized bleaching dynamics of PVA/J-aggregates with different concentrations on gold hole arrays. (a) Lower hybrid bands, (b) upper hybrid bands measured at the detection window edge (580 nm). The normalized bleaching dynamics of PVA/J-aggregates (absorbance 1.40) on a flat gold film at 623 nm is shown as reference (gray dot line). Similarly, the figures also show the normalized bleaching dynamics of PVA/J-aggregates on a glass substrate with different concentrations (color dot lines). The excitation source is equal to 560 nm. ΔOD: optical density variation.

Chapter 5
Enhanced resolution imaging by portable microspheres

5.1 Introduction

In the quest for a fundamental understanding of the building blocks of nature, several optical characterization approaches have been developed capable of resolving deep sub-wavelength structures. A notorious strategy capable of breaking the optical diffraction limit is the use of photo-switchable molecules in far field fluorescence microscopy [132]. By either employing a point scanning system (RESOLFT), or using a stochastic wide field approach (PALM or STORM), resolutions down to 40 nm can be obtained. These methods, though, strongly depend on the photophysics of the fluorescent dyes or proteins used for labeling, mainly limiting them to biological applications [133]. Alternatively, near-field effects can produce deep sub-wavelength resolutions by collecting evanescent waves. A well-known approach consists of using probes placed in close proximity to the sample, such as in near-field scanning optical microscopy (NSOM) [134]. Despite reported resolutions of 12 nm, the distance between probe and sample is extremely critical and difficult to control in practice, and it generally suffers from poor signal to noise ratio (SNR). Other super-resolution methods capable of projecting evanescent waves into the far field include superlenses [135], solid immersion lenses (SIL) [136, 137], or microspheres placed directly in contact with the object to be imaged [138]. The latter is particularly interesting due to the wide availability of microspheres with different size or refractive index, and the ease of implementation of this approach. Indeed, extensive literature on this subject has been recently published that demonstrate the potential of sphere-mediated microscopy (SMM) for different optical configurations including bright-field [139, 138] and fluorescence microscopy [140], or even confocal systems [141]. However, SMM suffers a serious drawback inherent to its simplicity: microspheres are placed on the surface of interest with no control. As a consequence, not a single microsphere may lay on top of the object to be imaged, rendering the concept unusable. A simple solution to this problem could be to increase the number of microspheres on the sample, but at high concentrations microspheres tend to aggregate and can axially overlap, deteriorating optical performance. Furthermore, even if a microsphere is found on top of a region of interest, the field of view is limited by the size of the microsphere, which is typically between 4 and 50 μm. Therefore, it would be highly beneficial to gain control over the positioning of the microspheres for enhanced resolution imaging over user-selectable areas. Previous attempts to achieve such control consisted of creating arrays of microspheres embedded in an elastomeric matrix [139, 142] or using a microsphere glued on the tip of a glass micropipette placed on an xyz stage [143]. Note that the displacement of the elastomer with respect to the surface or the fragility of glass and the potential micropipette breakage render these approaches difficult to implement in practice. As a consequence of the lack of control in the positioning of the microspheres, a complete characterization of the optical performance of SMM is still missing. Indeed, no systematic measurement of the enhancement in spatial resolution induced by the microspheres -using the standardized resolution criteria appropriate for partially coherent systems- has been performed so far [144]. Authors have also used different parameters to define resolution including the distance between the edge of two features or the distance between maximum and minimum contrast. As a result, there exists a large disparity in the data regarding attainable resolution in SMM, with claimed values ranging from 25 nm to more than 300 nm. Even if the full width at half maximum (FWHM) of the point spread function (PSF) has been measured by deconvolution methods [142, 145], some a priori knowledge was required (shape of the PSF). In fact, this has been the subject of recent controversy [146]. Therefore, a full description of the optical response of SMM has not yet been provided.

5.2 Results

Here, we present a novel method to translate the microsphere at targeted positions on a sample based on mounting a microbead on a tipless AFM cantilever. By using the piezoelectric stages of a standard AFM, the lateral positioning of the microsphere can be easily carried out. Optical inspection of the microbead-cantilever systems enables monitoring the process in situ. In addition, the measurement of deflection of the AFM cantilever could also be used to further control the distance between microsphere and sample. With such a system, we performed a detailed measurement of the spatial resolution in SMM by imaging a calibration target consisting of gratings with different periodicity. Images of the gratings with and without the microsphere allowed a full characterization of the spatial frequency response of our microscope (modulation transfer function or MTF) and the consequent quantitative determination of the enhancement in resolution induced by the microsphere. We show that, in agreement with FDTD simulations, SMM has a resolution ultimately limited by the microsphere properties, and quite independent of the particular focusing objective used. In the conditions reported herein, we were able to observe features with typical length scales below 150 nm as previously reported in literature. However, when the collected images are interpreted by using the standard resolution criteria, the maximum resolution was $\sim$260 nm for 0.5 and 0.8 NA objectives. Even though microspheres do not break the Abbe diffraction limit or produce super-resolution, they can be regarded as portable and cheap optical elements that can enhance the effective NA of a system, making them of great interest for many applications ranging from plasmonics [147] to micro or nano Raman spectroscopy [148].

SEM micrograph of a tip-less AFM cantilever with a microsphere electrostatically (Van der Waals interaction) attached to it is illustrated in Fig. 5.1. A scheme of the imaging setup and microsphere positioning system is presented in Fig. 5.2. All experiments were performed using a bright-field microscope operated in transmission mode and coupled to an AFM system provided with a XYZ piezoelectric actuator (WiTec Alpha 300 RA). The illumination source was a blue LED with a wavelength of 405 nm. We selected this particular color since it offered higher contrast and spatial resolution than white light. In order to position microspheres on targeted positions of a sample, we used a specially designed AFM cantilever in which 3.5 μm holes were drilled by means of focused ion beam (FIB) lithography (Helios FEI Dual Beam SEM-FIB). After placing the cantilever into the AFM holder of our microscope, we proceeded with the trapping and positioning

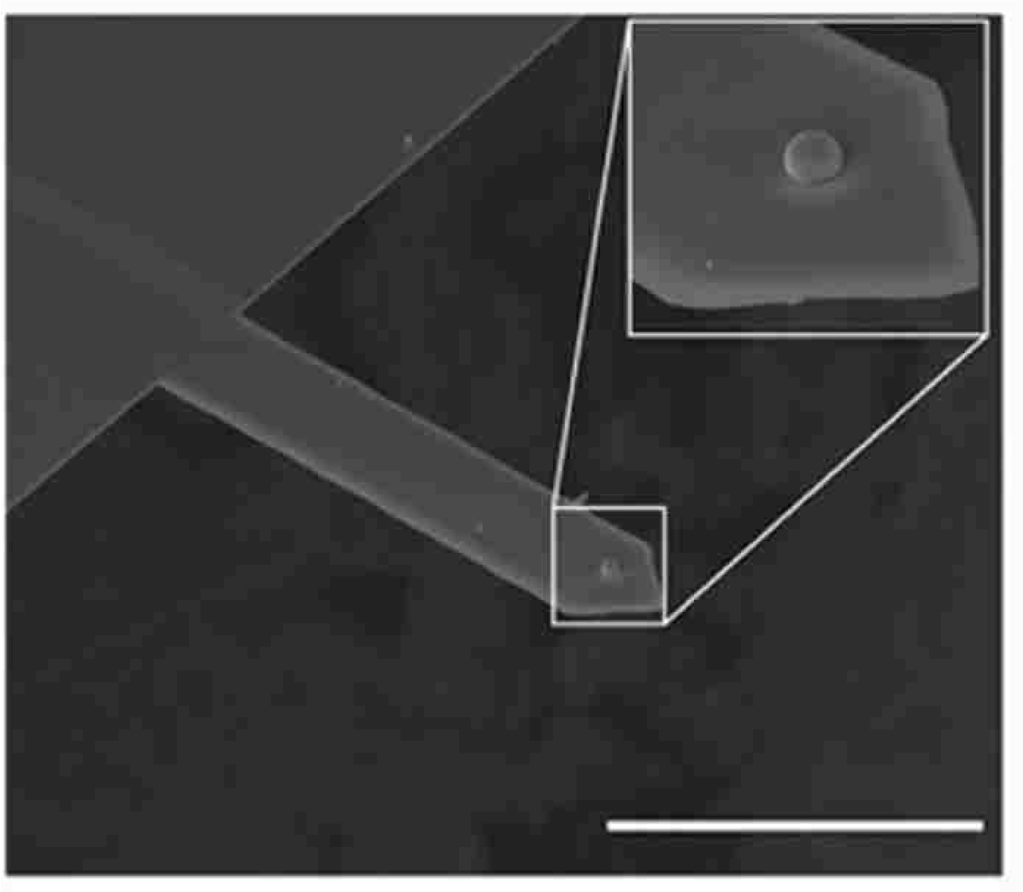

Figure 5.1: SEM micrograph of a tip-less AFM cantilever with a microsphere electrostatically (Van der Waals interaction) attached to it. Scale bar is 100 μm.

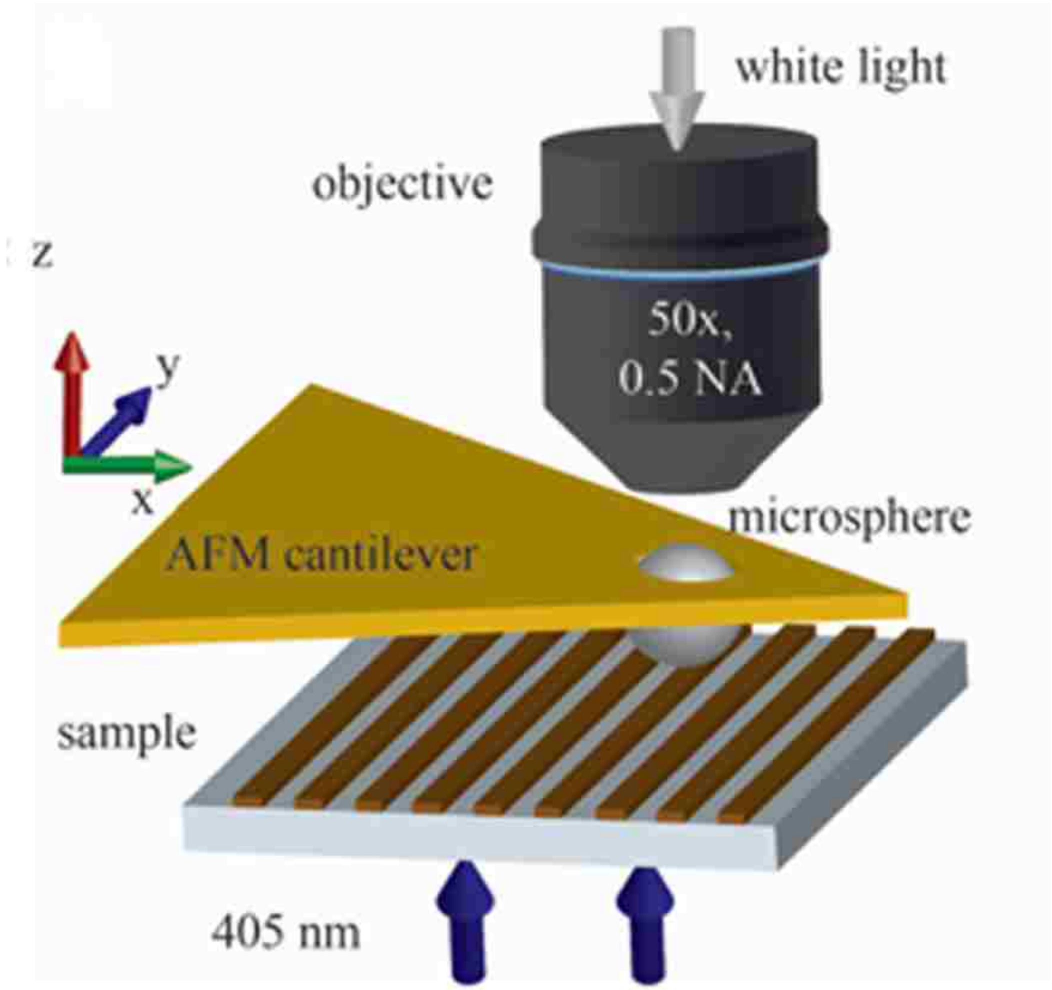

Figure 5.2: Scheme of the optical setup used for enhanced imaging with the microsphere. The system could be operated in either reflection or transmission modes. In any case, partially coherent light was used (white light or 405 nm wavelength) and the virtual image formed was collected with a microscope objective.

of individual beads. To this end, we selected a single microsphere from a reservoir of beads prepared by drop casting. We then placed the hole of the cantilever on top of the bead to be captured, and moved the cantilever axially until getting in contact with the microsphere. Electrostatic forces held the bead within the hole and allowed the displacement of the bead/cantilever system to the area of interest. Importantly, we could also detach the microsphere on a given point of interest by firmly pressing the bead against the substrate. The displacement of the cantilever was monitored in real time by means of the microscope camera (ImagingSource DFK72BUCO2). In all experiments, we used silica microspheres with a diameter of 4.7 μm (Banglabs CS019, refractive index of 1.46), as commonly used in literature [138, 149, 150]. Virtual image of a grating formed in reflection mode with SMM is presented in Fig. 5.3.

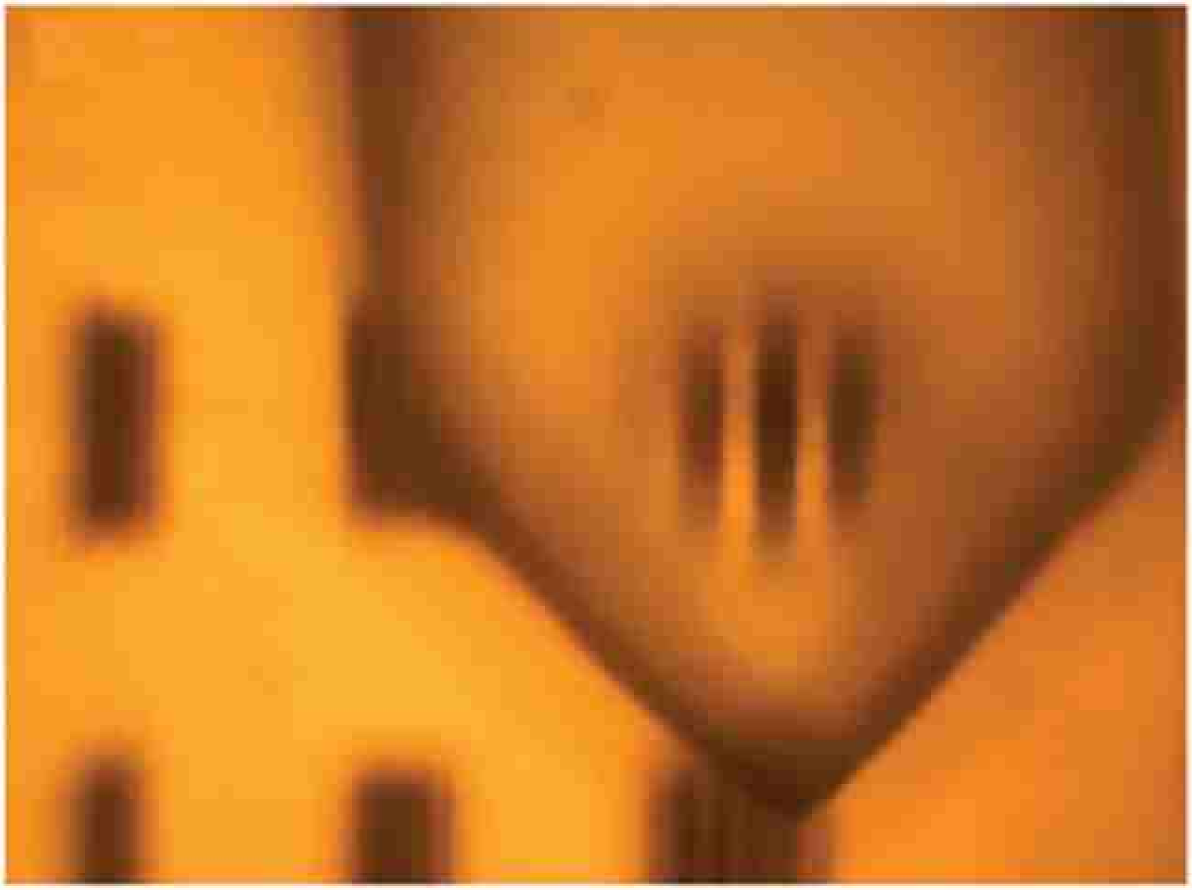

Figure 5.3: Virtual image of a grating formed in reflection mode with SMM.

We first characterized the optical performance of our system without a microsphere. In particular, we imaged a customized calibration target fabricated with FIB lithography and consisting of gold gratings on glass with periodicities ranging from 100 to 1000 nm. This calibration target can be considered as the high resolution equivalent of the 1951 USAF test chart typically used to measure resolution in partially coherent systems. Note that other test charts, such as a Siemens start, could be used for the same purpose [144]. However, given the small field of view of the microsphere, a target composed of periodic straight lines was considered more adequate. An image of the calibration target acquired with a 50x long working distance objective (NA 0.5, Olympus LMPLANFL) is presented in Fig. 5.4. Only structures with a grating period below 1630 line-pairs (lp) per mm can be distinguished. To further refine the measurement of spatial resolution, we captured an image of a slant sharp edge. From this image we could directly extract the edge response of our microscope, and by differentiation calculate the line spread function (LSF). Interestingly, the LSF is the 1D equivalent of the PSF of a microscope (image of a point source or impulse response), and thus from its Fourier transform we could retrieve the frequency response of our system, also known as MTF (Fig. 5.7). The MTF intuitively indicates contrast and it illustrates the behavior of a microscope as a filter, with the cutoff frequency (maximum resolution) conventionally considered at a 10% of the MTF (the Rayleigh resolution criterion corresponds to a 9% of the MTF). Our particular microscope objective presented a maximum resolution of 580 nm (equivalent NA of 0.42). For comparison, the optical performance of a diffraction-limited system was plotted in Fig. 5.7. The decrease in performance at high frequencies of our system with respect to the ideal case is expected due to imperfections in the design of "real" microscope objectives.

We repeated the above characterization for SMM, with a single microsphere placed on top of the different gratings. To avoid any potential interference caused by the cantilever during image formation, experiments were performed with no cantilever (the microsphere was positioned at targeted locations on the substrate and further detached from the cantilever, as detailed above). The presence of the cantilever, though, did not seem to affect the results. Remarkably, each microsphere

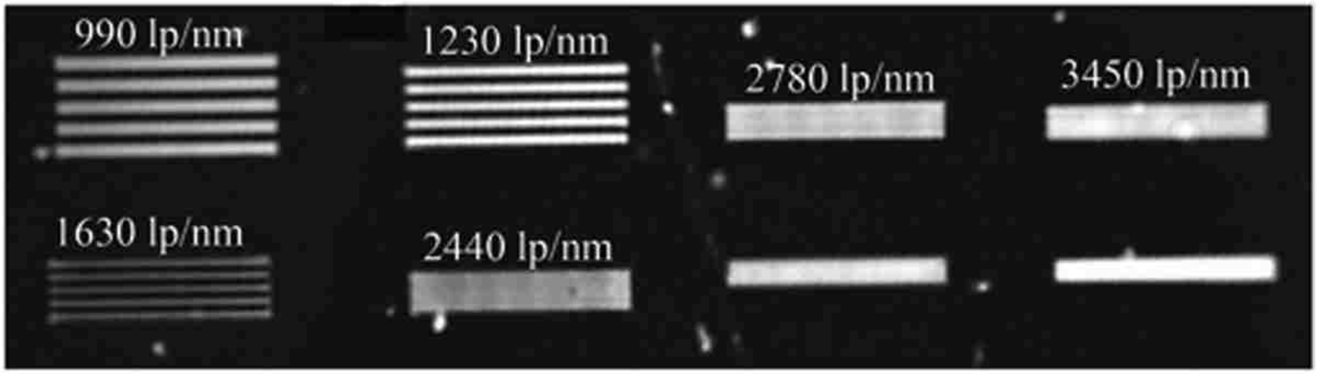

Figure 5.4: Optical micrograph acquired with the 50x objective of gratings imaged without the microsphere.

Figure 5.5: Details of three gratings imaged through the microsphere. Note that these frequencies could not be resolved without the microsphere.

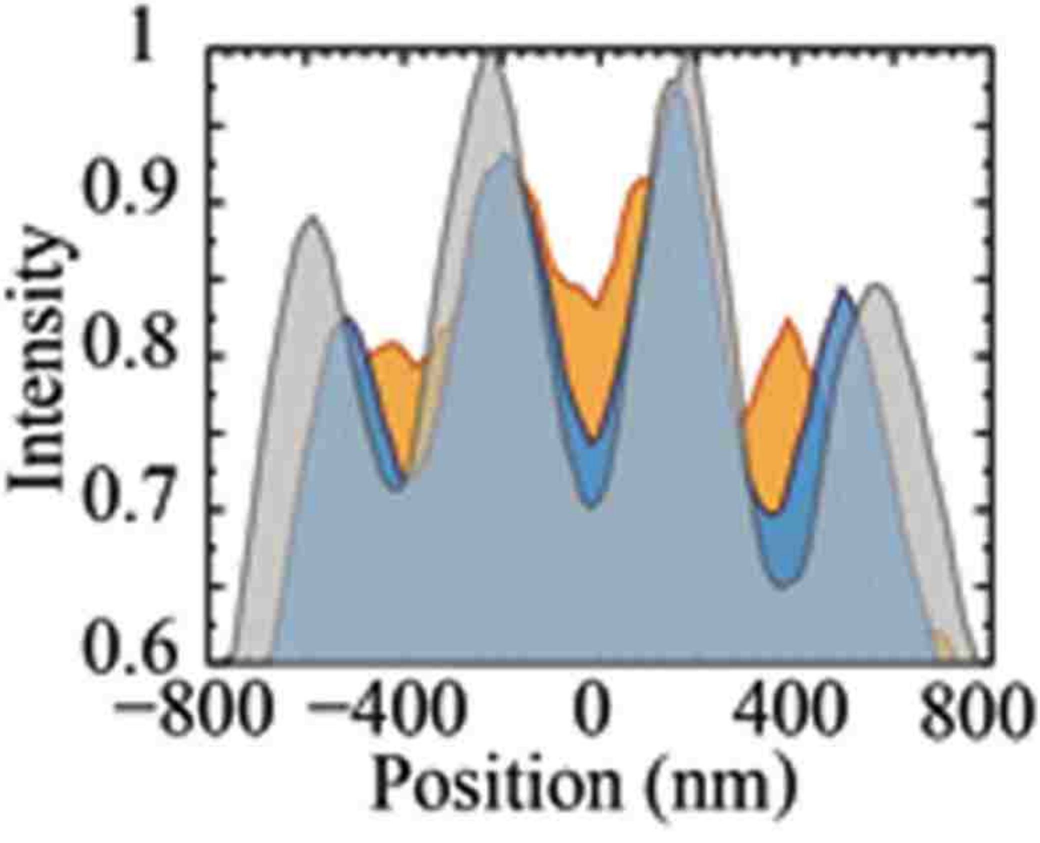

Figure 5.6: The corresponding intensity profiles (normalized with respect to 2440 lp/mm) for three gratings imaged through the microsphere shown in Fig. 5.5.

formed a virtual image at a distance of 4.5 μm below the sample surface, with a magnification factor of 2.8. Moreover, higher magnifications could be obtained by moving the objective focal plane further below the surface (up to a distance of about 9 μm an image could still be distinguished). However, at these positions the contrast was poorer while no higher spatial frequencies could be resolved, indicating a simple effect of "empty magnification" (magnification without gain in resolution). Interestingly, the microsphere enables to resolve frequencies not accessible with the conventional microscope, as shown in Figs. 5.5 and 5.6. Indeed, a grating with a spacing up to 3450 lp/mm could be clearly resolved. The corresponding MTF calculated using the slanted edge method is plotted in Fig. 5.7. Notably, the range of accessible frequencies in SMM was significantly extended compared to the microsphere-free microscope, with a maximum resolution of about 260 nm. Considering the Rayleigh criterion, this value indicates an enhancement in the effective numerical aperture of our system of a factor of 2.3, from 0.42 NA to an equivalent 0.95 NA objective. A similar behavior was observed with 2 additional objectives (20x 0.4 NA and 100x 0.8 NA). In both cases, the microsphere produced an improvement in spatial resolution, but with different enhancement factors. The results are summarized in Table 5.1. We can interpret the observed trend by considering the microsphere to act as a lens with a fixed numerical aperture of around 0.95. Thus, the simple introduction of the microsphere can effectively turn a regular microscope into a high NA system. Particular attention should be given to two different scenarios. First, when the initial NA of our system is already high, the effects of the microsphere become less apparent. In fact, the maximum resolution in our SMM system is limited to about 260 nm, even for the highest NA lenses tested. Second, given a low NA objective, it may not be possible to fully exploit the intrinsic high NA of the microsphere. In other words, the low NA objective may cutoff the high frequencies that the microsphere inherently can transfer into the far field. This helps explaining the lower effective NA of the 20x objective in the SMM configuration. Indeed, the initial objective NA was 0.3 (cutoff frequency of 1200 lp/mm), but the maximum resolution of the 20x objective, considering the 2.8 magnification factor, was only $2.8 \times 1200 = 3400$ lp/mm, which is equivalent to a 0.81 NA. Therefore, the optimal objective to be used in SMM should have a NA low enough to allow the microsphere to significantly increase the optical performance of the microscope, but sufficiently high to be able to resolve the highest frequencies that the microsphere couples into the far field.

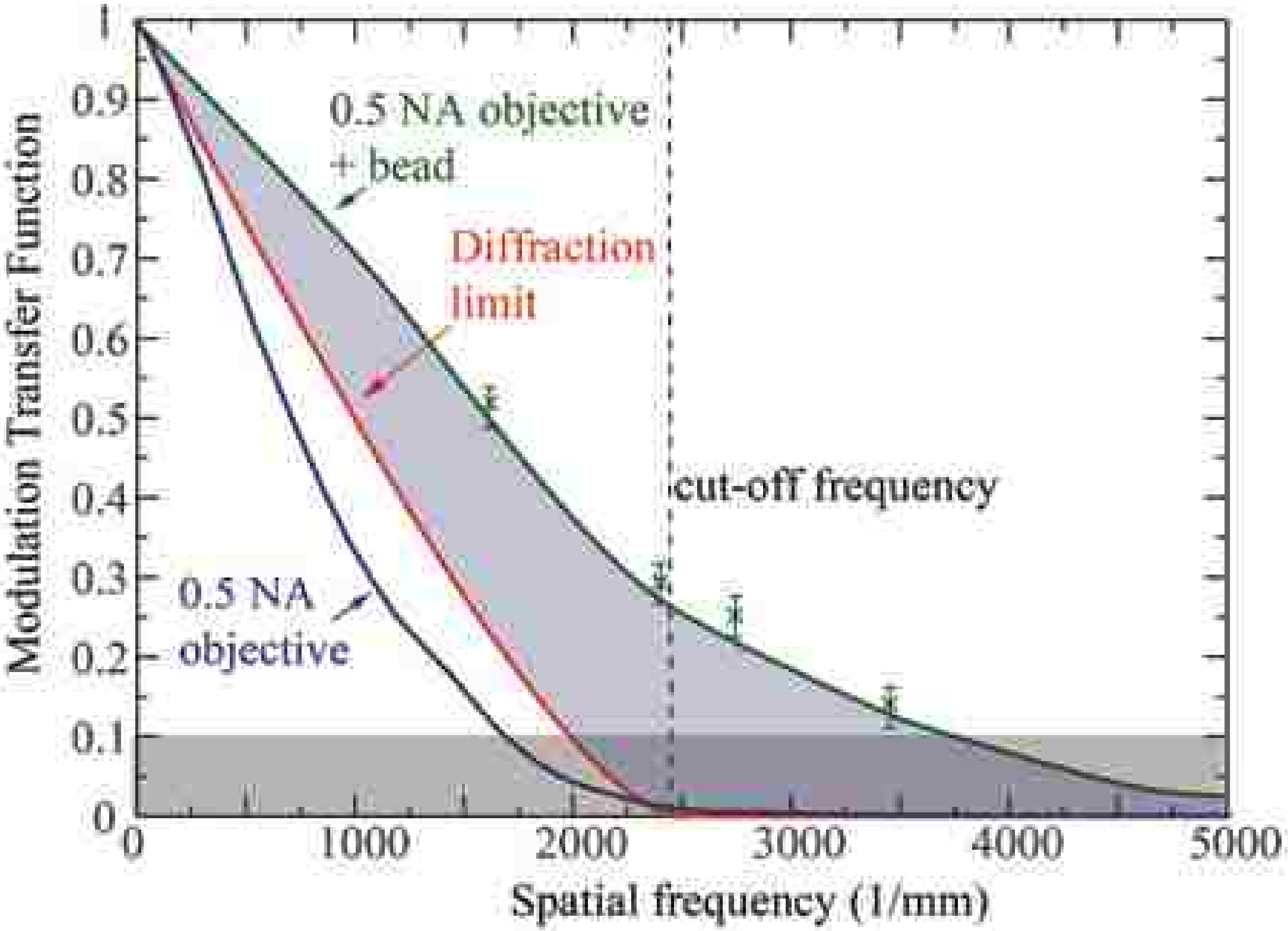

Figure 5.7: Frequency response of the microscope with and without microsphere. The response from a diffraction limited system has also been included. The gray area indicates the 10% MTF criterion used to define the maximum attainable resolution. The highlighted purple area indicates the enhancement in resolution achieved with SMM with respect to a perfect diffraction-limited system with a 0.5 NA. The cut-off frequency indicates the Abbe resolution limit for a 0.5 NA system.

To validate the idea of the microsphere as a high NA lens, we performed three dimensional FDTD simulations (Lumerical Solutions) of a simplified system consisting of two incoherent dipoles oscillating in xyz with a wavelength of 405 nm and placed in close proximity to a silica microsphere.

Table 5.1: Characterization of the effective NA of the different objectives used (10% MTF criterion), and the effective NA when imaging through the microsphere (SMM). The resolution enhancement is also included.

	Effective NA	SMM effective NA	Enhancement
20x 0.4 NA	0.3	0.80	2.7
50x 0.5 NA	0.42	0.95	2.3
100x 0.8 NA	0.69	0.97	1.4

The diameter of the microsphere (refractive index 1.46) was set to be 4.6 μm while as background material was chosen air. Perfect Matched Layer (PML) absorbing boundary condition was used for the entire simulation window.

Furthermore, convergence analysis was performed in order to guarantee solutions with an error below 5%. The schematic of the simulated layout, with two incoherent dipoles placed in contact with the microsphere and separated a distance Δd is shown in Fig. 5.8. More in detail, the electromagnetic field generated by the dipoles was calculated at the collecting plane (5.35 μm above the dipoles), namely after passing through the microsphere. Afterwards, the so calculated field was back-propagated upon removing the microsphere, as illustrated in Figs. 5.9 and 5.10 for Δd=250 nm and Δd=300 nm respectively. The position of maximum intensity was taken at the image plane, that is where the virtual image is formed [151]. As it can be observed in Fig. 5.11, dipoles separated by 250 nm could not be resolved using the Rayleigh criterion. To be noticed that the location of the image plane was at about 7.5 μm from the dipoles plane with a magnification factor equal to 3.1, in close agreement with experiment. By increasing the separation distance of the dipoles above 250 nm (Fig. 5.12), they become resolvable, as experimental results demonstrated. Therefore, the anticipated behavior of the microsphere as an optical element with an effective NA of about 0.95 is confirmed by the FDTD simulations.

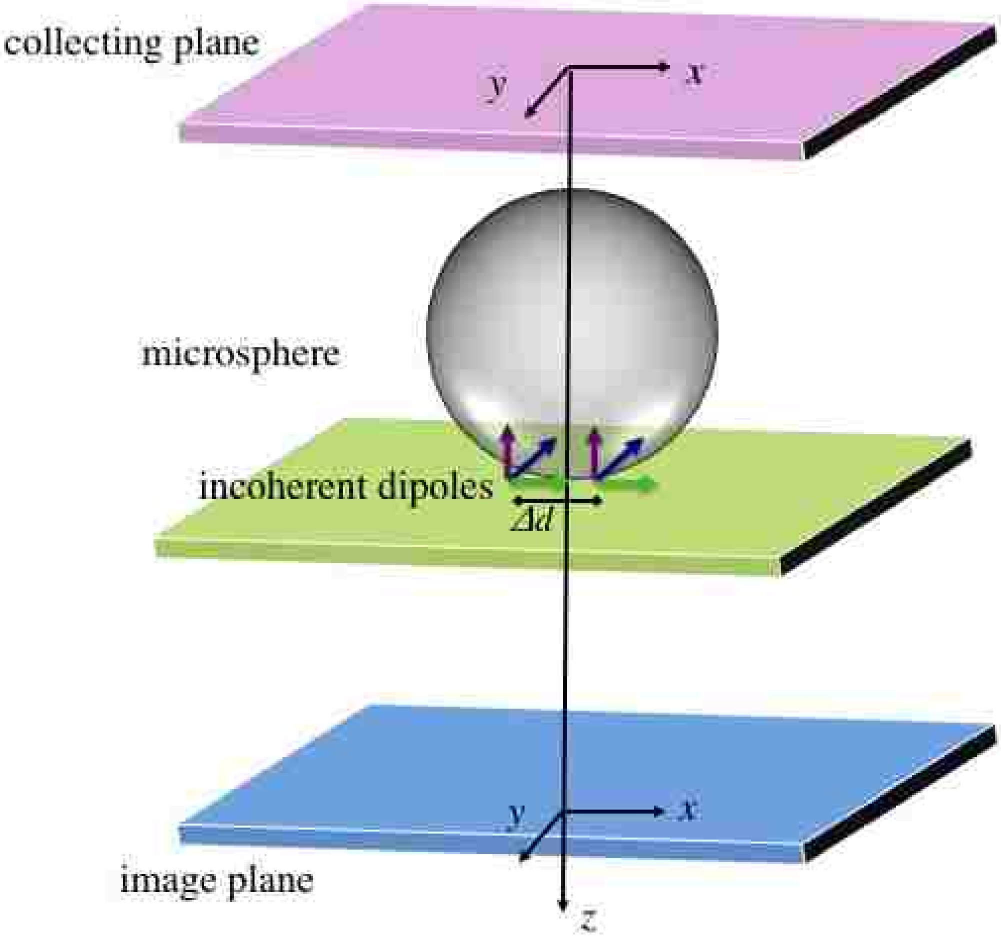

Figure 5.8: Schematic of the simulated layout, with two incoherent dipoles placed in contact with the silica microsphere with diameter of 4.7 μm, refractive index of 1.46 and separated a distance Δd.

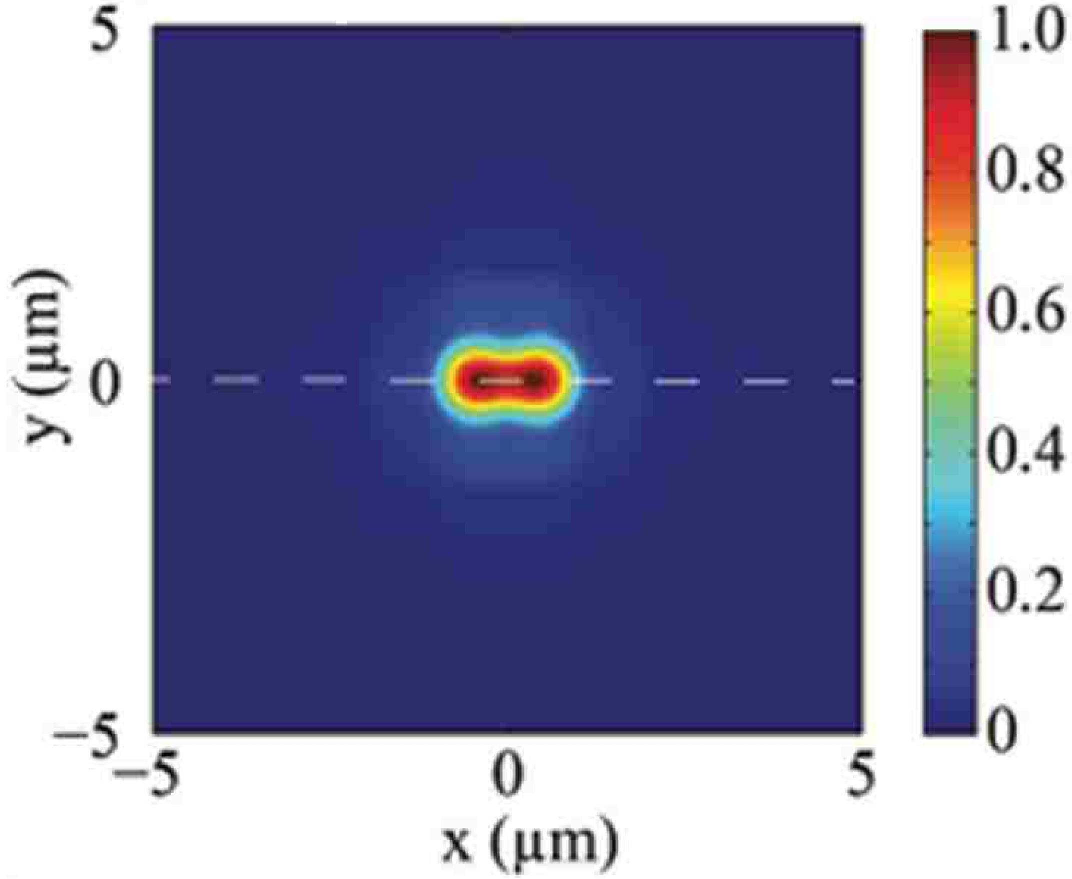

Figure 5.9: The electromagnetic field generated by the dipoles for Δd=250 nm is calculated in the collecting plane and back-propagated. The position of maximum intensity is considered the image plane.

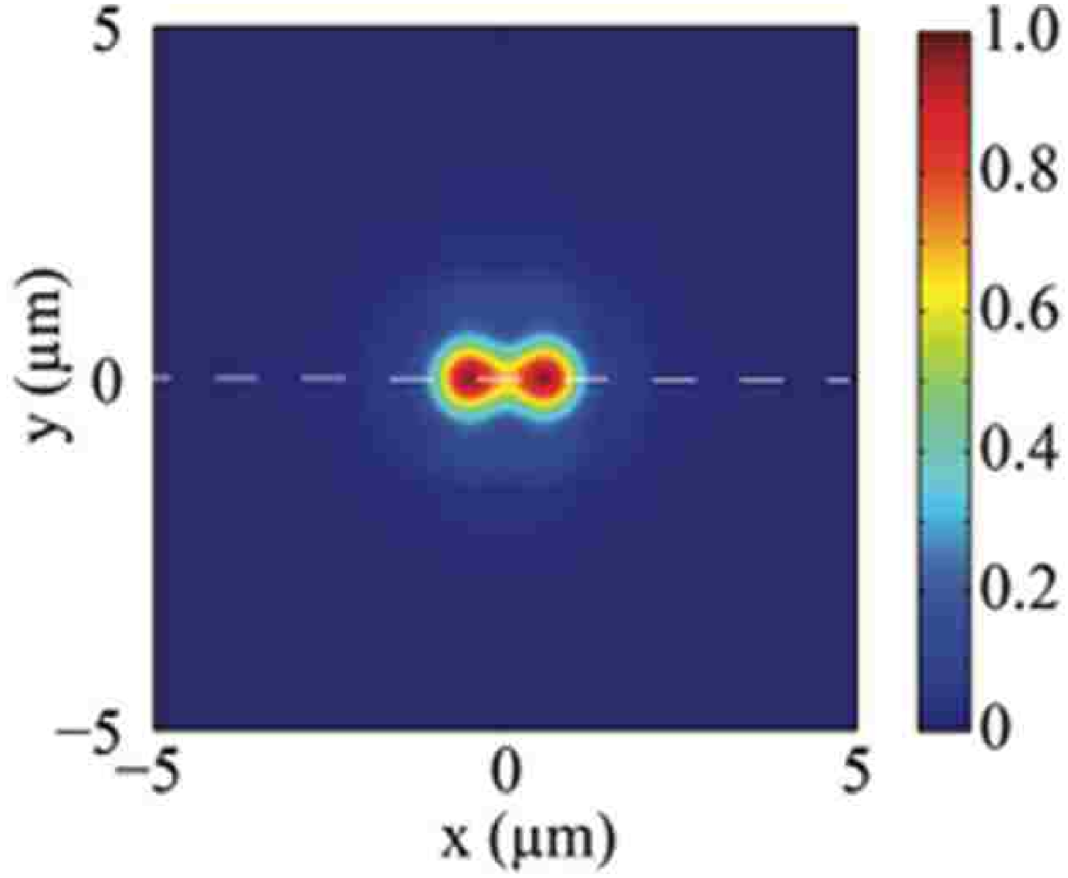

Figure 5.10: The electromagnetic field generated by the dipoles for Δd=300 nm is calculated in the collecting plane and back-propagated. The position of maximum intensity is considered the image plane.

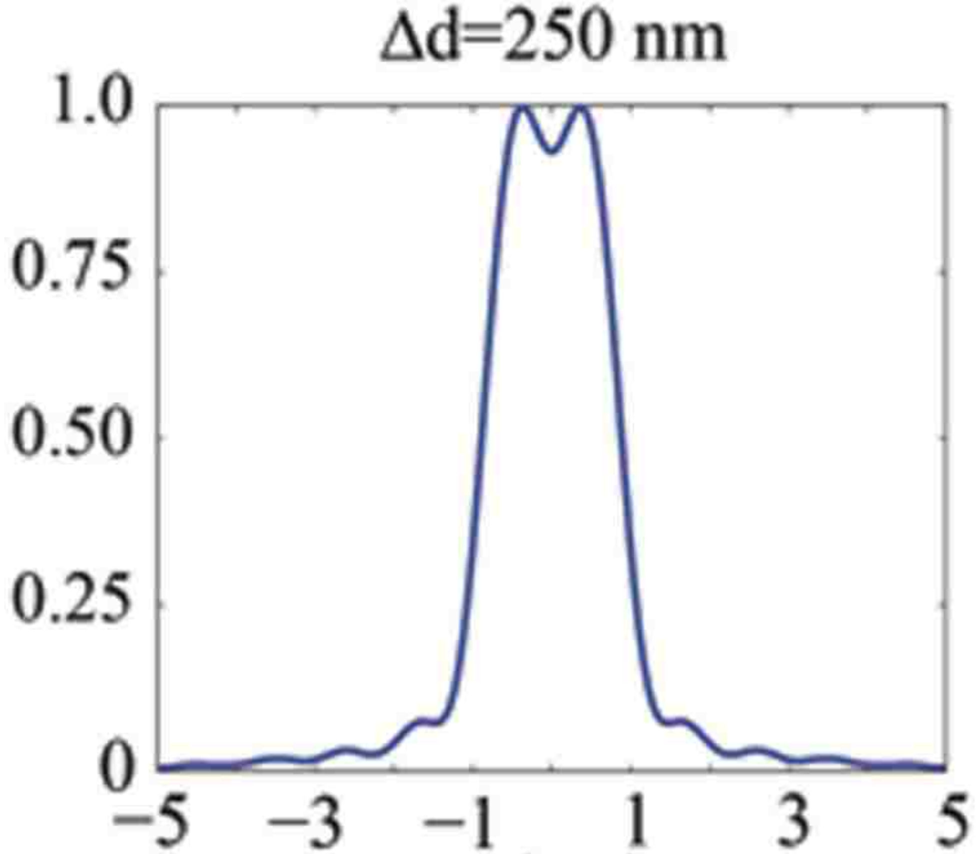

Figure 5.11: Normalized intensity profile for two dipoles separated 250 nm.

5.3 Discussion

It is important to discuss the implication of the results reported here and to put them in perspective. Using a 4.6 μm silica microsphere with 405 nm transmission illumination, SMM enhances the resolution of a microscope up to the limit imposed by an air focusing objective, but it does not break the diffraction limit. In fact, with a high NA immersion objective, resolutions below the 250 nm obtained in our SMM system can be achieved. This is in sharp contrast with resolution claims from previous works. However, none of them provided an accurate measurement of this parameter. For instance, a common imaged sample has been the periodic structures of Blu-ray disks or other patterns, which consist of ∼100 nm stripes separated by distances above 200 nm [138, 143, 145, 149, 150, 152, 153]. Conventionally, people have used the width of the stripes to claim super-resolution, which is misleading since it should be the total periodicity of the structure (∼300 nm) the parameter to be considered. This stems from the definition of resolution as the minimum distance at which two structures can be distinguished. Indeed, a point or line emitter with sub-diffraction size will appear as a blur in the image plane (PSF or LSF), which can be clearly distinguished, but this does not imply that the system resolution is given by the emitter size. Thereby, the ∼300 nm structure of a Blu-ray disk can be resolved in SMM but also by using a high NA objective. Other structures with deep sub-wavelength periodicities have been resolved in SMM, including 50 nm [141], 100 nm [138] and ∼160 nm [142, 145]. We tried to image structures of similar size with our system and could not resolve them. We believe there is a combination of effects to account for this. One of them is the difference in the experimental conditions. For instance, other imaging modalities such as a laser scanning confocal microscopy (LSCM) have been used [95]. Furthermore, microspheres of a higher refractive index material (n=1.9), or with a larger size (50 μm) and partially immersed in a fluid have been reported to further enhance the resolution in SMM [140]. Note that LSCM, provided a large enough photon budget when the pinhole is below 1 Airy Unit, is already a super-resolution approach (factor of 2 enhancement compared to wide-field microscopy) [154], whereas larger refractive index microspheres are expected to increase the light collection efficiency (NA) [145]. In addition, the effects of the particular substrate used [155] (i.e.

refractive index, plasmonic coupling, etc.) or the excitation of the electromagnetic modes [156] could also affect the ability of SMM to resolve a given structure. Overall, strong attention must be paid when claiming to reach a particular resolution in SMM, and the potential interferences that any of the different parameters can play on this quantity. We also included the corresponding simulation results for the case when we have hemisphere and protruded hemisphere in Appendix C.

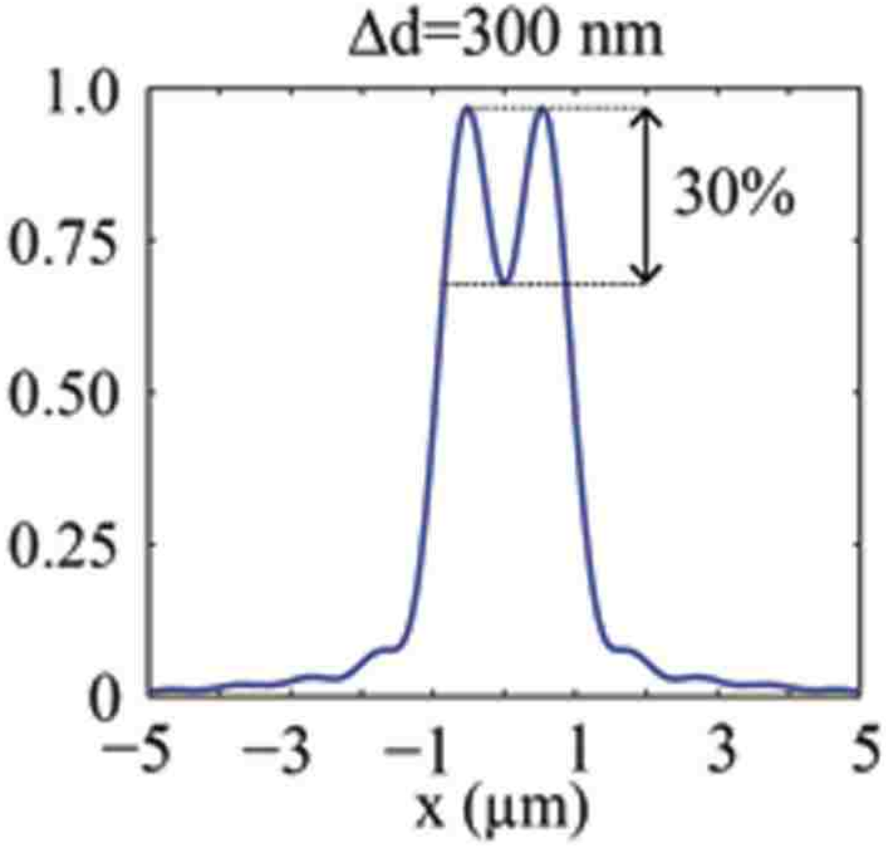

Figure 5.12: Normalized intensity profile for two dipoles separated 300 nm.

Chapter 6
Conclusions

We first briefly reviewed the history of achieving extraordinary optical transmission through subwavelength apertures and also the active control of the flow of light in plasmonic devices using externally applied magnetic fields. We then numerically investigated compact structures, consisting of multiple optical microcavities at both the entrance and exit sides of a subwavelength plasmonic slit, with the goal to enhance the directional transmission through the slit. Our reference structure consisted of a subwavelength slit in a metal film without microcavities. We found that for such a structure, as the slit length increases, the transmission cross section per unit angle in the normal direction exhibits peaks, corresponding to the Fabry-Perot resonances in the slit. As expected for a subwavelength slit in a metallic film, the radiation pattern is almost isotropic.

To enhance the directional transmission through the slit, we first considered a structure with a single microcavity at each of the entrance and exit sides of the slit. With such a structure we aimed to increase both the transmission of light through the slit, as well as the directivity in the normal direction. We found that the presence of the microcavities results in significantly larger reflectivity at the sides of the slit compared to a slit without microcavities. Thus, the resonance enhancement factor is greatly increased compared to the reference slit without microcavities. On the other hand, the increased reflectivity at the sides of the slit leads to decrease of the power radiated from the slit. Overall, the use of an optimized single microcavity at the entrance and exit sides of the slit results in a slit transmission cross section which is $\sim$1.8 times larger than the transmission cross section of the optimized slit without microcavities. We also found that for such a structure the radiation pattern is anisotropic, and the directivity in the normal direction is $\sim$2.6 times larger than the one of the optimized slit without microcavities. Overall, such a structure, when optimized, results in $1.8 \times 2.6 \sim 4.7$ times larger transmission cross section per unit angle in the normal direction compared to the optimized reference slit without microcavities.

To further enhance the transmission cross section per unit angle of the slit in the normal direction, we considered a structure with multiple microcavities at both the entrance and exit sides of the slit. We found that, unlike the optimized single-microcavity structure in which the increased transmission is associated with increased resonance enhancement in the slit, for an optimized double-microcavity structure the increased transmission is mostly associated with improved impedance matching between free-space waves and the slit mode. Such a structure enhances both the incoupling of normally incident light from free space into the slit mode, as well as the outcoupling of light from the slit mode to free-space radiation in the normal direction. The use of two optimized microcavities at the entrance and exit sides of the slit results in a slit transmission cross section which is $\sim$3.7 times larger than the transmission cross section of the optimized slit without microcavities. We also found that for such a structure the directivity in the normal direction is $\sim$4.1 times larger than the one of the optimized reference slit without microcavities. Overall, the double-microcavity structure, when optimized, results in $3.7 \times 4.1 \sim 16$ times larger transmission cross section per unit angle in the normal direction compared to the optimized reference slit without microcavities. We also found that, while all structures were optimized at a single wavelength, the operation frequency range for high emission in the normal direction is broad.

We then introduced highly compact resonant-cavity-enhanced magneto-optical switches for MDM plasmonic waveguides. We applied the external static magnetic field to the metal and derived the dispersion relation. We observed that the dispersion relation depends only on the square of the propagation constant k. We found however that the corresponding field profiles are different. In addition to the numerically calculated magnetic field amplitude profile obtained with FDFD, we also showed the analytically calculated profile, obtained by solving the dispersion relation of the modes supported by the waveguide. We observed that there is excellent agreement between the analytical results and the numerical results obtained using the FDFD method. We also investigated the effect of the externally applied static magnetic field on the propagation constant of the mode. We observed that the real part of the propagation constant of the waveguide mode in the presence of the magnetic field $\mathrm{Re}[k(\omega_B = 0.1\omega_P)]$ is larger than the real part of the propagation constant of the mode in the absence of the magnetic field $\mathrm{Re}[k(\omega_B = 0)]$. We also defined the magnetic field induced wave vector modulation as $|\Delta k(\omega_B)/k| \equiv |\frac{k(\omega_B)-k(\omega_B=0)}{k(\omega_B=0)}|$. We observed that, as the frequency increases, both the magnetic field induced change in the propagation constant, as well as the magnetic field induced wave vector modulation increase. As a final step, we investigated a Fabry-Perot cavity structure consisting of a MDM waveguide side-coupled to two MDM stub resonators. The metal was subject to an externally applied static magnetic field. By using two stubs and properly tuning the length of the cavity L formed between them, the difference in transmission between the on and off states, and therefore the modulation depth of the switch, defined as $[T(\omega_B = 0.1\omega_P) - T(\omega_B = 0)]/T(\omega_B = 0.1\omega_P)$, can be resonantly enhanced compared to the single-stub structure. Thus, such a Fabry-Perot cavity structure can act as a magneto-optical switch, in which the on/off states correspond to the presence/absence of externally applied static magnetic field.

We also showed that strong coupling can occur between J-aggregate molecules and SPPs supported by gold nanohole arrays. We investigated the dynamics of the formed hybrid state with different coupling strengths by using a femto-second pump–probe approach. Under upper band resonant excitation, two distinctive bleaching bands appeared in the transient absorption spectra showing an increased Rabi splitting upon increase of the concentration of J-aggregate molecules. This result was indeed confirmed by static measurements. Furthermore, the non-thermal kinetics of the hybrid state indicates that the upper band has an intrinsic long lifetime that depends on the Rabi splitting values as well. Our measurements suggest that the phonon bottleneck relaxation mechanism might play an important role in SPP-related dynamics processes. With stronger coupling strength, the bottleneck effect is suppressed, leading to a shorter lifetime of the upper hybrid band. This indicates that the coupling strength alters the dynamics of the hybrid system and offers new insights into the intrinsic photophysics of strong coupling.

We also proposed a portable microsphere system and discussed the corresponding optical characterization. We showed that microspheres can enhance the optical performance of bright-field microscopes provided an initial low NA objective. Under conditions described herein, microspheres behave as optical lenses with a NA of around 0.95, capable to extend the response of a low NA objective to higher spatial frequencies. In this sense, SMM is a simple and affordable alternative to traditionally expensive immersion objectives or other imaging modalities. Furthermore, the integration of microspheres with an AFM system opens the door to correlative approaches for combining optical characterization tools, such as imaging or Raman spectroscopy, with the different AFM modalities (force mapping, topography), which could help getting further insights about the intrinsic properties of materials.

References

[1] S. A. Maier, P. G. Kik, H. A. Atwater, S. Meltzer, E. Harel, B. E. Koel, and A. A. Requicha, "Local detection of electromagnetic energy transport below the diffraction limit in metal nanoparticle plasmon waveguides," *Nat. Mater.*, vol. 2, no. 4, pp. 229–232, 2003.

[2] P. Dastmalchi, A. Haddadpour, and G. Veronis, *Nanophotonics: devices for manipulating light at the nanoscale*. No. 42, Woodhead Publishing Series in Electronic and Optical Materials, 2014.

[3] B. Schechter, "Bright new world," *New Sci.*, no. 2392, pp. 30–33, 2003.

[4] T. W. Ebbesen, H. J. Lezec, H. Ghaemi, T. Thio, and P. Wolff, "Extraordinary optical transmission through sub-wavelength hole arrays," *Nature*, vol. 391, no. 6668, pp. 667–669, 1998.

[5] S. Carretero-Palacios, O. Mahboub, F. Garcia-Vidal, L. Martin-Moreno, S. G. Rodrigo, C. Genet, and T. Ebbesen, "Mechanisms for extraordinary optical transmission through bull's eye structures," *Opt. Express*, vol. 19, no. 11, pp. 10429–10442, 2011.

[6] C. Genet and T. W. Ebbesen, "Light in tiny holes," *Nature*, vol. 445, no. 7123, pp. 39–46, 2007.

[7] Z. Yu, G. Veronis, S. Fan, and M. L. Brongersma, "Design of midinfrared photodetectors enhanced by surface plasmons on grating structures," *Appl. Phys. Lett.*, vol. 89, no. 15, p. 151116, 2006.

[8] H. J. Lezec, A. Degiron, E. Devaux, R. A. Linke, L. Martin-Moreno, F. Garcia-Vidal, and T. Ebbesen, "Beaming light from a subwavelength aperture," *Science*, vol. 297, no. 5582, pp. 820–822, 2002.

[9] L. Martin-Moreno, F. Garcia-Vidal, H. Lezec, A. Degiron, and T. W. Ebbesen, "Theory of highly directional emission from a single subwavelength aperture surrounded by surface corrugations," *Phys. Rev. Lett.*, vol. 90, no. 16, p. 167401, 2003.

[10] F. López-Tejeira, S. G. Rodrigo, L. Martín-Moreno, F. J. García-Vidal, E. Devaux, T. W. Ebbesen, J. R. Krenn, I. Radko, S. I. Bozhevolnyi, M. U. González, *et al.*, "Efficient unidirectional nanoslit couplers for surface plasmons," *Nature Phys.*, vol. 3, no. 5, pp. 324–328, 2007.

[11] T. Ishi, J. Fujikata, K. Makita, T. Baba, and K. Ohashi, "Si nano-photodiode with a surface plasmon antenna," *Jpn. J. Appl. Phys.*, vol. 44, no. 3L, pp. L364–L366, 2005.

[12] W. Cai, J. S. White, and M. L. Brongersma, "Compact, high-speed and power-efficient electrooptic plasmonic modulators," *Nano Lett.*, vol. 9, no. 12, pp. 4403–4411, 2009.

[13] G. Gbur, H. F. Schouten, and T. D. Visser, "Achieving superresolution in near-field optical data readout systems using surface plasmons," *Appl. Phys. Lett.*, vol. 87, no. 19, p. 191109, 2005.

[14] J. Fujikata, T. Ishi, H. Yokota, K. Kato, M. Yanagisawa, M. Nakada, K. Ishihara, K. Ohashi, T. Thio, and R. Linke, "Surface plasmon enhancement effect and its application to near-field optical recording," *Trans. Magn. Soc. Japan*, vol. 4, no. 4-2, pp. 255–259, 2004.

[15] S. Shinada, J. Hashizume, and F. Koyama, "Surface plasmon resonance on microaperture vertical-cavity surface-emitting laser with metal grating," *Appl. Phys. Lett.*, vol. 83, no. 5, pp. 836–838, 2003.

[16] B. Guo, G. Song, and L. Chen, "Plasmonic very-small-aperture lasers," *Appl. Phys. Lett.*, vol. 91, no. 2, p. 021103, 2007.

[17] J. Wen, W. Wang, N. Li, Z. Li, and W. Lu, "Light enhancement by metal-insulator-metal plasmonic focusing cavity," *Opt. and Quant. Elect.*, vol. 48, no. 2, pp. 1–8, 2016.

[18] D. E. Grupp, H. J. Lezec, T. Thio, and T. W. Ebbesen, "Beyond the Bethe limit: Tunable enhanced light transmission through a single sub-wavelength aperture," *Adv. Mater.*, vol. 11, no. 10, pp. 860–862, 1999.

[19] L. Verslegers, Z. Yu, P. B. Catrysse, and S. Fan, "Temporal coupled-mode theory for resonant apertures," *J. Opt. Soc. Am. B*, vol. 27, no. 10, pp. 1947–1956, 2010.

[20] Q. Min and R. Gordon, "Surface plasmon microcavity for resonant transmission through a slit in a gold film," *Opt. Express*, vol. 16, no. 13, pp. 9708–9713, 2008.

[21] P. Ginzburg and M. Orenstein, "Plasmonic transmission lines: from micro to nano scale with $\lambda/4$ impedance matching," *Opt. Express*, vol. 15, no. 11, pp. 6762–6767, 2007.

[22] C. Min, L. Yang, and G. Veronis, "Microcavity enhanced optical absorption in subwavelength slits," *Opt. Express*, vol. 19, no. 27, pp. 26850–26858, 2011.

[23] E. Ozbay, "Plasmonics: merging photonics and electronics at nanoscale dimensions," *Science*, vol. 311, no. 5758, pp. 189–193, 2006.

[24] A. V. Krasavin and N. I. Zheludev, "Active plasmonics: Controlling signals in Au/Ga waveguide using nanoscale structural transformations," *Appl. Phys. Lett.*, vol. 84, no. 8, pp. 1416–1418, 2004.

[25] K. F. MacDonald and N. I. Zheludev, "Active plasmonics: current status," *Laser Photon. Rev.*, vol. 4, no. 4, pp. 562–567, 2010.

[26] V. V. Temnov, G. Armelles, U. Woggon, D. Guzatov, A. Cebollada, A. Garcia-Martin, J.-M. Garcia-Martin, T. Thomay, A. Leitenstorfer, and R. Bratschitsch, "Active magneto-plasmonics in hybrid metal-ferromagnet structures," *Nature Photon.*, vol. 4, pp. 107–111, 02 2010.

[27] S. Fan, “Nanophotonics: Magnet-controlled plasmons,” *Nature Photon.*, vol. 4, no. 2, pp. 76–77, 2010.

[28] M. Freiser, “A survey of magnetooptic effects,” *IEEE Trans. Magn.*, vol. 4, no. 2, pp. 152–161, 1968.

[29] G. Armelles, A. Cebollada, A. García-Martín, and M. U. González, “Magnetoplasmonics: Combining magnetic and plasmonic functionalities,” *Adv. Opt. Mater.*, vol. 1, no. 1, pp. 10–35, 2013.

[30] H. Raether, *Surface plasmons on smooth surfaces.* Springer, 1988.

[31] E. Palik and J. Furdyna, “Infrared and microwave magnetoplasma effects in semiconductors,” *Rep. Prog. Phys.*, vol. 33, no. 3, pp. 1193–1322, 1970.

[32] J. D. Jackson, *Classical Electrodynamics.* Wiley, 1998.

[33] Z. Yu, G. Veronis, Z. Wang, and S. Fan, “One-way electromagnetic waveguide formed at the interface between a plasmonic metal under a static magnetic field and a photonic crystal,” *Phys. Rev. Lett.*, vol. 100, p. 023902, Jan 2008.

[34] B. Hu, Q. J. Wang, S. W. Kok, and Y. Zhang, “Active focal length control of terahertz slitted plane lenses by magnetoplasmons,” *Plasmonics*, vol. 7, no. 2, pp. 191–199, 2012.

[35] H. Dötsch, N. Bahlmann, O. Zhuromskyy, M. Hammer, L. Wilkens, R. Gerhardt, P. Hertel, and A. F. Popkov, “Applications of magneto-optical waveguides in integrated optics: review,” *J. Opt. Soc. Am. B*, vol. 22, no. 1, pp. 240–253, 2005.

[36] G. Mathew, C. Bhagyaraj, A. Babu, and V. Mathew, “Effect of gyrotropic substrates on the surface plasmon polaritons guided by metal films of finite width,” *J. Lightwave Technol.*, vol. 30, no. 2, pp. 273–278, 2012.

[37] B. Sepulveda, L. M. Lechuga, and G. Armelles, “Magnetooptic effects in surface-plasmon-polaritons slab waveguides,” *J. Lightwave Technol.*, vol. 24, no. 2, pp. 945–955, 2006.

[38] A. B. Khanikaev, S. H. Mousavi, G. Shvets, and Y. S. Kivshar, “One-way extraordinary optical transmission and nonreciprocal spoof plasmons,” *Phys. Rev. Lett.*, vol. 105, no. 12, p. 126804, 2010.

[39] P. Ferguson, O. Stafsudd, and R. Wallis, “Enhancement of the transverse Kerr magneto-optic effect by surface magnetoplasma waves,” *Physica B*, vol. 89, pp. 91–94, 1977.

[40] N. Richard, A. Dereux, T. David, E. Bourillot, J. Goudonnet, F. Scheurer, E. Beaurepaire, and G. Garreau, “Magneto-optical effects in multilayers illuminated by total internal reflection,” *Phys. Rev. B.*, vol. 59, no. 8, pp. 5936–5944, 1999.

[41] C. Hermann, V. Kosobukin, G. Lampel, J. Peretti, V. Safarov, and P. Bertrand, “Surface-enhanced magneto-optics in metallic multilayer films,” *Phys. Rev. B.*, vol. 64, no. 23, p. 235422, 2001.

[42] J.-H. Park, H. Takagi, J.-K. Cho, K. Nishimura, H. Uchida, and M. Inoue, “Magnetooptic spatial light modulator with one-step pattern growth on ion-milled substrates by liquid-phase epitaxy,” *IEEE Trans. Magn.*, vol. 40, no. 4, pp. 3045–3047, 2004.

[43] K. J. Chau, S. E. Irvine, and A. Y. Elezzabi, “A gigahertz surface magneto-plasmon optical modulator,” *IEEE J. Quantum Electron.*, vol. 40, no. 5, pp. 571–579, 2004.

[44] M. Khatir and N. Granpayeh, “An ultra compact and high speed magneto-optic surface plasmon switch,” *J. Lightwave Technol.*, vol. 31, no. 7, pp. 1045–1054, 2013.

[45] V. Bonanni, S. Bonetti, T. Pakizeh, Z. Pirzadeh, J. Chen, J. Nogués, P. Vavassori, R. Hillenbrand, J. Åkerman, and A. Dmitriev, “Designer magnetoplasmonics with nickel nanoferromagnets,” *Nano Lett.*, vol. 11, no. 12, pp. 5333–5338, 2011.

[46] J. Montoya, K. Parameswaran, J. Hensley, M. Allen, and R. Ram, “Surface plasmon isolator based on nonreciprocal coupling,” *J. Appl. Phys.*, vol. 106, no. 2, p. 023108, 2009.

[47] J. S. White, G. Veronis, Z. Yu, E. S. Barnard, A. Chandran, S. Fan, and M. L. Brongersma, “Extraordinary optical absorption through subwavelength slits,” *Opt. Lett.*, vol. 34, no. 5, pp. 686–688, 2009.

[48] J.-M. Yi, A. Cuche, E. Devaux, C. Genet, and T. W. Ebbesen, “Beaming visible light with a plasmonic aperture antenna,” *ACS Photonics*, vol. 1, no. 4, pp. 365–370, 2014.

[49] J. Qi, T. Kaiser, R. Peuker, T. Pertsch, F. Lederer, and C. Rockstuhl, “Highly resonant and directional optical nanoantennas,” *J. Opt. Soc. Am. A*, vol. 31, no. 2, pp. 388–393, 2014.

[50] W. Wang, D. Zhao, Y. Chen, H. Gong, X. Chen, S. Dai, Y. Yang, Q. Li, and M. Qiu, “Grating-assisted enhanced optical transmission through a seamless gold film,” *Opt. Express*, vol. 22, no. 5, pp. 5416–5421, 2014.

[51] P. Kuang, J.-M. Park, G. Liu, Z. Ye, W. Leung, S. Chaudhary, D. Lynch, K.-M. Ho, and K. Constant, “Metal-nanowall grating transparent electrodes: Achieving high optical transmittance at high incident angles with minimal diffraction,” *Opt. Express*, vol. 21, no. 2, pp. 2393–2401, 2013.

[52] Y. Liang, W. Peng, R. Hu, and H. Zou, “Extraordinary optical transmission based on subwavelength metallic grating with ellipse walls,” *Opt. Express*, vol. 21, no. 5, pp. 6139–6152, 2013.

[53] F. Garcıa-Vidal, L. Martın-Moreno, H. Lezec, and T. Ebbesen, “Focusing light with a single subwavelength aperture flanked by surface corrugations,” *Appl. Phys. Lett.*, vol. 83, no. 22, pp. 4500–4502, 2003.

[54] N. Yu, Q. Wang, and F. Capasso, “Beam engineering of quantum cascade lasers,” *Laser Photon. Rev.*, vol. 6, no. 1, pp. 24–46, 2012.

[55] A. Haddadpour and G. Veronis, “Microcavity enhanced directional transmission through a subwavelength plasmonic slit,” *Opt. Express*, vol. 23, no. 5, pp. 5789–5799, 2015.

[56] G. Veronis and S. Fan, "Surface plasmon nanophotonics," *Surface Plasmon Nanophotonics, M. L. Brongersma and P. G. Kik, eds. (Springer, 2007), Vol. 131*, p. 169.

[57] E. D. Palik, *Handbook of optical constants of solids*, vol. 3. Academic press, 1998.

[58] J.-M. Jin, *The finite element method in electromagnetics.* John Wiley & Sons, 2002.

[59] A. Taflove and S. C. Hagness, "Computational electrodynamics: the finite-difference time-domain method," *Norwood, 2nd Edition, MA: Artech House*, 1995.

[60] S. E. Kocabas, G. Veronis, D. A. Miller, and S. Fan, "Transmission line and equivalent circuit models for plasmonic waveguide components," *IEEE J. Sel. Topics Quantum Electron.*, vol. 14, no. 6, pp. 1462–1472, 2008.

[61] C. A. Balanis, *Antenna theory: analysis and design.* John Wiley & Sons, 2005.

[62] Y. Huang, C. Min, L. Yang, and G. Veronis, "Nanoscale plasmonic devices based on metal-dielectric-metal stub resonators," *Int. J. Opt.*, vol. 2012, p. 372048, 2012.

[63] G. Veronis and S. Fan, "Theoretical investigation of compact couplers between dielectric slab waveguides and two-dimensional metal-dielectric-metal plasmonic waveguides," *Opt. Express*, vol. 15, no. 3, pp. 1211–1221, 2007.

[64] Z. Yu, A. Raman, and S. Fan, "Fundamental limit of nanophotonic light trapping in solar cells," *PNAS*, vol. 107, no. 41, pp. 17491–17496, 2010.

[65] Z. Ruan and S. Fan, "Superscattering of light from subwavelength nanostructures," *Phys. Rev. Lett.*, vol. 105, no. 1, p. 013901, 2010.

[66] K. X. Wang, Z. Yu, S. Sandhu, V. Liu, and S. Fan, "Condition for perfect antireflection by optical resonance at material interface," *Optica*, vol. 1, no. 6, pp. 388–395, 2014.

[67] K. Krishnakumar, "Micro-genetic algorithms for stationary and non-stationary function optimization," in *1989 Advances in Intelligent Robotics Systems Conference*, pp. 289–296, International Society for Optics and Photonics, 1990.

[68] H. Zhu and C. Jiang, "Nonreciprocal extraordinary optical transmission through subwavelength slits in metallic film," *Opt. Lett.*, vol. 36, no. 8, pp. 1308–1310, 2011.

[69] J. B. Khurgin, "Optical isolating action in surface plasmon polaritons," *Appl. Phys. Lett.*, vol. 89, no. 25, p. 251115, 2006.

[70] M. S. Kushwaha and P. Halevi, "Magnetoplasmons in thin films in the Voigt configuration," *Phys. Rev. B*, vol. 36, pp. 5960–5967, 1987.

[71] K. Chiu and J. Quinn, "Magneto-plasma surface waves in solids," *Il Nuovo Cimento B (1971-1996)*, vol. 10, no. 1, pp. 1–20, 1972.

[72] V. A. Dmitriev and A. O. Silva, "Nonreciprocal properties of surface plasmon-polaritons at the interface between two magnetized media: Exact analytical solutions," *Prog. Electromagn. Res.*, vol. 21, pp. 177–186, 2011.

[73] G. Armelles, A. Cebollada, A. García-Martín, J. M. García-Martín, M. U. González, J. B. González-Díaz, E. Ferreiro-Vila, and J. Torrado, "Magnetoplasmonic nanostructures: systems supporting both plasmonic and magnetic properties," *J. Opt. A*, vol. 11, no. 11, p. 114023, 2009.

[74] P. Haefner, E. Luck, and E. Mohler, "Magnetooptical properties of surface plasma waves on copper, silver, gold, and aluminum," *Phys. Status Solidi B*, vol. 185, no. 1, pp. 289–299, 1994.

[75] D. Nikolova and A. Fisher, "Switching and propagation of magnetoplasmon polaritons in magnetic slot waveguides and cavities," *Phys. Rev. B*, vol. 88, no. 12, p. 125136, 2013.

[76] B. Hu, Y. Zhang, and Q. J. Wang, "Surface magneto plasmons and their applications in the infrared frequencies," *Nanophotonics*, vol. 4, 2015.

[77] E. Ferreiro-Vila, J. M. García-Martín, A. Cebollada, G. Armelles, and M. U. González, "Magnetic modulation of surface plasmon modes in magnetoplasmonic metal-insulator-metal cavities," *Opt. Express*, vol. 21, no. 4, pp. 4917–4930, 2013.

[78] A. Haddadpour, V. F. Nezhad, Z. Yu, and G. Veronis, "Highly compact magneto-optical switches for metal-dielectric-metal plasmonic waveguides," *Opt. Lett.*, vol. 41, no. 18, pp. 4340–4343, 2016.

[79] Y. Huang, C. Min, and G. Veronis, "Compact slit-based couplers for metal-dielectric-metal plasmonic waveguides," *Opt. Express*, vol. 20, no. 20, pp. 22233–22244, 2012.

[80] A. Haddadpour, V. Foroughi Nezhad, Z. Yu, and G. Veronis, "Magneto-optical switches in metal-dielectric-metal plasmonic waveguides," *Proc. SPIE*, vol. 9546, p. 95461S, 2015.

[81] G. Veronis and S. Fan, "Modes of subwavelength plasmonic slot waveguides," *J. Lightwave Technol.*, vol. 25, no. 9, pp. 2511–2521, 2007.

[82] C. Min and G. Veronis, "Absorption switches in metal-dielectric-metal plasmonic waveguides," *Opt. Express*, vol. 17, no. 13, pp. 10757–10766, 2009.

[83] L. Shen, X. Zheng, and X. Deng, "Stopping terahertz radiation without backscattering over a broad band," *Opt. Express*, vol. 23, no. 9, pp. 11790–11798, 2015.

[84] T. H. Isaac, W. L. Barnes, and E. Hendry, "Determining the terahertz optical properties of subwavelength films using semiconductor surface plasmons," *Appl. Phys. Lett.*, vol. 93, no. 24, p. 241115, 2008.

[85] D. Jalas, A. Petrov, M. Eich, W. Freude, S. Fan, Z. Yu, R. Baets, M. Popovic, A. Melloni, J. D. Joannopoulos, *et al.*, "What is and what is not an optical isolator," *Nature Photon.*, vol. 7, no. 8, pp. 579–582, 2013.

[86] S. Panaro, A. Nazir, C. Liberale, G. Das, H. Wang, F. De Angelis, R. Proietti Zaccaria, E. Di Fabrizio, and A. Toma, "Dark to bright mode conversion on dipolar nanoantennas: a symmetry-breaking approach," *ACS Photonics*, vol. 1, no. 4, pp. 310–314, 2014.

[87] J. Song, R. P. Zaccaria, M. Yu, and X. Sun, "Tunable Fano resonance in photonic crystal slabs," *Opt. Express*, vol. 14, no. 19, pp. 8812–8826, 2006.

[88] A. Salomon, S. Wang, J. A. Hutchison, C. Genet, and T. W. Ebbesen, "Strong light-molecule coupling on plasmonic arrays of different symmetry," *ChemPhysChem*, vol. 14, no. 9, pp. 1882–1886, 2013.

[89] A. González-Tudela, P. Huidobro, L. Martín-Moreno, C. Tejedor, and F. García-Vidal, "Theory of strong coupling between quantum emitters and propagating surface plasmons," *Phys. Rev. Lett.*, vol. 110, no. 12, p. 126801, 2013.

[90] Y.-W. Hao, H.-Y. Wang, Y. Jiang, Q.-D. Chen, K. Ueno, W.-Q. Wang, H. Misawa, and H.-B. Sun, "Hybrid-state dynamics of gold nanorods/dye J-aggregates under strong coupling," *Angew. Chem.*, vol. 123, no. 34, pp. 7970–7974, 2011.

[91] J. Bellessa, C. Symonds, K. Vynck, A. Lemaitre, A. Brioude, L. Beaur, J. Plenet, P. Viste, D. Felbacq, E. Cambril, *et al.*, "Giant Rabi splitting between localized mixed plasmon-exciton states in a two-dimensional array of nanosize metallic disks in an organic semiconductor," *Phys. Rev. B.*, vol. 80, no. 3, p. 033303, 2009.

[92] Y. Sugawara, T. Kelf, J. Baumberg, M. Abdelsalam, and P. Bartlett, "Strong coupling between localized plasmons and organic excitons in metal nanovoids," *Phys. Rev. Lett.*, vol. 97, no. 26, p. 266808, 2006.

[93] J. Dintinger, S. Klein, F. Bustos, W. L. Barnes, and T. Ebbesen, "Strong coupling between surface plasmon-polaritons and organic molecules in subwavelength hole arrays," *Phys. Rev. B.*, vol. 71, no. 3, p. 035424, 2005.

[94] Y.-F. Zhang, D.-J. Yang, J.-H. Wang, Y.-L. Wang, S.-J. Ding, L. Zhou, Z.-H. Hao, and Q.-Q. Wang, "Multiple hybridized resonances of IR-806 chromonic molecules strongly coupled to Au nanorods," *Nanoscale*, vol. 7, no. 18, pp. 8503–8509, 2015.

[95] S. Wang, T. Chervy, J. George, J. A. Hutchison, C. Genet, and T. W. Ebbesen, "Quantum yield of polariton emission from hybrid light-matter states," *J. Phys. Chem. Lett.*, vol. 5, no. 8, pp. 1433–1439, 2014.

[96] R. Bose, T. Cai, K. R. Choudhury, G. S. Solomon, and E. Waks, "All-optical coherent control of vacuum Rabi oscillations," *Nature Photon.*, vol. 8, no. 11, pp. 858–864, 2014.

[97] A. Canaguier-Durand, E. Devaux, J. George, Y. Pang, J. A. Hutchison, T. Schwartz, C. Genet, N. Wilhelms, J.-M. Lehn, and T. W. Ebbesen, "Thermodynamics of molecules strongly coupled to the vacuum field," *Angew. Chem.*, vol. 125, no. 40, pp. 10727–10730, 2013.

[98] T. Schwartz, J. A. Hutchison, C. Genet, and T. W. Ebbesen, "Reversible switching of ultrastrong light-molecule coupling," *Phys. Rev. Lett.*, vol. 106, no. 19, p. 196405, 2011.

[99] Y.-Y. Lai, Y.-P. Lan, and T.-C. Lu, "Strong light–matter interaction in ZnO microcavities," *Light: Sci. Appl.*, vol. 2, no. 6, p. e76, 2013.

[100] S. Chen, G. Li, D. Lei, and K. W. Cheah, "Efficient energy exchange between plasmon and cavity modes via Rabi-analogue splitting in a hybrid plasmonic nanocavity," *Nanoscale*, vol. 5, no. 19, pp. 9129–9133, 2013.

[101] W. Wang, P. Vasa, R. Pomraenke, R. Vogelgesang, A. De Sio, E. Sommer, M. Maiuri, C. Manzoni, G. Cerullo, and C. Lienau, "Interplay between strong coupling and radiative damping of excitons and surface plasmon polaritons in hybrid nanostructures," *ACS Nano*, vol. 8, no. 1, pp. 1056–1064, 2014.

[102] S. Gambino, M. Mazzeo, A. Genco, O. Di Stefano, S. Savasta, S. Patanè, D. Ballarini, F. Mangione, G. Lerario, and D. Sanvitto, "Exploring light–matter interaction phenomena under ultrastrong coupling regime," *ACS Photonics*, vol. 1, no. 10, pp. 1042–1048, 2014.

[103] S. Kéna-Cohen, S. A. Maier, and D. D. Bradley, "Ultrastrongly coupled exciton–polaritons in metal-clad organic semiconductor microcavities," *Adv. Opt. Mater.*, vol. 1, no. 11, pp. 827–833, 2013.

[104] J. A. Hutchison, T. Schwartz, C. Genet, E. Devaux, and T. W. Ebbesen, "Modifying chemical landscapes by coupling to vacuum fields," *Angew. Chem. Int.*, vol. 51, no. 7, pp. 1592–1596, 2012.

[105] J. A. Hutchison, A. Liscio, T. Schwartz, A. Canaguier-Durand, C. Genet, V. Palermo, P. Samorì, and T. W. Ebbesen, "Tuning the work-function via strong coupling," *Adv. Mater.*, vol. 25, no. 17, pp. 2481–2485, 2013.

[106] J. D. Plumhof, T. Stöferle, L. Mai, U. Scherf, and R. F. Mahrt, "Room-temperature Bose-Einstein condensation of cavity exciton-polaritons in a polymer," *Nat. Mater.*, vol. 13, no. 3, 2014.

[107] P. Vasa, W. Wang, R. Pomraenke, M. Lammers, M. Maiuri, C. Manzoni, G. Cerullo, and C. Lienau, "Real-time observation of ultrafast Rabi oscillations between excitons and plasmons in metal nanostructures with J-aggregates," *Nature Photon.*, vol. 7, no. 2, pp. 128–132, 2013.

[108] K. Daskalakis, S. Maier, R. Murray, and S. Kéna-Cohen, "Nonlinear interactions in an organic polariton condensate," *Nat. Mater.*, vol. 13, no. 3, pp. 271–278, 2014.

[109] K. F. MacDonald, Z. L. Sámson, M. I. Stockman, and N. I. Zheludev, "Ultrafast active plasmonics," *Nature Photon.*, vol. 3, no. 1, pp. 55–58, 2009.

[110] P. Törmä and W. L. Barnes, "Strong coupling between surface plasmon polaritons and emitters: a review," *Rep. Prog. Phys.*, vol. 78, no. 1, p. 013901, 2015.

[111] S. Balci, C. Kocabas, B. Küçüköz, A. Karatay, E. Akhüseyin, H. G. Yaglioglu, and A. Elmali, "Probing ultrafast energy transfer between excitons and plasmons in the ultrastrong coupling regime," *Appl. Phys. Lett.*, vol. 105, no. 5, p. 051105, 2014.

[112] T. Virgili, D. Coles, A. Adawi, C. Clark, P. Michetti, S. Rajendran, D. Brida, D. Polli, G. Cerullo, and D. Lidzey, "Ultrafast polariton relaxation dynamics in an organic semiconductor microcavity," *Phys. Rev. B.*, vol. 83, no. 24, p. 245309, 2011.

[113] N. T. Fofang, N. K. Grady, Z. Fan, A. O. Govorov, and N. J. Halas, "Plexciton dynamics: exciton- plasmon coupling in a J-aggregate-Au nanoshell complex provides a mechanism for nonlinearity," *Nano Lett.*, vol. 11, no. 4, pp. 1556–1560, 2011.

[114] P. Vasa, R. Pomraenke, G. Cirmi, E. De Re, W. Wang, S. Schwieger, D. Leipold, E. Runge, G. Cerullo, and C. Lienau, "Ultrafast manipulation of strong coupling in metal-molecular aggregate hybrid nanostructures," *ACS Nano*, vol. 4, no. 12, pp. 7559–7565, 2010.

[115] A. Salomon, C. Genet, and T. W. Ebbesen, "Molecule–light complex: Dynamics of hybrid molecule–surface plasmon states," *Angew. Chem.*, vol. 121, no. 46, pp. 8904–8907, 2009.

[116] T. Schwartz, J. A. Hutchison, J. Léonard, C. Genet, S. Haacke, and T. W. Ebbesen, "Polariton dynamics under strong light–molecule coupling," *ChemPhysChem*, vol. 14, no. 1, pp. 125–131, 2013.

[117] D. M. Coles, P. Michetti, C. Clark, W. C. Tsoi, A. M. Adawi, J.-S. Kim, and D. G. Lidzey, "Vibrationally assisted polariton-relaxation processes in strongly coupled organic-semiconductor microcavities," *Adv. Func. Mater.*, vol. 21, no. 19, pp. 3691–3696, 2011.

[118] D. M. Coles, R. T. Grant, D. G. Lidzey, C. Clark, and P. G. Lagoudakis, "Imaging the polariton relaxation bottleneck in strongly coupled organic semiconductor microcavities," *Phys. Rev. B.*, vol. 88, no. 12, p. 121303, 2013.

[119] L. Mazza, S. Kéna-Cohen, P. Michetti, and G. C. La Rocca, "Microscopic theory of polariton lasing via vibronically assisted scattering," *Phys. Rev. B.*, vol. 88, no. 7, p. 075321, 2013.

[120] H. Wang, A. Toma, H.-Y. Wang, A. Bozzola, E. Miele, A. Haddadpour, G. Veronis, F. De Angelis, L. Wang, Q.-D. Chen, *et al.*, "The role of Rabi splitting tuning in the dynamics of strongly coupled J-aggregates and surface plasmon polaritons in nanohole arrays," *Nanoscale*, vol. 8, no. 27, pp. 13445–13453, 2016.

[121] R. P. Zaccaria, "Butterfly wing color: A photonic crystal demonstration," *Opt. Lasers Eng.*, vol. 76, pp. 70–73, 2016.

[122] A. Alabastri, S. Tuccio, A. Giugni, A. Toma, C. Liberale, G. Das, F. D. Angelis, E. D. Fabrizio, and R. P. Zaccaria, "Molding of plasmonic resonances in metallic nanostructures: Dependence of the non-linear electric permittivity on system size and temperature," *Materials*, vol. 6, no. 11, pp. 4879–4910, 2013.

[123] G. A. Wurtz, P. R. Evans, W. Hendren, R. Atkinson, W. Dickson, R. J. Pollard, A. V. Zayats, W. Harrison, and C. Bower, "Molecular plasmonics with tunable exciton-plasmon coupling strength in J-aggregate hybridized Au nanorod assemblies," *Nano Lett.*, vol. 7, no. 5, pp. 1297–1303, 2007.

[124] Y. Nishijima, Y. Adachi, L. Rosa, and S. Juodkazis, "Augmented sensitivity of an IR-absorption gas sensor employing a metal hole array," *Opt. Mater. Express*, vol. 3, no. 7, pp. 968–976, 2013.

[125] Y. Nishijima, H. Nigorinuma, L. Rosa, and S. Juodkazis, "Selective enhancement of infrared absorption with metal hole arrays," *Opt. Mater. Express*, vol. 2, no. 10, pp. 1367–1377, 2012.

[126] H. Wang, H.-Y. Wang, B.-R. Gao, Y. Jiang, Z.-Y. Yang, Y.-W. Hao, Q.-D. Chen, X.-B. Du, and H.-B. Sun, "Surface plasmon enhanced absorption dynamics of regioregular poly (3-hexylthiophene)," *Appl. Phys. Lett.*, vol. 98, no. 25, p. 251501, 2011.

[127] H. Wang, H.-Y. Wang, B.-R. Gao, L. Wang, Z.-Y. Yang, X.-B. Du, Q.-D. Chen, J.-F. Song, and H.-B. Sun, "Exciton diffusion and charge transfer dynamics in nano phase-separated P3HT/PCBM blend films," *Nanoscale*, vol. 3, no. 5, pp. 2280–2285, 2011.

[128] L. Wang, C.-F. Wu, H.-Y. Wang, Y.-F. Wang, Q.-D. Chen, W. Han, W.-P. Qin, J. McNeill, and H.-B. Sun, "Internal structure-mediated ultrafast energy transfer in self-assembled polymer-blend dots," *Nanoscale*, vol. 5, no. 16, pp. 7265–7270, 2013.

[129] G. V. Hartland, "Optical studies of dynamics in noble metal nanostructures," *Chem. Rev.*, vol. 111, no. 6, pp. 3858–3887, 2011.

[130] J. Urayama, T. B. Norris, J. Singh, and P. Bhattacharya, "Observation of phonon bottleneck in quantum dot electronic relaxation," *Phys. Rev. Lett.*, vol. 86, no. 21, pp. 4930–4933, 2001.

[131] A. Tartakovskii, M. Emam-Ismail, R. Stevenson, M. Skolnick, V. Astratov, D. Whittaker, J. J. Baumberg, and J. Roberts, "Relaxation bottleneck and its suppression in semiconductor microcavities," *Phys. Rev. B.*, vol. 62, no. 4, pp. R2283–R2286, 2000.

[132] B. Huang, M. Bates, and X. Zhuang, "Super resolution fluorescence microscopy," *Annu. Rev. Biochem.*, vol. 78, p. 993, 2009.

[133] M. Elmeranta, G. Vicidomini, M. Duocastella, A. Diaspro, and G. de Miguel, "Characterization of nanostructures fabricated with two-beam DLW lithography using STED microscopy," *Opt. Mater. Express*, vol. 6, no. 10, pp. 3169–3179, 2016.

[134] E. Betzig and R. J. Chichester, "Single molecules observed by near-field scanning optical microscopy," *Science*, vol. 262, pp. 1422–1422, 1993.

[135] N. Fang, H. Lee, C. Sun, and X. Zhang, "Sub–diffraction-limited optical imaging with a silver superlens," *Science*, vol. 308, no. 5721, pp. 534–537, 2005.

[136] C. F. Martí Duocastella, P. Serra, and A. Diaspro, "Sub-wavelength laser nanopatterning using droplet lenses," *Scientific Reports*, vol. 5, p. 16199, 2015.

[137] L. P. Ghislain and V. B. Elings, "Scanning probe optical microscope using a solid immersion lens," Aug. 17 1999. US Patent 5,939,709.

[138] Z. Wang, W. Guo, L. Li, B. Luk'yanchuk, A. Khan, Z. Liu, Z. Chen, and M. Hong, "Optical virtual imaging at 50 nm lateral resolution with a white-light nanoscope," *Nat. Commun.*, vol. 2, p. 218, 2011.

[139] A. Darafsheh, C. Guardiola, A. Palovcak, J. C. Finlay, and A. Cárabe, "Optical super-resolution imaging by high-index microspheres embedded in elastomers," *Opt. Lett.*, vol. 40, no. 1, pp. 5–8, 2015.

[140] H. Yang, N. Moullan, J. Auwerx, and M. A. Gijs, "Super-resolution biological microscopy using virtual imaging by a microsphere nanoscope," *Small*, vol. 10, no. 9, pp. 1712–1718, 2014.

[141] Y. Yan, L. Li, C. Feng, W. Guo, S. Lee, and M. Hong, "Microsphere-coupled scanning laser confocal nanoscope for sub-diffraction-limited imaging at 25 nm lateral resolution in the visible spectrum," *ACS Nano*, vol. 8, no. 2, pp. 1809–1816, 2014.

[142] K. W. Allen, N. Farahi, Y. Li, N. I. Limberopoulos, D. E. Walker, A. M. Urbas, V. Liberman, and V. N. Astratov, "Super-resolution microscopy by movable thin-films with embedded microspheres: Resolution analysis," *Ann. Phys.*, vol. 527, no. 7-8, pp. 513–522, 2015.

[143] L. A. Krivitsky, J. J. Wang, Z. Wang, and B. Lukiyanchuk, "Locomotion of microspheres for super-resolution imaging," *arXiv preprint arXiv:1307.5595*, 2013.

[144] R. Horstmeyer, R. Heintzmann, G. Popescu, L. Waller, and C. Yang, "Standardizing the resolution claims for coherent microscopy," *Nature Photon.*, vol. 10, no. 2, pp. 68–71, 2016.

[145] A. Darafsheh, N. I. Limberopoulos, J. S. Derov, D. E. Walker Jr, and V. N. Astratov, "Advantages of microsphere-assisted super-resolution imaging technique over solid immersion lens and confocal microscopies," *Appl. Phys. Lett.*, vol. 104, no. 6, p. 061117, 2014.

[146] A. Darafsheh, "Comment on 'super-resolution microscopy by movable thin-films with embedded microspheres: Resolution analysis' [ann. phys. (berlin) 527, 513 (2015)]," *Ann. Phys.*, 2016.

[147] F. De Angelis, G. Das, P. Candeloro, M. Patrini, M. Galli, A. Bek, M. Lazzarino, I. Maksymov, C. Liberale, L. C. Andreani, and E. D. Fabrizio, "Nanoscale chemical mapping using three-dimensional adiabatic compression of surface plasmon polaritons," *Nat. Nanotechnology*, vol. 5, no. 1, pp. 67–72, 2010.

[148] F. De Angelis, F. Gentile, F. Mecarini, G. Das, M. Moretti, P. Candeloro, M. Coluccio, G. Cojoc, A. Accardo, C. Liberale, *et al.*, "Breaking the diffusion limit with super-hydrophobic delivery of molecules to plasmonic nanofocusing sers structures," *Nature Photon.*, vol. 5, no. 11, pp. 682–687, 2011.

[149] R. Ye, Y.-H. Ye, H. F. Ma, J. Ma, B. Wang, J. Yao, S. Liu, L. Cao, H. Xu, and J.-Y. Zhang, "Experimental far-field imaging properties of a $\sim$ 5-μm diameter spherical lens," *Opt. Lett.*, vol. 38, no. 11, pp. 1829–1831, 2013.

[150] X. Hao, C. Kuang, X. Liu, H. Zhang, and Y. Li, "Microsphere based microscope with optical super-resolution capability," *Appl. Phys. Lett.*, vol. 99, no. 20, p. 203102, 2011.

[151] Y. Duan, G. Barbastathis, and B. Zhang, "Classical imaging theory of a microlens with super-resolution," *Opt. Lett.*, vol. 38, no. 16, pp. 2988–2990, 2013.

[152] L. Li, W. Guo, Y. Yan, S. Lee, and T. Wang, "Label-free super-resolution imaging of adenoviruses by submerged microsphere optical nanoscopy," *Light: Sci. Appl.*, vol. 2, no. 9, p. e104, 2013.

[153] J. N. Monks, B. Yan, N. Hawkins, F. Vollrath, and Z. Wang, "Spider silk: Mother nature's bio-superlens," *Nano Lett.*, vol. 16, no. 9, pp. 5842–5845, 2016.

[154] C. B. Müller and J. Enderlein, "Image scanning microscopy," *Phys. Rev. Lett.*, vol. 104, no. 19, p. 198101, 2010.

[155] V. M. Sundaram and S.-B. Wen, "Analysis of deep sub-micron resolution in microsphere based imaging," *Appl. Phys. Lett.*, vol. 105, no. 20, p. 204102, 2014.

[156] A. V. Maslov and V. N. Astratov, "Imaging of sub-wavelength structures radiating coherently near microspheres," *Appl. Phys. Lett.*, vol. 108, no. 5, p. 051104, 2016.

Appendix A
Proof of Eq. 3.2

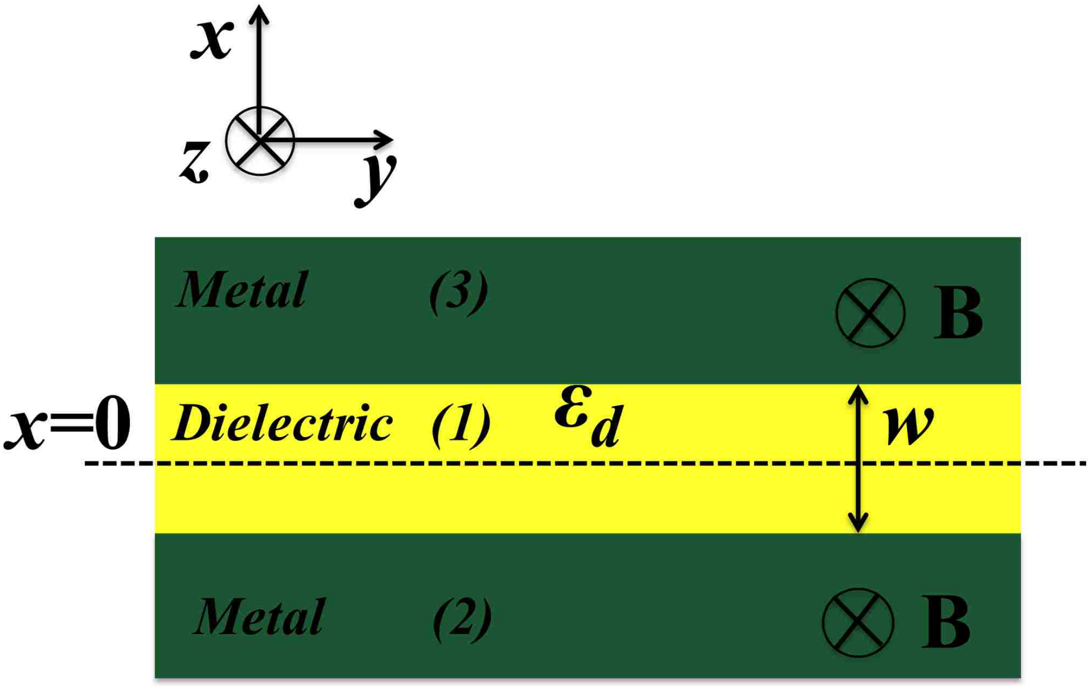

Figure A.1: Schematic of a MDM waveguide. The metal is subject to an externally applied static magnetic field.

As we mention in Chapter 3, the dispersion relation for the optical modes supported by the MDM waveguide, in which the metal is subject to an externally applied static magnetic field, can be derived by applying the boundary conditions at the metal-dielectric interfaces. The boundary conditions are that the tangential components of the electric and magnetic field (E_y and H_z) have to be continuous at the two metal-dielectric interfaces at Fig. A.1.

The first step is to express the tangential components of the fields in the different regions of the waveguide. Using Maxwell's equations and the dielectric permittivity of the metal (Eq. 3.1), we obtain the following expressions for the fields in the dielectric ($-w/2 < x < w/2$), and the metal ($x < -w/2$ and $x > w/2$):

$$\begin{cases} H_{1z} = (Ce^{k_d x} + De^{-k_d x})e^{iky}, & \text{(A.1a)} \\ E_{1y} = -i\dfrac{k_d}{\varepsilon_0 \varepsilon_1 \omega}(Ce^{k_d x} - De^{-k_d x})e^{iky}, \qquad -w/2 < x < w/2 & \text{(A.1b)} \end{cases}$$

$$\begin{cases} H_{2y} = Be^{k_m x + iky}, & \text{(A.2a)} \\ E_{2y} = \dfrac{X_-}{\varepsilon_0 \omega} H_{2z}, \qquad x < -w/2 & \text{(A.2b)} \end{cases}$$

$$\begin{cases} H_{3z} = Ae^{-k_m x + iky}, & \text{(A.3a)} \\ E_{3y} = \dfrac{X_+}{\varepsilon_0 \omega} H_{3z}, \qquad x > w/2 & \text{(A.3b)} \end{cases}$$

where A, B, C, D are constants, $X_\pm = \frac{\pm i k_m - k\varepsilon_{xy}/\varepsilon_{xx}}{\varepsilon_m}$, and $\varepsilon_m = \varepsilon_{xx} + \varepsilon_{xy}^2/\varepsilon_{xx}$, k is the y component of the wave vector, and $k_i = \sqrt{k^2 - k_0^2 \varepsilon_i}\quad, i = d, m$. Imposing the boundary conditions at $x = w/2$ (please see Fig. A.1 above), we obtain

$$\begin{cases} H_{3z}(y, x = w/2) = H_{1z}(y, x = w/2) \Rightarrow Ae^{-k_m w/2} = Ce^{k_d w/2} + De^{-k_d w/2}, & \text{(A.4a)} \\ E_{3y}(y, x = w/2) = E_{1y}(y, x = w/2) \Rightarrow X_+ Ae^{-k_m w/2} = \dfrac{ik_d}{\varepsilon_d}(-Ce^{k_d w/2} + De^{-k_d w/2}). & \text{(A.4b)} \end{cases}$$

Imposing the boundary conditions at $x = -w/2$ (please see Fig. A.1 above), we obtain

$$\begin{cases} H_{2z}(y, x = -w/2) = H_{1z}(y, x = -w/2) \Rightarrow Be^{-k_m w/2} = Ce^{-k_d w/2} + De^{k_d w/2}, & \text{(A.5a)} \\ E_{2y}(y, x = -w/2) = E_{1y}(y, x = -w/2) \Rightarrow X_- Be^{-k_m w/2} = & \\ \qquad\qquad\qquad\qquad \dfrac{ik_d}{\varepsilon_d}(-Ce^{-k_d w/2} + De^{k_d w/2}). & \text{(A.5b)} \end{cases}$$

Eqs. A.4a, A.4b, A.5a, and A.5b form a system of four equations with four unknowns (A, B, C, and D). We set the determinant equal to zero in order to have nontrivial solutions for A, B, C, and D, and derive the following dispersion relation for the optical modes supported by the structure

$$\exp(2k_d w) = \frac{\left(\frac{k\varepsilon_{xy}}{\varepsilon_{xx}\varepsilon_m}\right)^2 + (k_d/\varepsilon_d - k_m/\varepsilon_m)^2}{\left(\frac{k\varepsilon_{xy}}{\varepsilon_{xx}\varepsilon_m}\right)^2 + (k_d/\varepsilon_d + k_m/\varepsilon_m)^2}. \tag{A.6}$$

Appendix B
Proof of Eq. 3.3

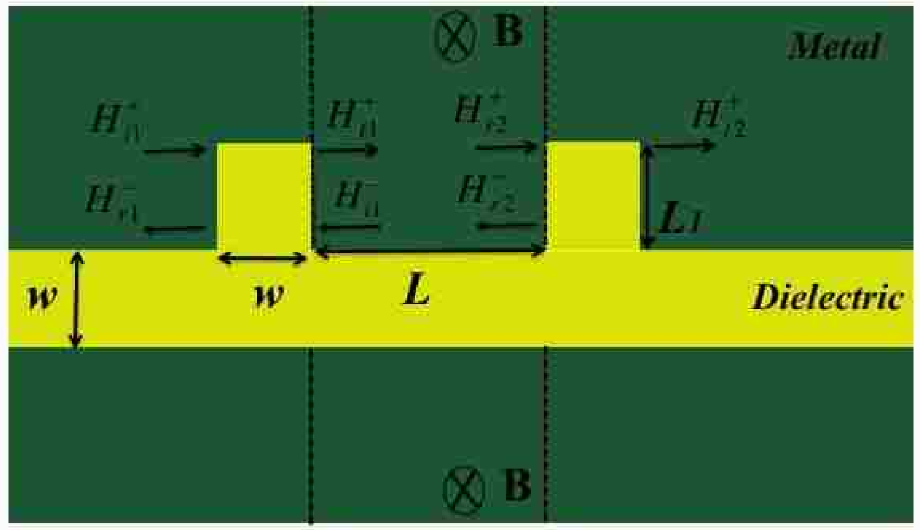

Figure B.1: Schematic of a Fabry-Perot cavity structure consisting of a MDM waveguide side-coupled to two MDM stub resonators. The metal region between the two stubs is subject to an externally applied static magnetic field.

We consider a Fabry-Perot cavity structure consisting of a MDM waveguide side-coupled to two MDM stub resonators shown in Fig. B.1. The metal region between the two stubs is subject to an externally applied static magnetic field. Such a system can be described by the following equations

$$\begin{cases} H_{t1}^+ = t_1 H_{i1}^+ + r_1 H_{i1}^-, & \text{(B.1a)} \\ H_{r2}^- = r_2 H_{i2}^+, & \text{(B.1b)} \\ H_{t2}^+ = t_2 H_{i2}^+, & \text{(B.1c)} \end{cases}$$

where t_1 and r_1 (t_2 and r_2) are transmission and reflection coefficients, respectively, when the metal region to the right (left) of the stub is subject to a static magnetic field (Fig. 3.12). We also have

$$\begin{cases} H_{i2}^{+} = H_{t1}^{+} e^{-kL}, & \text{(B.2a)} \\ H_{i1}^{-} = H_{r2}^{-} e^{-kL}. & \text{(B.2b)} \end{cases}$$

Using the above equations we obtain

$$H_{t2}^{+} = t_2 e^{-kL}(t_1 H_{i1}^{+} + r_1 e^{-kL} r_2 e^{-kL} H_{t1}^{+}), \tag{B.3}$$

$$H_{t1}^{+} = t_1 H_{i1}^{+} + r_1 e^{-kL} r_2 e^{-kL} H_{t1}^{+}, \tag{B.4}$$

$$H_{t1}^{+} = \frac{t_1 H_{i1}^{+}}{1 - r_2 r_1 e^{-2kL}}. \tag{B.5}$$

Substituting Eq. B.5 in Eq. B.3, we will have:

$$\frac{H_{t2}^{+}}{H_{i1}^{+}} = \frac{t_1 t_2 e^{-kL}}{1 - r_2 r_1 e^{-2kL}}, \tag{B.6}$$

so the transmission will be:

$$T = |\frac{t_1 t_2 e^{-kL}}{1 - r_1 r_2 e^{-2kL}}|^2. \tag{B.7}$$

Appendix C
Hemisphere and Protruded Hemisphere

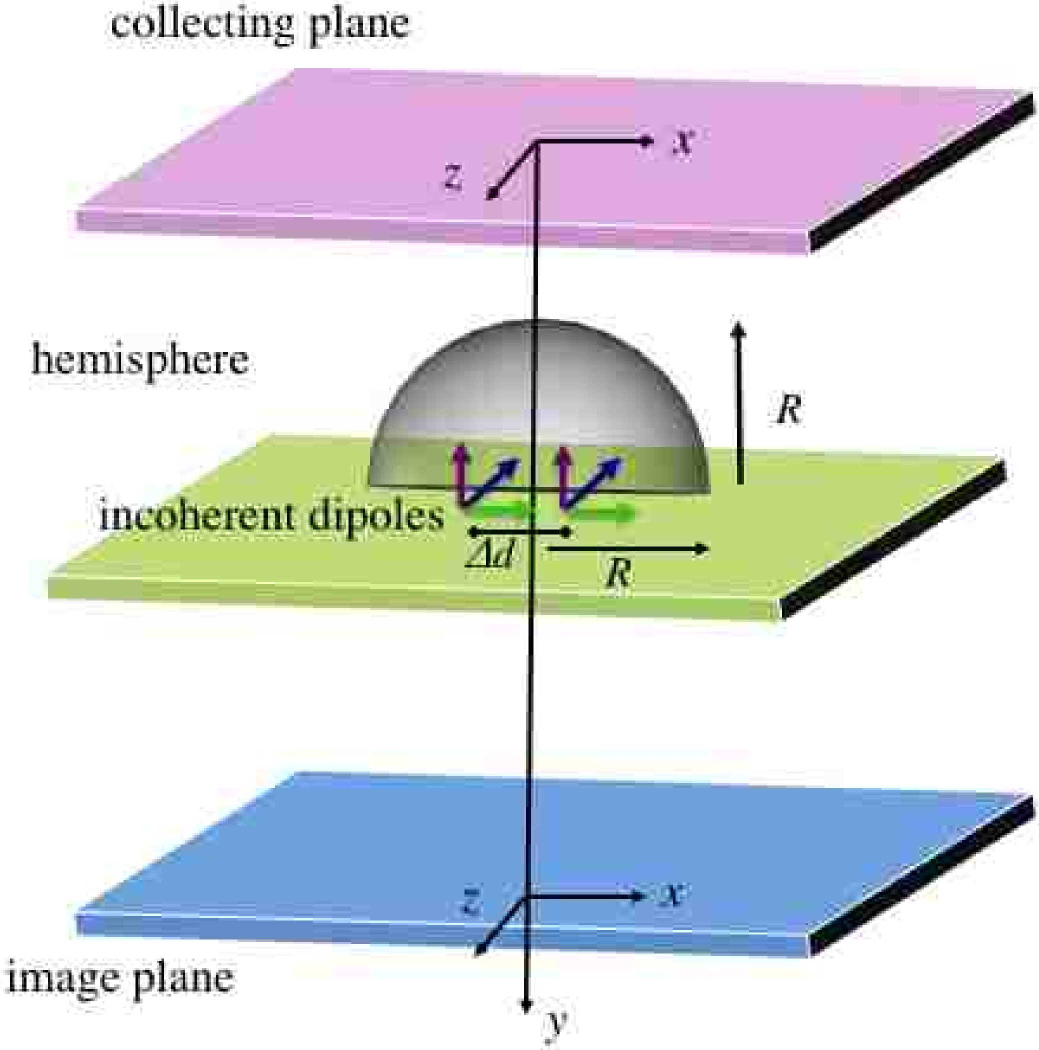

Figure C.1: Schematic of the simulated layout, with two incoherent dipoles separated by a distance Δd=250 nm placed in contact with the silica hemisphere with diameter of 4.7 μm and refractive index of 1.46.

Here we consider two additional cases. In Fig. C.1, we show a hemispherical lens instead of a microsphere. We replace the microsphere in our simulations by a hemisphere (Fig. C.1). In Fig. C.3, we show a more protruded object. The dipoles are separated by a distance of Δd=250 nm, in contact with the flat part of the lens. The wavelength of the illumination source is 405 nm corresponding to a blue LED . The corresponding field profiles are shown in Figs. C.2 and C.4.

We also show FDTD simulation results when the wavelength of the illumination source is 405 nm, 520 nm, and 633 nm. The dipoles are 300 nm apart. We use a silica microsphere with a diameter of 4.7 μm and refractive index of 1.46. We observe that when the wavelength of the illumination source is 405 nm the dipoles are more distinguishable compared to other cases. The corresponding field profiles are illustrated in Figs. C.5, C.6, and C.7.

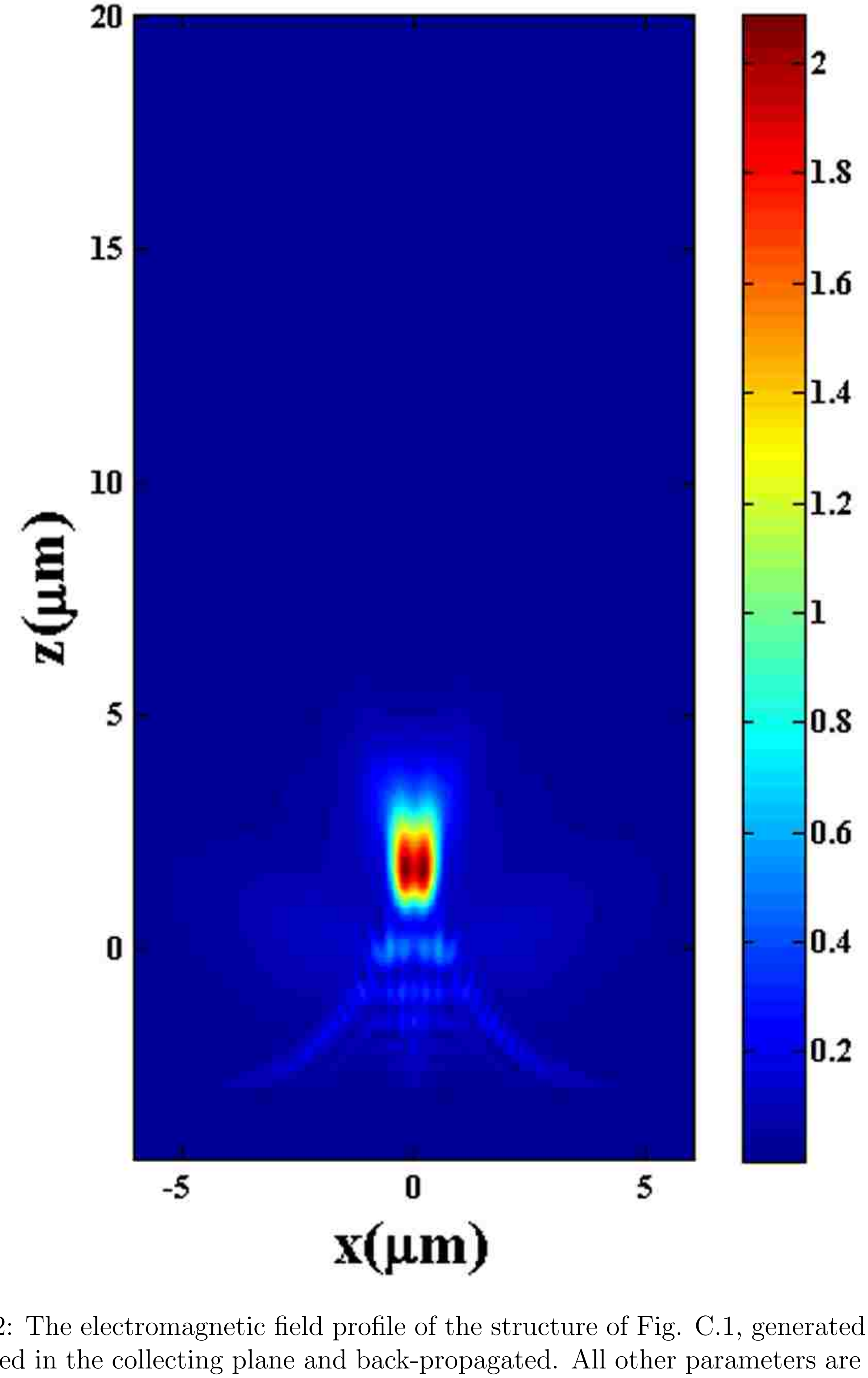

Figure C.2: The electromagnetic field profile of the structure of Fig. C.1, generated by the dipoles is calculated in the collecting plane and back-propagated. All other parameters are as in Fig. C.1.

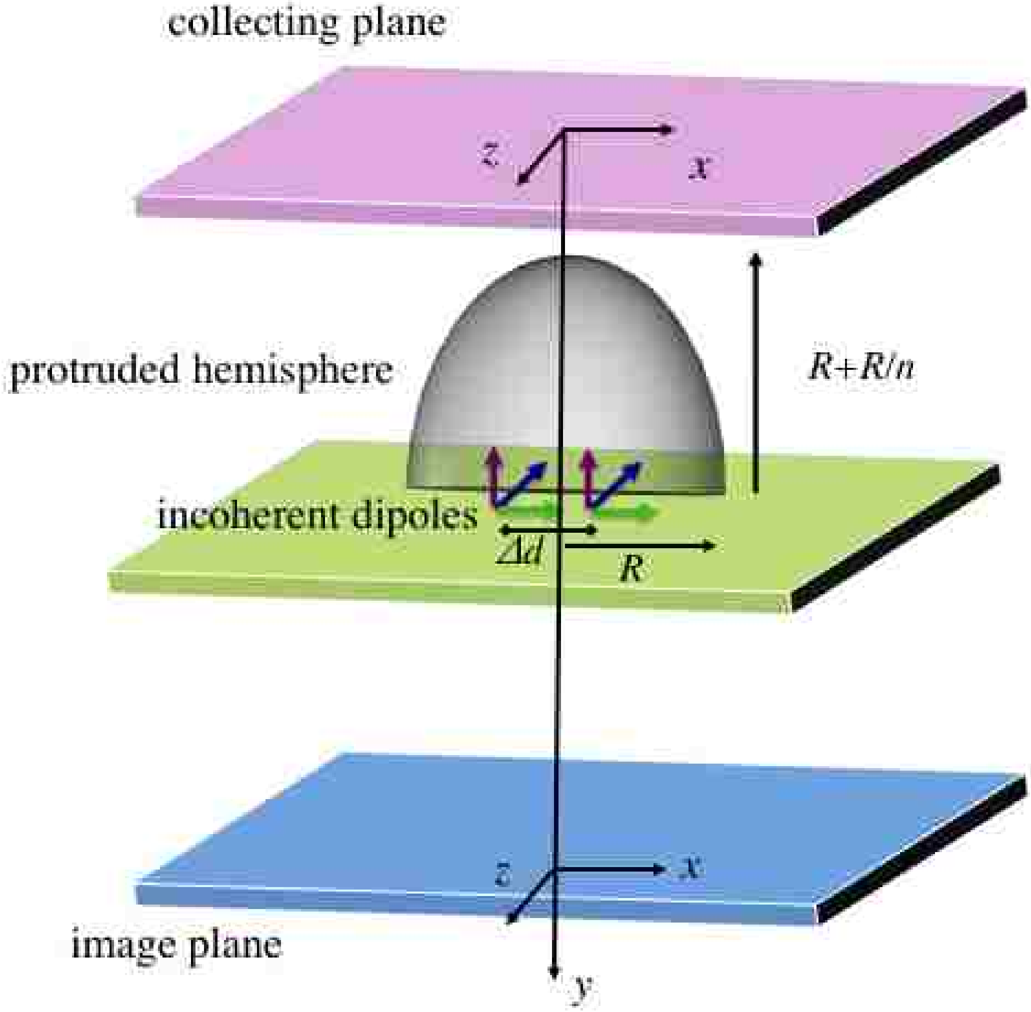

Figure C.3: Schematic of the simulated layout, with two incoherent dipoles separated by a distance of Δd=250 nm placed in contact with the silica protruded hemisphere with diameter of 4.7 μm and refractive index of n=1.46.

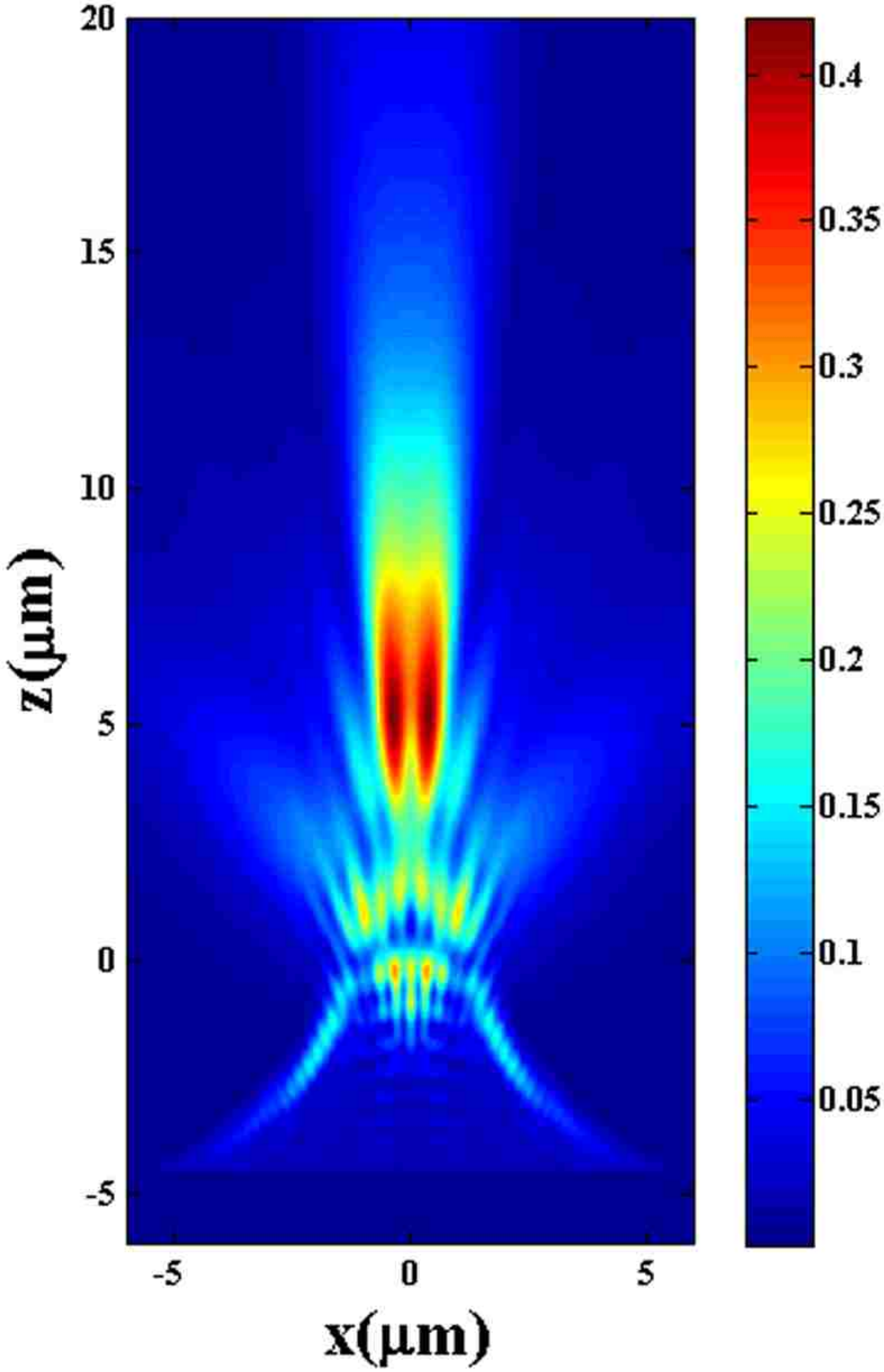

Figure C.4: The electromagnetic field profile of the structure of Fig. C.3, generated by the dipoles is calculated in the collecting plane and back-propagated. All other parameters are as in Fig. C.3.

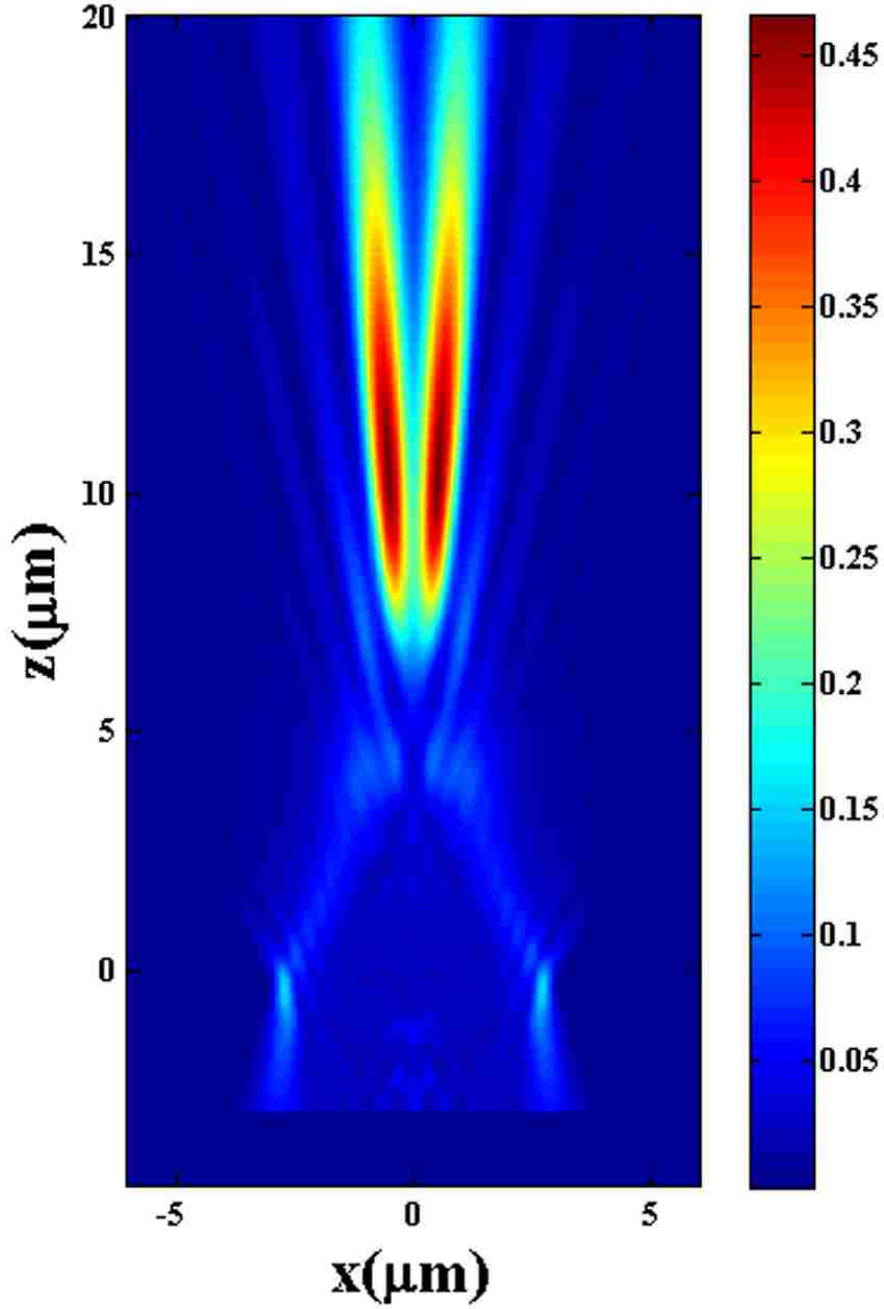

Figure C.5: The electromagnetic field profile of the structure of Fig. 5.8, generated by the dipoles is calculated in the collecting plane and back-propagated when the wavelength of the illumination source is 405 nm. All other parameters are as in Fig. 5.8.

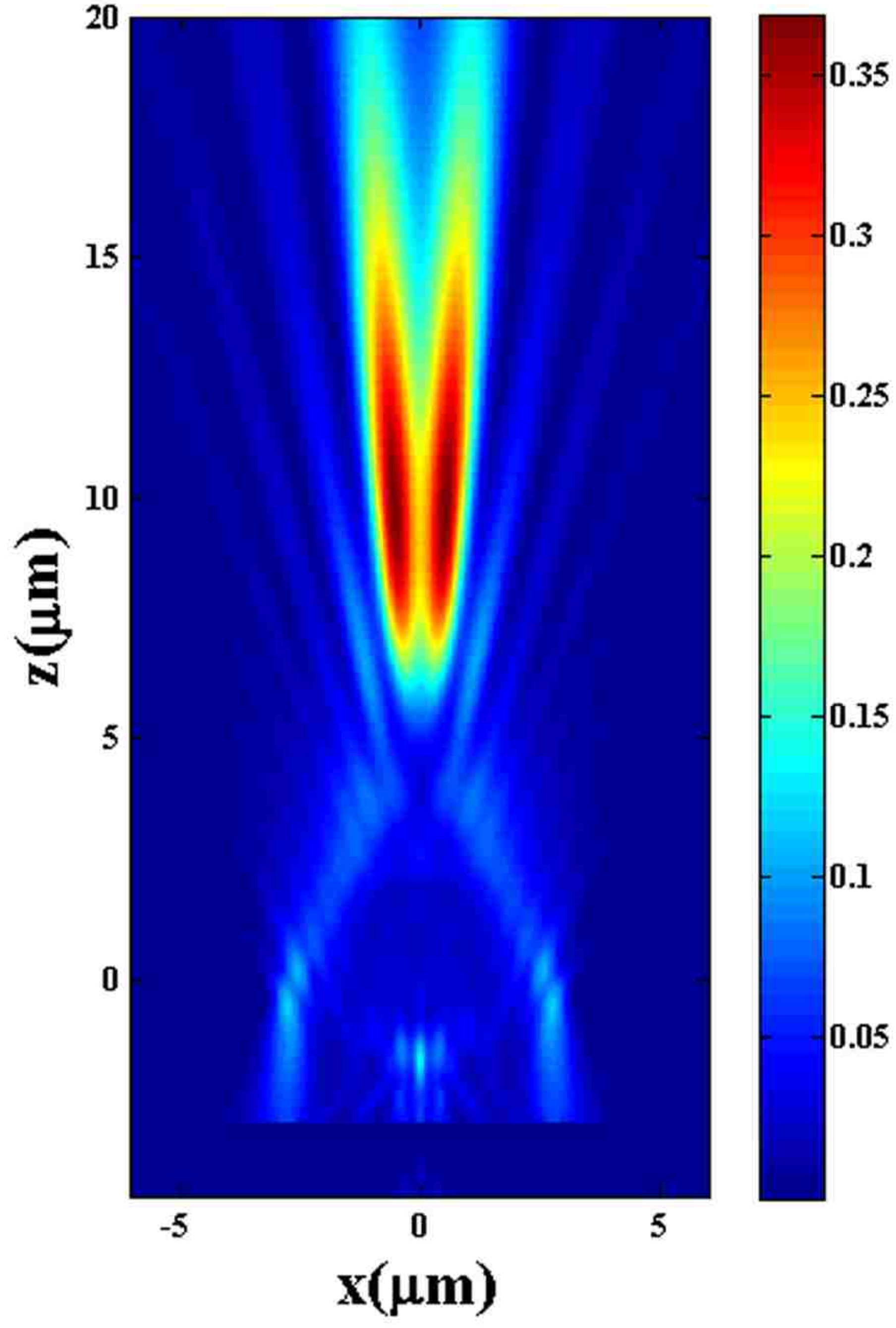

Figure C.6: The electromagnetic field profile of the structure of Fig. 5.8, generated by the dipoles is calculated in the collecting plane and back-propagated when the wavelength of the illumination source is 520 nm. All other parameters are as in Fig. 5.8.

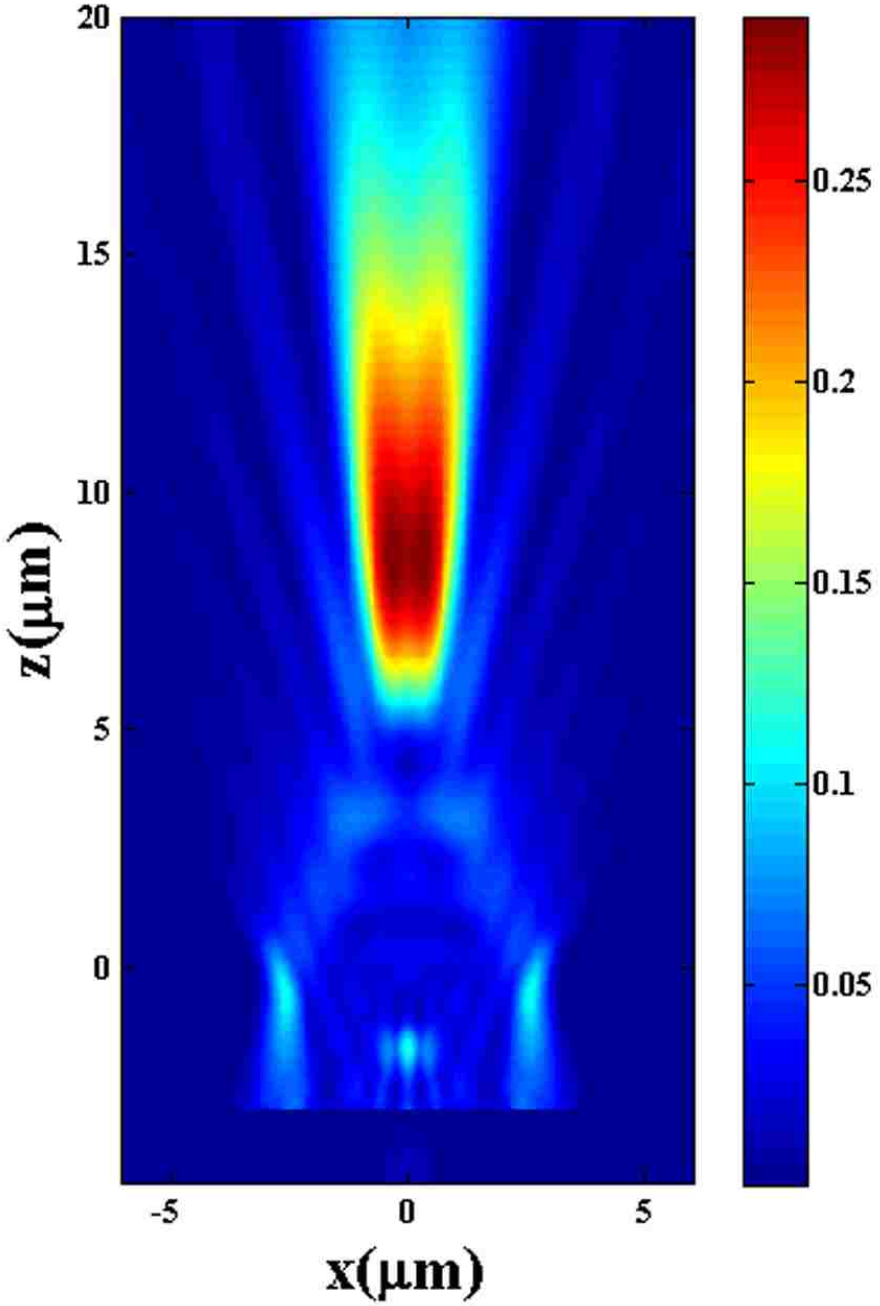

Figure C.7: The electromagnetic field profile of the structure of Fig. 5.8, generated by the dipoles is calculated in the collecting plane and back-propagated when the wavelength of the illumination source is 633 nm. All other parameters are as in Fig. 5.8.

Vita

Ali Haddadpour was born in 1987 in Marand, Iran. He graduated from Taleghani High School in 2005. He proceeded to get his B.Sc. and M.Sc. in electrical engineering from the University of Tabriz in Tabriz in 2009 and 2011, respectively. In August 2012 he came to Louisiana State University to pursue graduate studies. He is currently a candidate for the Doctor of Philosophy degree in Electrical Engineering which will be awarded in May 2017.